工學博士學位論文

**Fabrication of Flexible Graphene Thin Films via
Solution Process and Their Electronic Device Applications**

용액 공정법을 이용한 유연성 그래핀 박막의 제조 및
전자 소자 응용

2014年 8月

서울大學校 大學院

化學生物工學部

申 槿 泳

Fabrication of Flexible Graphene Thin Films via Solution Process and Their Electronic Device Applications

용액 공정법을 이용한 유연성 그래핀 박막의 제조 및
전자 소자 응용

指導敎授: 張 正 植

이 論文을 工學博士 學位論文으로 提出함

2014年 5月

서울大學校 大學院

化學生物工學部

申 槿 泳

申 槿 泳의 工學博士 學位論文을 認准함

2014年 5月

委 員 長 _____ (인)

副委員長 _____ (인)

委   員 _____ (인)

委   員 _____ (인)

委   員 _____ (인)

Fabrication of Flexible Graphene Thin Films via Solution Process and Their Electronic Device Applications

by

Keun-Young Shin

Submitted to the Graduate School of Seoul National University

in Partial Fulfillment of the Requirements

for the Degree of Doctor of Philosophy

August, 2014

Thesis Adviser: Jyongsik Jang

ABSTRACT

Graphene, typically composed of one-atom-thick layer of carbon in a 2D hexagonal lattice, is a basic building block for graphitic materials of all other dimensionalities. The graphene has attracted tremendous worldwide attention because of their fascinating properties different from those of the carbon-based graphitic materials (*e.g.*, extremely high charge carrier mobility, large specific surface area, thermal/electrical conductivity, and chemical/mechanical stability). Up to date, various synthetic methods for preparing graphene thin films have been developed. However, most previous synthetic methods suffer from high-cost, complicated processing technique and low flexibility of the film. Consequently, it is still challenging to produce graphene thin films with good electrical, mechanical and thermal property via low-cost solution process.

This dissertation describes the four different ways in the synthetic methodology of graphene materials and flexible graphene thin films using simple solution processes. First, chemically exfoliated graphene thin film was fabricated via inkjet printing and vapor deposition process, and it could be applied for the electrodes of dipole antenna and thin film speaker. Second, size-controlled graphene thin film with uniform conductivity and outstanding

flexibility could be prepared through a mechanochemical method and screen printing for use of transparent electrode. Third, multilayered graphene thin film with good thermal conductivity were able to be obtained from the graphite intercalation compound, microwave and screen printing, allowing its application for line-heater production. Lastly, graphene/polyaniline thin films with outstanding mechanical and electrical property could have been formed by in or ex-situ polymerization and screen printing for monopole and dipole tag antenna application. The graphene-based thin films on flexible substrate exhibited sustained mechanical, electrical and thermal property. Most importantly, these novel approaches can be used as an alternative tool for fabrication of various carbon-based thin films and functional devices, and may offer an opportunity for the further investigation of industrial applications, and might be expanded to allow the electronic device applications of graphene-based thin films in a wide range of areas.

List of Abbreviations

AFM : atomic force microscopy

ANC : active noise cancellation

APS : ammonium persulfate

C_0 : speed of light in free space

C_{60} : fullerene

CH_3NO_2 : nitromethane

CNT : carbon nanotubes

CSR : controlled shear rate

CVD : chemical vapor deposition

D : drain

D : density of water

d : particle diameter

DC : direct current

De- : de-doped

DLS : dynamic light scattering

DMF : dimethylformamide

EB : emeraldine base

EGnP : expanded-graphite nanoplatelets

ER : electrorheological

ES : emeraldine salt

f : frequency in free space

$FeCl_3$: iron chloride

FET : field effect transistor

FTIR : fourier transform infrared

G : graphene

G : gravitational acceleration

GICs : graphite intercalation compounds

GNRs : graphene nanoribbons

GO : graphene oxide

GOD : glucose oxidase

H_2SO_4 : sulfuric acid

H_2O_2 : hydrogen peroxide

HCl : Hydrochloric acid

ILC : ionic liquid crystals

ITO : indium tin oxide

$KMnO_4$: potassium permanganate

KPS : potassium persulfate

L_d : crystalline domain size

LPCVD : low pressure chemical vapor deposition

MWCNT : multi-walled carbon nanotube

$N_2H_4.H_2O$: hydrazine monohydrate

$NaNO_3$: sodium nitrate

OFET : Organic field-effect transistors

OLEDs : organic light-emitting diodes

P : pycnometer mass

PAHs : polycyclic aromatic hydrocarbons

PANI : polyaniline

PDMS : polydimethylsiloxane

PEDOT: poly (3,4-ethylenedioxythiophene)

PES : poly (ethersulfone)

PET : poly (ethyleneterephtalate)

PI : polyimide

PPy : polypyrrole

PSS : poly(styrenesulfonate)

PVDF : poly (vinylidene fluoride)

RFID : Radio Frequency Identification

R : measured sheet resistance

Re- : re-doped

rGO : reduced graphene oxide

RL : return loss

R_s : initial average sheet resistance

S : source

SEM : scanning electron microscope

Si : silicon

SiC : silicon carbide

SWCNT : single-walled carbon nanotube

TEM : transmission electron microscopy

t_{rec} : recovery times

t_{res} : response times

UHV : ultra-high vacuum

VDP : vapor deposition

V_g : sedimentation velocity

vol% : volume fraction

V_{rms} : root mean square voltage

VSWR : voltage standing wave ratio

wt% : weight content

W_0 : masses of particles

W_1 : masses of particles and liquid

W_2 : masses of liquid in the bottle

XPS : X-ray photoelectron spectroscopy

XRD : X-ray diffraction

α : fine structure constant

ε_r : relative permittivity of medium

ε' : permittivity

ε'' : loss factor

η : viscosity

λ : wavelength

λ_0 : wavelength in free space.

λ' : Raman excitation wavelength

μCP : microcontact printing

μ_r : permeability of medium

ρ_l : liquid density

ρ_p : particle density

σ : electrical conductivity

τ_E : shear stresses with an applied electric field strength

τ_o : shear stresses without an applied electric field strength

τ_y : yield stress

$\Delta R/R_s$: sheet resistance change

List of Figures

graphenes using graphite as the starting material. This is followed by: (1) An oxidative treatment is initially performed to generate oxidized graphite; (2) exfoliation by ultrasonication to generate GO; (3) reduction of GO via various reduction methods to produce rGO.

Figure 6. Schematic description of Si atom sublimation in Si-terminated 4H– SiC under a) thermal annealing process, b) pulsed electronic beam irradiation process. Reprinted with permission from Ref. 47. Copyright 2010 Royal Society of Chemistry.

Figure 7. a) Schematic diagram of the roll-based production of graphene films grown on a copper foil. The processes are divided into three steps: (1) the adhesion of polymer supports, (2) copper etching and (3) transfer to the target substrate. b) Photographs of the roll-based production of graphene films on copper foil produced by the process shown in panel (a). Reproduced with permission from Ref. 54. Copyright 2010 Right Managed by Nature Publishing Group.

Figure 8. There are several methods of mass-production of graphene, which allow a wide choice in terms of size, quality and price for any

particular application. Reproduced with permission from Ref. 72. Copyright 2012 Right Managed by Nature Publishing Group.

Figure 9. a) Fabrication of graphene film by Meyer rod coating and b) Photograph of a large-scale graphene film. c) The resistance change with tensile strain applied to RGO and ITO films on PET substrates under bending and unbending conditions. d) A flexible four-wire resistance touch screen fabricated using graphene electrodes. e) Linearity test of NC-FTS-1. The intersections of the lines indicate the practical touch points, and the black dots indicate the detected points. Reproduced with permission from Ref. 87. Copyright 2010 Wiley-VCH Verlag GmbH & Co. KGaA.

Figure 10. a) Schematic diagram of the steps used to fabricate the ion gel gated graphene transistor array on a plastic substrate. b) Optical images of an array of devices on a plastic substrate. c) Transfer and output characteristics of graphene FETs on plastic substrate. In output curve, the gate voltage was varied between +2 and –3 V in steps of –1 V. Reprinted with permission from Ref. 82. Copyright 2011

American Chemical Society.

with permission from Ref. 98. Copyright 2011 Right Managed by

Nature Publishing Group.

Figure 13. a) The fabrication of patterned GO on PET film by inkjet printing. b)

Large-area patterned GO (left image) and graphene sheets resulted

from the reduction procedure (right image). c) The reduction

process was performed by mild-thermal annealing at 90 $^{\circ}$C with

hydrazine and ammonia vapor.

Figure 14. a) Representative AFM and b) TEM image of the exfoliated GO as

a conducting ink for inkjet printing. For the sample preparation, the

exfoliated GO solution was deposited on Si wafer and copper grid,

respectively.

Figure 15. a) Deconvoluted XPS spectrum of patterned GO films by repeat

inkjet printing for 30 passes (top image) and graphene sheets

resulted from the reduction procedure (bottom image) in the C1s

region. Fit lines are labeled as: C−C, C−O and C=O bonds. b)

Raman spectra of patterned graphene sheets on the PET film

showing G and 2D peaks. A weak D peak is apparent, consistent

with edge effects.

printing number using inkjet printing and reduction process (Inset: AFM image of graphene film acquired by inkjet printing for 1 pass which has observable range of 50 μm) b) The surface sheet resistances of graphene-based PVDF films with different film thickness (Inset: the data represented by transmittance versus sheet resistance with the same film thickness).

Figure 28. a) The frequency response of the graphene-based thin film transducer with three different electrode thickness (60, 90 and 120 nm) compared to the PEDOT:PSS-based commercial thin film transducer b) Each frequency response at the flat and bending conditions (radius: 6 cm) of graphene-based thin film transducer with 120 nm electrode thickness.

Figure 29. The ANC effect on the harmonics of graphene-based thin film transducer from 3 kHz tonal signal. A soft substrate (3M VHB 4910 acrylic form tape) was cleaved to the film to make an ANC actuator. [stars indicate harmonic sounds at multiples of 3 kHz.]

Figure 30. Schematic illustration of the production of size-controlled graphite

silicone oil-based ER fluid was *ca.* 2.4 at 105 Hz.

vol% in silicone oil) (inset: definition of the sedimentation ratio).

EGnP.

Figure 59. a) Fabrication of patterned EGnP on a PI film using screen printing and side-view schematic of the EGnP-based line heater with a Cu electrode pair. b) The top-view of the fabrication schematic. The molar concentration of KPS for synthesis of EGnP was 150 mM, and the weight ratio of EGnP ink dispersed in an aqueous solution was 30 wt%. For the reduction of heat loss at high temperatures (> 140 °C), the EGnP films were located within "closed" PI substrates and copper tape was used to lower the contact resistance to the DC power supply. The synthesized EGnP-based lines had a width of 2.5 mm and a length of 100 mm.

Figure 60. Surface sheet resistances of EGnP-based line with different thicknesses produced by screen printing. The concentration of EGnP in the water solution for screen printing ink was 30 wt%. Different film thicknesses were obtained by controlling the number of prints.

Figure 61. Temperature history of the EGnP-based line heater while applying an input voltage of 12 V. The temperature distribution on the PI

substrate was measured continuously by an infrared thermal imager.

Figure 62. a) Temperature profiles of EGnP-based line heaters for different applied DC voltages. b) Temperature as a function of power consumption for EGnP-based line heaters. The inset table indicates the relationship between the applied voltage and current to the EGnP-based line heater. Using a digital multimeter, the average resistance over the 10 cm line length was *ca.* 28.5 Ω.

Figure 63. The infrared thermal images of EGnP-based heater while applying an input voltage of 3 V in 60 s. The size of rectangular heater was 4 × 4 cm.

Figure 64. a) Infrared image of an EGnP-based heater under flat and bending conditions (radius of curvature: 4 cm). b) The temperature value and resistance of EGnP-based line heaters for a line distance of 10 cm with respect to the bending radius. For the bending test, EGnP-based 4-lines were used with heater and temperature values measured 60 s after applying the 12 V input voltage.

Figure 65. Water heating results a) before and b) after operation of the EGnP-

based line heater under an applied voltage of 14 V. The volume of the water used for the boiling test was 500 mL and the time required to raise the water temperature (*ca.* 90.2 °C) was 30 min.

Figure 66. a) SEM, b) TEM and c) AFM images of pristine multilayer graphene, respectively. (inset: Raman spectra of multilayer graphene indicating the D, G and 2D peaks).

Figure 67. Representative SEM micrographs of a synthesized a) G/PANI/PSS and b) graphene/PANI hybrid films. For SEM sample preparation, 30 wt% graphene powder was mechanically blended with the PANI/PSS or PANI aqueous solution.

Figure 68. FTIR spectra of PANI/PSS and G/PANI/PSS. Powdered samples were used for FTIR analysis.

Figure 69. a) Surface resistance of the G/PANI/PSS hybrid film as a function of the graphene concentration. The inset scheme indicates the "bridge effect" of the PANI/PSS in the graphene interlayer. b) Shear viscosity of the G/PANI/PSS-based conducting ink according to the graphene content. The shear rate to measure viscosity was 0.1 s^{-1}.

at the marked areas (scale bar: 100 μm). c) A schematic mechanism illustrates the observed differences in edge waviness between the pristine graphene and the G/PANI/PSS hybrid film.

straight lines with the width of *ca.* 500 μm and length of *ca.* 3 cm on photo paper. The patterning of three different conductive materials-based thin films was obtained via screen printing.

List of Tables

Table of Contents

1. INTRODUCTION

1.1. Background

1.1.1. Graphene

Graphene, a one-atom-thick planar sheet of sp^2-bonded carbon atoms densely packed in a honeycomb crystal lattice, has grabbed appreciable attention to be used as a next generation electronic material, due to its exceptional properties including high current density, ballistic transport, chemical inertness, high thermal conductivity, optical transmittance and super hydrophobicity at nanometer scale (Figure 1) [1,2]. While studies of graphite have included those utilizing fewer and fewer layers for some time, the field was delivered a jolt in 2004, when Geim and co-workers at Manchester University first isolated single-layer samples from graphite [3,4]. The mechanical exfoliation technique isolated the two-dimensional crystals from three-dimensional graphite. Resulting single- and few-layer flakes were pinned to the substrate by only van der Waals forces and could be made free-standing by etching away the substrate [5,6]. In the end, they won the 2010 Nobel Prize in Physics for their groundbreaking work on graphene. Its extended honeycomb network is the basic building block of other important allotropes; it can be stacked to form 3D graphite, rolled to form 1D nanotubes, and wrapped to form 0D fullerenes. Long-range π-conjugation in graphene yields extraordinary
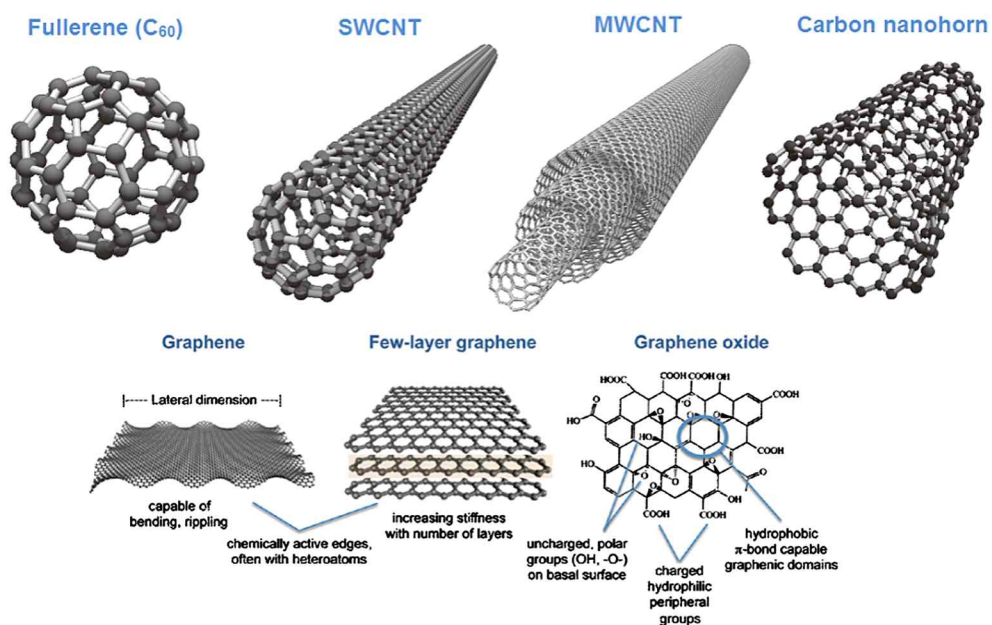
Figure 1. Structures of various important carbon nanomaterials: fullerene (C_{60}), single-walled carbon nanotube (SWCNT), multi-walled carbon nanotube (MWCNT), carbon nanohorn, graphene, few layer graphene and graphene oxide. Reprinted with permission. Copyright 2012 Elsevier.

thermal, mechanical, and electrical properties, which have long been the interest of many theoretical studies and more recently became an exciting area for experimentalists. Many graphene characteristics measured in experiments have exceeded those obtained in any other material, with some reaching theoretically predicted limits: room-temperature electron mobility of 2.5×10^5 $cm^2 V^{-1} s^{-1}$ [7]; a Young's modulus of 1 TPa and intrinsic strength of 130 GPa [8]; very high thermal conductivity (above 3,000 W mK^{-1}) [9]; optical absorption of exactly $\pi\alpha < 2.3\%$ (in the infrared limit, where α is the fine structure constant) [10]; complete impermeability to any gases, ability to sustain extremely high densities of electric current (a million times higher than copper) [11].

The anisotropy of graphite's material properties continues to fascinate both scientists and technologists. The s, p_x, and p_y atomic orbitals on each carbon hybridize to form strong covalent sp^2 bonds, giving rise to 120 ° C−C−C bond angles and the familiar chicken-wire-like layers. The remaining p_z orbital on each carbon overlaps with its three neighboring carbons to form a band of filled π orbitals, known as the valence band, and a band of empty π^* orbitals, called the conduction band. While three of the four valence electrons on each carbon form the σ (single) bonds, the fourth electron forms one-third of a π bond with each of its neighbors producing a carbon-carbon bond order in

graphite of one and one-third. With no chemical bonding in the *c*-direction, out-of-plane interactions are extremely weak. This includes the propagation of charge and thermal carriers, which leads to out-of-plane electrical and thermal conductivities that are both more than 10^3 times lower than those of their in-plane analogues. Furthermore, the edges of graphene can be described as having armchair or zigzag motifs (Figure 2), with the two edge types leading to different electronic and magnetic properties [12,13]. For the majority of graphene synthesized the edges consist of a mixture of the two motifs, although synthesis of graphene structures with defined edges is a growing area of research given the potential to tune the properties for specic applications [14]. In particular graphene nanoribbons (GNRs); thin strips of graphene, have received a great deal of attention. GNRs with zigzag or armchair configuration, show different electrical property; the zigzag GNRs are metallic, while armchairs can be either metallic or semiconductor. The energy band gap of armchair GNRs are inversely proportional to the width.
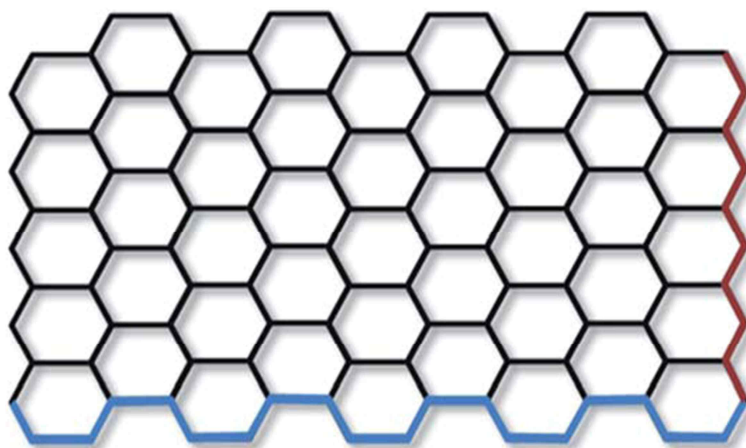
Figure 2. Armchair (blue) and zigzag (red) edges in monolayer graphene. Reprinted with permission from Ref. 12. Copyright 2013 Royal Society of Chemistry.

1.1.2. Synthesis of graphene

Graphene synthesis can be split into two different types of approach; top-down and bottom-up. Top-down approaches involve breaking apart the stacked layers of graphite to yield single graphene sheets, whereas bottom-up methods involve synthesising graphene from alternative carbon containing sources (Figure 3). For top-down methods separating the stacked sheets means that the van der Waals forces that hold the layers together must be overcome, which is not a trivial task despite the relatively low interlayer bonding energy [15]. Key challenges in this area include effectively separating the layers without damaging the sheets, and preventing re-agglomeration of the sheets once the layers have been exfoliated. Top-down approaches generally suffer from low yields, numerous steps, and have the common disadvantage that natural graphite is a finite resource that is on the European list of scarce materials, and requires mining and processing prior to use. Graphite can be produced synthetically under high temperature conditions, but it is not generally suitable for graphene production due to poor levels of graphitisation and irregular morphologies [16,17]. For bottom-up methods high levels of graphitisation must be promoted to produce good quality material, so these methods generally require high temperatures. The processes involved are usually simple, although the material produced can contain higher levels of defects than observed for
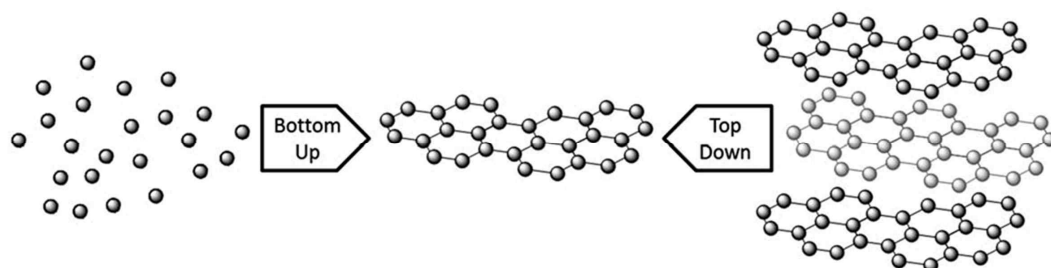
Figure 3. A schematic of 'bottom-up' and 'top-down' graphene synthesis. Reprinted with permission from Ref. 12. Copyright 2013 Royal Society of Chemistry.

top-down methods. In addition to forming graphene nanosheets, bottom-up methods can also be used to form large area graphene flms via growth on certain substrates.

1.1.2.1. Micromechanical cleavage

The exfoliation of graphite is a process in which bulk graphite can be separated into single atomic planes. Attempts prior to development of the so-called "Scotch tape method" were unable to observe isolated single layers. Ever since the first graphene discovered using micromechanical cleavage of bulk graphite, this method has been widely used to prepare high-quality graphene samples, which is less formally called peeled graphene. The technique is quite simple; utilizing everyday adhesive tape to repeatedly peel layers off of highly oriented pyrolytic graphite and pressing it onto an appropriate substrate, typically but not limited to oxidized silicon [18]. The sheets are of high quality as a result of the limited graphite processing required, but the method is slow and labour intensive so the material produced is often reserved for study of the fundamental properties of graphene rather than use in commercial applications.

1.1.2.2. Electrochemical exfoliation

Graphite was used as a sacrificial electrode, and exfoliated material could be collected the from the electrolyte solution. Surfactant and H_2SO_4-KOH solutions were used as electrolytes, which serve different functions [19,20]. Surfactants prevent reagglomeration of the graphene; with the hydrophobic groups interacting with the π-orbitals of graphene, and the hydrophilic groups stabilizing the sheets in water [21]. However, surfactants can be difficult to remove, and their presence has been shown to affect the electrical and electrochemical properties of graphene [22]. Sulfuric acid was a good electrolyte for graphite exfoliation due to intercalation of $[SO4]^{2-}$ ions. However, it is necessary to add KOH to the electrolyte to reduce the high levels of oxidation observed when using only H_2SO_4. In both cases the electrochemical exfoliation produces a mixture of different thicknesses of graphite flakes, with few-layer graphene being isolated by centrifugation.

1.1.2.3. Exfoliation of graphite intercalation compounds (GICs)

Generally, GICs included solvent-assisted and thermal exfoliation. For solvent assisted exfoliation, GICs are sonicated in solution and the intercalation of solvent molecules can expand the layers. Furthermore, interaction with the solvent may cause gas to be expelled that aids exfoliation (Figure 4) [23].
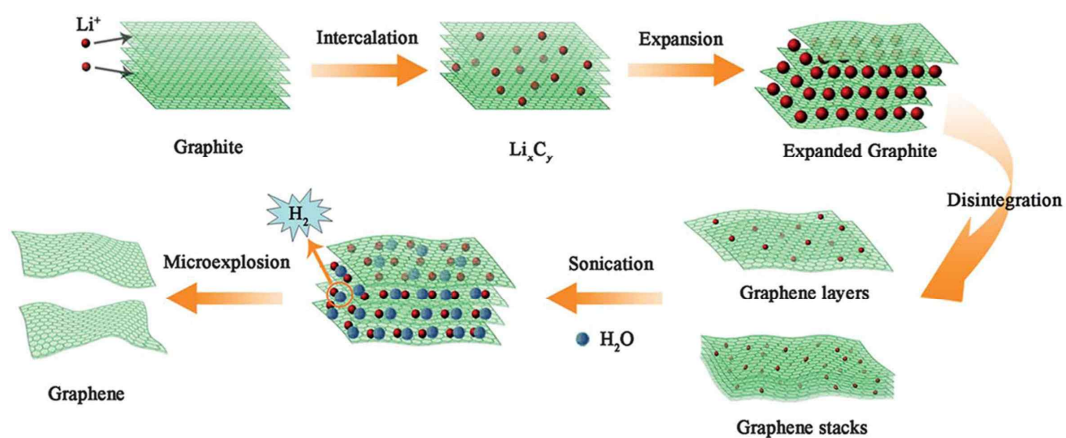
Figure 4. A sketch showing the formation steps of graphene sheets through Li intercalation–expansion–microexplosion processes. Reprinted with permission from Ref. 23. Copyright 2012 Royal Society of Chemistry.

Heating of GICs generally causes thermal decomposition of the intercalates into gaseous species that push the layers apart. The most common method for expanded graphite formation is via the exposure of graphite to strong acids to yield a GIC which is then exfoliated by rapid thermal heating or, more recently, by microwave radiation [24]. Mono- to few-layer graphene has been reported for expanded graphite ground in ethanol, or sonicated in NMP, while repeated cycles of intercalation–exfoliation followed by sonication in DMF has been shown to yield over 50 % mono- and bi-layer graphene [25,26]. Other examples of GICs designed for thermal exfoliation include graphite co-intercalated with iron chloride ($FeCl_3$) and nitromethane (CH_3NO_2), and graphite intercalated with ionic liquid crystals (ILC) [27,28]. In the former iron chloride is used to promote the intercalation of nitromethane, which decomposes at relatively low temperatures (100 °C) under microwave radiation, while in the latter mild heating is used to promote ILC intercalation due to their reduced viscosity at higher temperatures, and stronger heating (700 °C) is used to induce thermal decomposition. Based on a similar principle supercritical carbon dioxide has been used to exfoliate graphite based on intercalation of the CO_2 in the supercritical phase followed by rapid expansion upon depressurization to form gaseous CO_2 which forces the graphitic layers apart [29].

1.1.2.4. Exfoliation of graphite oxide

A more efficient way to obtain large volumes of graphene is by firstly synthesis of graphite oxide, then exfoliation into monolayers, and finally reduction to remove the oxygen [30,31]. The Brodie, Staudenmeier and Hummers methods are the three most common ways to oxidize graphite. Among these, a slightly modified Hummers method has become the most popular in producing graphite oxide, for its relatively shorter reaction time and absence of toxic side products (Figure 5). After oxidation, the interlayer spacing increases from 0.34 nm in graphite to above 0.6 nm, with weakened van der Waals forces between the layers. Exfoliation is typically augmented with sonication, yielding single layers of graphene oxide (GO), which are soluble in water without the assistance of surfactants to form a stable colloidal system. GO is electrically insulating due to the functional groups disrupting the sp^2 hybridisation of the graphene layers, so efficient reduction is an important step in restoring desirable electrical properties of the material. Many methods of removing the oxygen from the GO structure through chemical, [32] thermal, [33] electrochemical [34] or electromagnetic flash [35] and laser-scribe [36] techniques have been successful, but generally resulted in inferior samples which are hence more precisely named reduced graphene oxide (rGO).
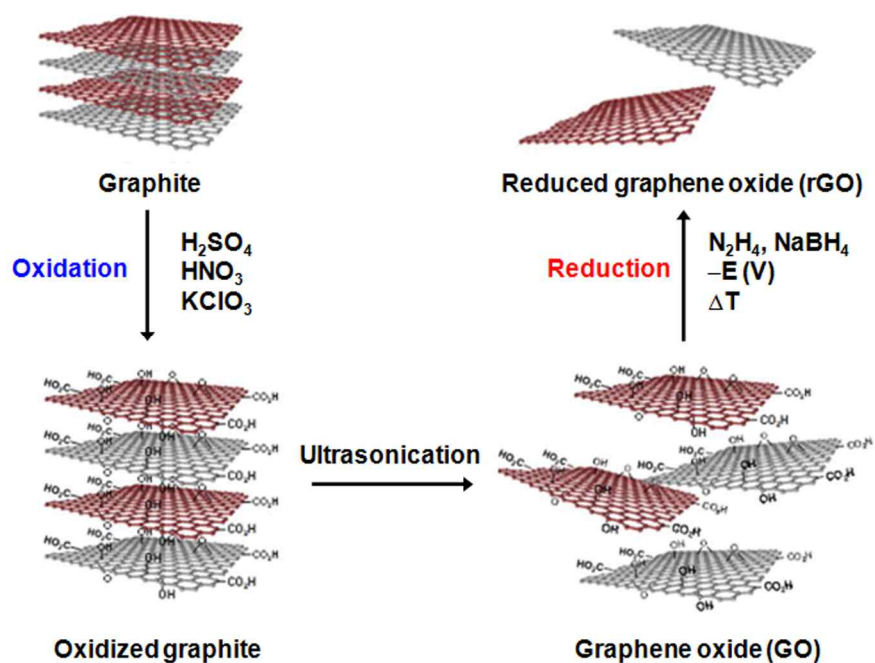
Figure 5. The procedure followed for the production of chemically-modified graphenes using graphite as the starting material. This is followed by: (1) An oxidative treatment is initially performed to generate oxidized graphite; (2) exfoliation by ultrasonication to generate GO; (3) reduction of GO via various reduction methods to produce rGO.

1.1.2.5. Unzipping carbon nanotubes

Graphene can be synthesised by unzipping single or multi-walled carbon nanotubes (MWNTs) respectively using wet chemistry methods such as strong oxidizing agents, or by physical methods such as laser irradiation and plasma etching [37,38]. This unzipping results in graphene 'nanoribbons', with ribbon widths dictated by the diameter of the tubes. It was claimed that MWNTs can be opened up longitudinally by using intercalation of Li and ammonia, followed by exfoliation in acid and abrupt heating [39]. In another study, graphene nanoribbons were produced by plasma etching of MWNTs, partially embedded in a polymer film [40]. The etching treatment basically opened up the MWNTs to form graphene. In a different approach, MWNTs were unzipped by amulti-step chemical treatment, including exfoliation by concentrated H_2SO_4, $KMnO_4$ and H_2O_2, stepwise oxidation using $KMnO_4$ and finally reduction in NH_4OH and hydrazine monohydrate ($N_2H_4.H_2O$) solution [41]. This new process route of unzipping MWNTs to produce graphene creates possibilities of synthesizing graphene in a substrate-free manner. GNRs are considered as quasi one dimensional materials, and have different properties depending on their width and edge type (armchair/zigzag) [42]. Carbon nanotube unzipping occurs via C–C bond fission which is often initiated at defect sites, leading to irregular cutting [43].

1.1.2.6. Epitaxial growth on silicon carbide

The formation of graphene on silicon carbide (SiC) proceeds via the preferential sublimation of silicon from the SiC surface and subsequent graphitisation of the excess carbon atoms left behind [44]. This process occurs at high temperatures (> 1000 °C) and is generally performed in ultra-high vacuum (UHV) conditions, although growth in argon atmospheres or in the presence of small quantities of disilane has been shown to reduce the rate of silicon sublimation, allowing higher temperatures to be used which results in higher quality graphene [45,46]. Preferential Si sublimation can also be induced by pulsed electron irradiation (Figure 6) [47].

One of the highly popular techniques of graphene growth is thermal decomposition of Si on the (0001) surface plane of single crystal of 6H-SiC [48]. Graphene sheets were found to be formed when H_2-etched surface of 6H-SiC was heated to temperatures of 1250 to 1450 °C, for a short time (1 to 20 minutes). Graphene, epitaxially grown on this surface, typically had 1 to 3 graphene layers; the number of layers being dependent on the decomposition temperature. In a significant development to this technology, continuous films (mm scale) of graphene were synthesized on a Ni thin film coated SiC substrate, at a quite lower temperature (750 °C) [49]. This process has the added advantage of continuity of graphene film over the entire Ni-coated
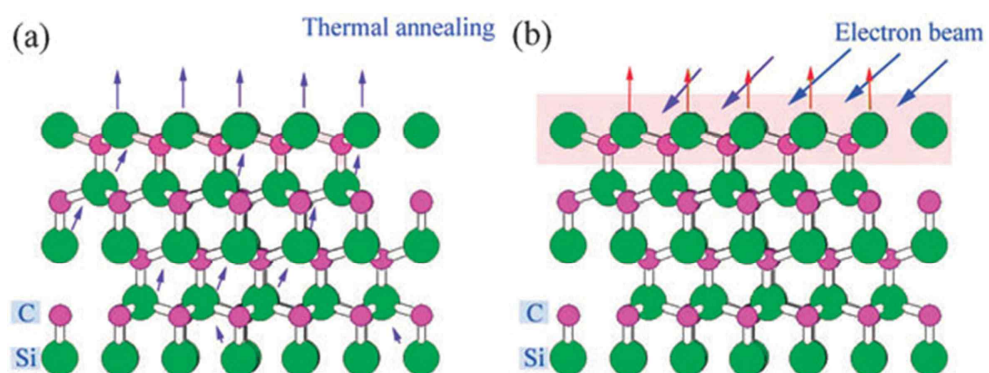
15

Figure 6. Schematic description of Si atom sublimation in Si-terminated 4H–SiC under a) thermal annealing process, b) pulsed electronic beam irradiation process. Reprinted with permission from Ref. 47. Copyright 2010 Royal Society of Chemistry.

surface. Large area production of graphene makes this route favorable for industrial application. In a similar process, Emtsev et al. have shown synthesis of large-size, monolayer graphene films at atmospheric pressure [50]. The method was predicted to produce wafer-size graphene films. While this method uses lower temperatures, it has the additional cost of using a transition metal and requires transfer to insulating substrates for use in electronic applications.

1.1.2.7. Chemical vapor deposition

Chemical vapor deposition (CVD) method has emerged to be one of the most promising techniques for the large-scale production of single and multiple layer graphene films. Uniform, wafer size graphene films have been grown on both single crystal and polycrystalline transition metal surfaces at high temperatures by pyrolysis of hydrocarbon precursors such as methane [51–53]. Figure 7 shows the largest continuous area of CVD graphene reported to date: 30-inch diagonal length, grown on copper foil in an 8-inch diameter quartz tube at low pressure [54]. The number of graphene layers depends highly on the carbon solubility of the substrate. For metals with relatively high carbon solubility, such as nickel, [55] the carbon atoms can dissolve at high temperature, then precipitate onto the metal surface and form single or multilayer graphitic films upon cooling. These non-uniform films with a wide
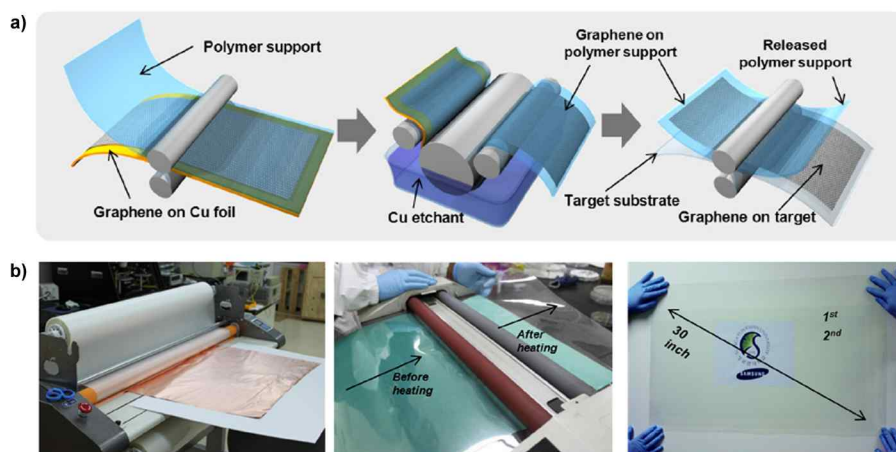
Figure 7. a) Schematic diagram of the roll-based production of graphene films grown on a copper foil. The processes are divided into three steps: (1) the adhesion of polymer supports, (2) copper etching and (3) transfer to the target substrate. b) Photographs of the roll-based production of graphene films on copper foil produced by the process shown in panel (a). Reproduced with permission from Ref. 54. Copyright 2010 Right Managed by Nature Publishing Group.

thickness range from 1 to around 10 layers with monolayer domain sizes up to several tens of micrometers in diameter were produced on nickel substrates [56]. The thickness and crystal ordering can be controlled by the cooling rate and hydrocarbon gas concentration. On the other hand, low carbon solubility in certain transition metals, for instance copper [57] and platinum [58] enables complete monolayer coverage [59].

Lattice mismatch between the metal surface and graphene typically forms a pseudomorphic interface and generally displays a moiré pattern as well as lattice strain. Graphene epitaxially grown on single crystal metal substrates can avoid surface defects on the metal grain boundaries and help to mitigate orientation mismatch, however still has significant misaligned domains and grain boundaries. Polycrystalline films offer a more economical alternative that is still capable of large domains without noticeable performance difference within individual domains.

Yan and coworkers broke the self-limiting effect of the low pressure chemical vapor deposition (LPCVD) process to enable second layer growth on prepared monolayer graphene using a fresh copper foil placed in the high-temperature upstream regime. Bernal AB-stacked bilayer graphene is possible with coverage area as high as 67%, which shows typical gate response [60]. Furthermore, Chen and coworkers report the synthesis of controllable mono-

and multilayer graphene films on Cu 0.69 Ni 0.31 alloy foils by LPCVD. By using the alloy of low- and high-solubility catalysts, both thickness and quality of the films can be controlled by the growth temperature and cooling rate [61].

The recent achievements in graphene growth by thermal CVD has confirmed reproducibility of good quality graphene on a centimeter scale substrate and successful transfer to many other substrates including Si, glass and polydimethylsiloxane (PDMS). These developments create new pathways for application of graphene in photovoltaic and flexible electronics. However, in near future, issues like growth of graphene on wafer size substrates, controlling efficiently the number of layers should be solved, for creating more interest in actual applications.

Substrate free synthesis has the advantage that the removal of graphene from the substrate is not required. Furthermore as the material is collected outside the furnace, graphene can be produced via continuous rather than batch processing. An early example of substrate free growth is the work by Dato et al., where the growth of single and bilayer graphene has been reported via atmospheric pressure, microwave enhanced CVD of ethanol [62,63]. More recently a route to produce few-layer graphene via substrate free CVD has been demonstrated using thermal decomposition of sodium ethoxide in ethanol [64]. Both methods yield large quantities of graphene.

1.1.2.8. Chemical synthesis

Another alternative route for the controllable production of graphene is bottom-up organic synthesis. Graphene can be composed of interconnected polycyclic aromatic hydrocarbons (PAHs), which are very small two-dimensional graphene segments. This approach is attractive due to its high versatility and compatibility with various organic synthesis techniques [65]. Müllen and coworkers are pioneers in this field, reporting synthesis of nanoribbon like PAHs with lengths over 30 nm [66,67]. Recently, the largest stable colloidal graphene quantum dots were synthesized using a benzene-based chemical route, which compose 132, 168, 170 conjugated carbon atoms [68,69]. However, the size of the as-grown graphene dots is limited due to decreasing solubility as sizes increase as well as an increasing number of possible side reactions, which is still a major challenge for organic synthesis of graphene molecules with controllable shapes, sizes and edge structures.

1.1.3. Application fields

Graphene has shown exceptional electrical, optoelectrical, mechanical and chemical properties and thus, has emerged to be a valuable platform for various applications. Graphene is intrinsically metallic and can be found in a number of promising applications utilizing it as a passive conducting component. Most of all, graphene thin films can be utilized for electrode of electronic device via solution process such as spin coating, drop casting, spraying, printing technology, electrophoretic deposition and Langmuir-Blodgett methodologies, etc,. However, the sheet resistance of an undoped pristine graphene monolayer is around 6 kΩ/sq [70]. The conductivity can be increased by using electrostatic or chemical doping, to increase carrier concentration. Additional advantages include its exceptional transparency, surface area, mechanical strength and flexibility.

Exceptional electrical properties of graphene have attracted applications for future electronics such as ballistic transistors, field emitter, components of integrated circuits, transparent conducting electrodes and sensors. Graphene has a high electron (or hole) mobility as well as low Johnson noise (electronic noise generated by the thermal agitation of the charge carriers inside an electrical conductor at equilibrium, which happens regardless of any applied voltage), allowing it to be utilized as the channel in a field effect transistor

(FET). Combination of excellent electrical property and low noise make graphene an excellent sensor. Its entire volume is exposed to the surrounding due to its 2D structure, making it very efficient to detect adsorbed molecules. The high electrical conductivity and high optical transparency promote graphene as a candidate for transparent conducting electrodes, required for applications in touch-screens, liquid crystal displays, organic photovoltaic cells and organic light-emitting diodes (OLEDs) [71].

The quantity and form of graphene required varies according to the application; while some applications such as transparent electrodes and sensors require thin films of graphene, other applications such as energy storage devices (such as batteries and supercapacitors) and polymer composites require relatively large quantities of graphene nanosheets or platelets. It is logical to categorize these by the quality of the resulting graphene and thus the possible applications: (1) graphene or reduced graphene oxide flakes for composite materials, conductive paints, and so on; (2) planar graphene for lower-performance active and non-active devices; and (3) planar graphene for high-performance electronic devices. The properties of a particular grade of graphene depend very much on the quality of the material, type of defects, substrate, and so forth, which are strongly affected by the production method (Figure 8) [72].
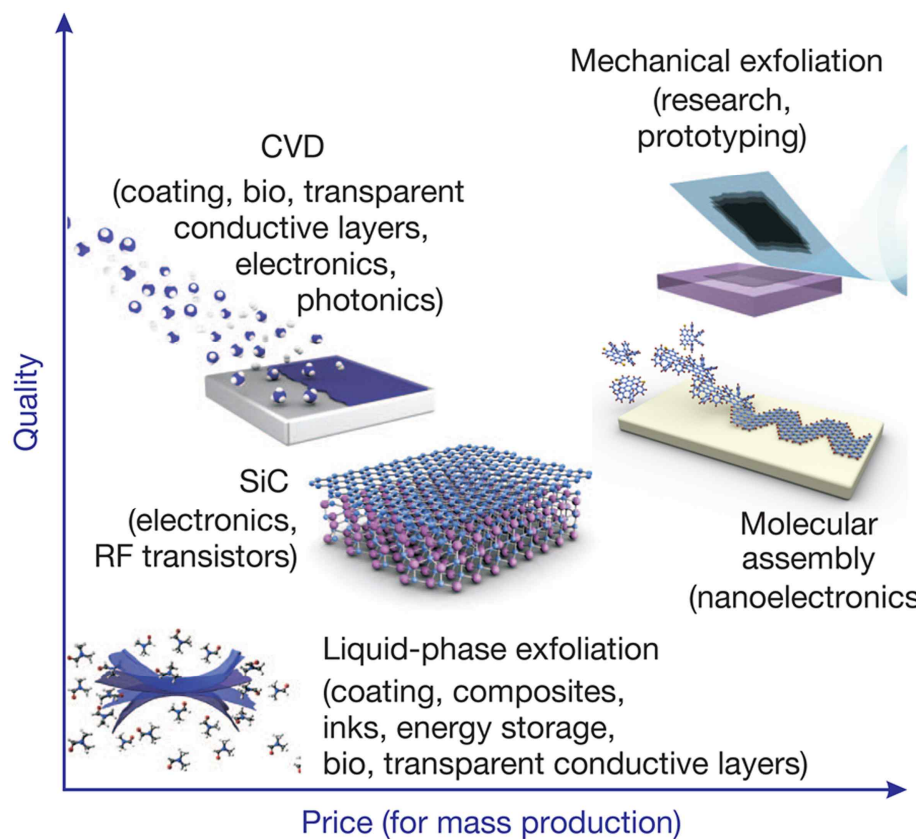
Figure 8. There are several methods of mass-production of graphene, which allow a wide choice in terms of size, quality and price for any particular application. Reproduced with permission from Ref. 72. Copyright 2012 Right Managed by Nature Publishing Group.

1.1.3.1. Transparent electrode

The most soon-to-be realized application is the use of graphene thin film as a transparent electrode. Currently, the touch screen and electrode fields are dominated by the use of indium tin oxide (ITO). When compared to graphene, ITO is easy to handle and tends to outperform graphene in terms of conductance and low sheet resistance at the current stage [73]. However, high cost, limited supply and brittle nature of indium restricts its application in flexible substrate, motivating the search for highly transparent and conducting materials to replace ITO. Therefore, graphene quality is expected to improve with the fine tuning of its synthesis process and its electrical properties are still at an acceptable level for several applications. Given this, graphene's mechanical resilience, flexibility, and high transparency play important roles in establishing graphene as the new revolutionary material [74].

Demonstration of a graphene based touch screen first done by Bae et al., which renders a graphene based electronics market something quite realistic [54]. A palm-sized touch screen was made with a CVD grown graphene sheet. Even when the graphene sheet was predominantly single layer (this corresponds to the achievement of ~97% transmittance), it showed remarkable resilience upon bending and when written on with a touch screen pen. Bolstered by the roll-to-roll production possibility of graphene sheets on a

large scale and given the reliable performance of the graphene touch screen, such industrial advancements seem very much feasible.

Recently K. Kim et al. reported 80% transmittance from the graphene grown on a 300 nm thick nickel layer, corresponding to 6 to 10 graphene layers [75]. The transmittance was increased up to 93% by further reducing the growth time and nickel thickness, resulting in formation of thinner graphene film. For microelectronic application, high mobility and excellent mechanical properties of transparent graphene film are useful to make flexible and stretchable electrodes. Zhi et al. fabricated the large-area (4.5 inch) of uniform reduced graphene oxide films for flexible touch screens via rod coating (Figure 9) [76]. The uniformity of the sheet resistance of the prepared graphene films was compatible with industry expectations, exhibiting a standard deviation of 3.7–9.8% over 100 cm^2. It showed not only a linearity comparable to ITO-based touch screens, but also a high mechanical flexibility exceeding that of ITO-based touch screens. Many types of electronics could find their way into bendable devices, such as displays, data storage, sensors, solar cells, wearable nanogenerators, and energy storage. Printable devices utilizing graphene-based conductive inks offer a relatively inexpensive and scalable approach to fabricating flexible electronics [77].
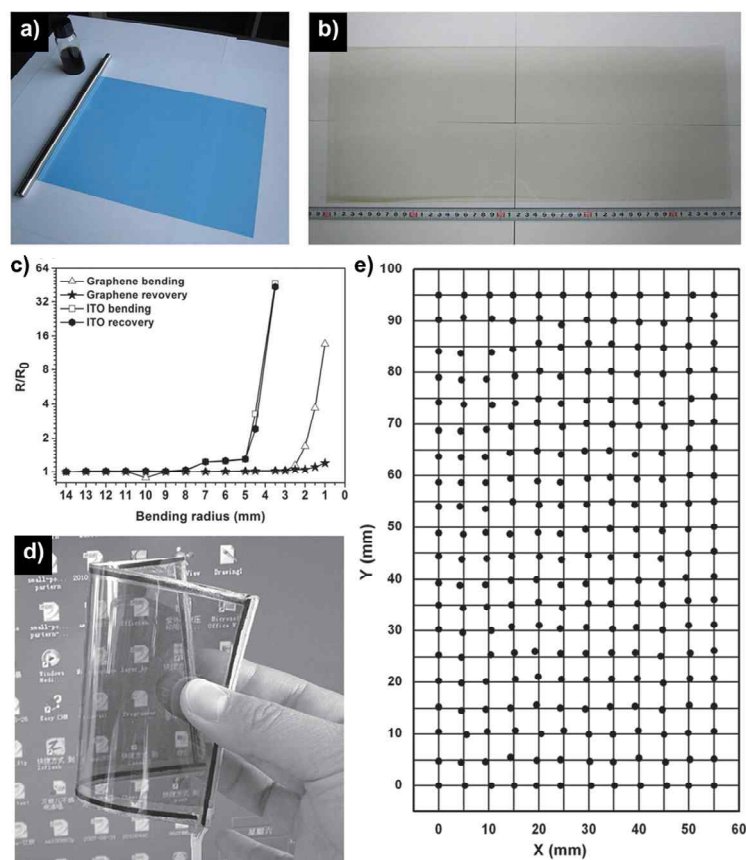
Figure 9. a) Fabrication of graphene film by Meyer rod coating and b) Photograph of a large-scale graphene film. c) The resistance change with tensile strain applied to RGO and ITO films on PET substrates under bending and unbending conditions. d) A flexible four-wire resistance touch screen fabricated using graphene electrodes. e) Linearity test of NC-FTS-1. The intersections of the lines indicate the practical touch points, and the black dots indicate the detected points. Reproduced with permission from Ref. 87. Copyright 2010 Wiley-VCH Verlag GmbH & Co. KGaA.

1.1.3.2. Transistors

FET is one of the potential applications of graphene. Graphene is unique as a channel material, because unlike other semiconductors, graphene does not require impurity doping to conduct electricity. In particular, graphene presents the phenomenon of self-doping [78]. Self-doping refers to the electric field effect in graphene, which allows the charge carrier type and concentration to be controlled with an outside electric field, or rather gate voltage. Graphene-based FET devices with a single back gate have been investigated, and experimental values of the field-effect mobility of graphene are one order of magnitude higher than that of silicon (Si) [79,80].

Organic field-effect transistors (OFET) with patterned single graphene sheet as source and drain electrodes were prepared using microcontact printing (μCP) [81]. A single graphene sheet was transferred to various substrates in a pattern defined by the geometry of the PDMS stamp. With single crystalline rubrene as an active channel, the devices exhibited excellent p-type characteristics. The highest mobility of transferred rubrene transistor was of 10.3 cm^2/Vs with approximately 10^7 of on/off ratio. It could be explained that the low Schottky barrier between single graphene layer and rubrene crystal led to excellent output curves showing up to 100 μA at a gate voltage of –20 V. Recently, Cho *et al.* reported a promising route to the fabrication of an all-

graphene-based FET array on a flexble polymer substrate using using solution-processable, high-capacitance ion gel gate dielectrics (Figure 10) [82]. A CVD grown graphene film was transferred onto pre-patterned Au source/drain (S/D) electrodes and was isolated to make a channel region. Subsequently, ion-gel was spread as a dielectric layer and this process was followed by gate electrode deposition. The graphene FETs fabricated on the plastic substrates showed a hole and electron mobility of 203 ± 57 and 91 ± 50 cm^2/(V·s), respectively, at a drain bias of -1 V. Moreover, ion gel gated graphene FETs on the plastic substrates exhibited remarkably good mechanical flexibility. This method represents a significant step in the application of graphene to flexible and stretchable electronics.
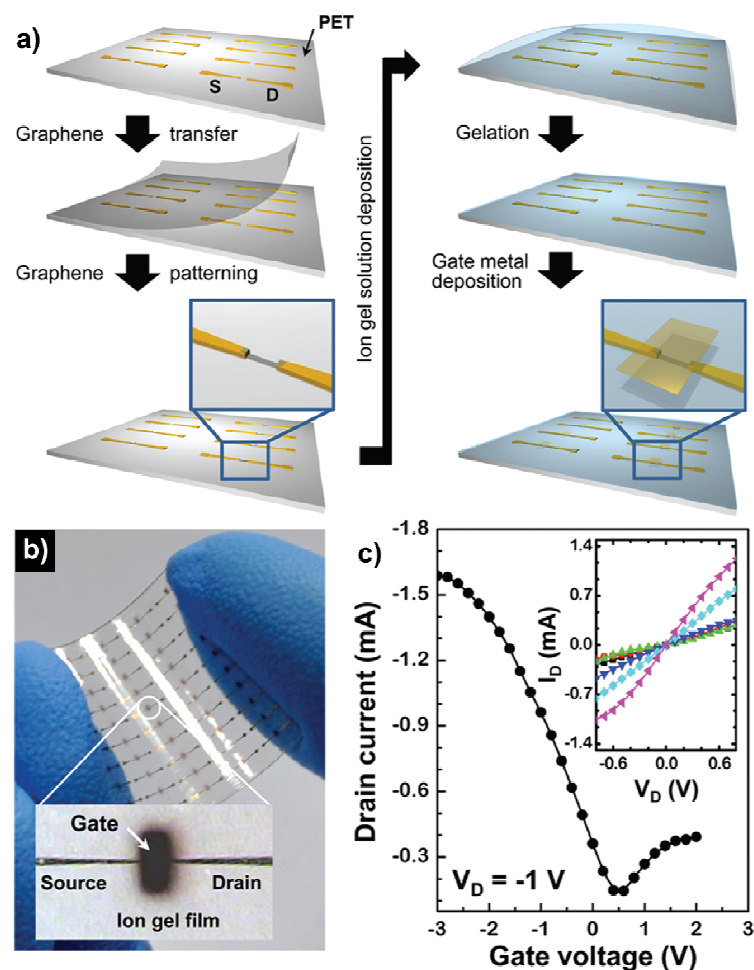
Figure 10. a) Schematic diagram of the steps used to fabricate the ion gel gated graphene transistor array on a plastic substrate. b) Optical images of an array of devices on a plastic substrate. c) Transfer and output characteristics of graphene FETs on plastic substrate. In output curve, the gate voltage was varied between +2 and –3 V in steps of –1 V. Reprinted with permission from Ref. 82. Copyright 2011 American Chemical Society.

1.1.3.3. Chemical/Bio sensor

One of the most promising applications of graphene is in sensors, including chemical and bio sensors. The operational principle of graphene is based on the change of graphene's electrical conductivity (σ) due to adsorption of molecules on graphene surface [83]. The change in conductivity can be attributed to the change in carrier concentration of graphene due to the absorbed gas molecules acting as donors or acceptors. Furthermore, some interesting properties of graphene aid to increase its sensitivity up to single atom or molecular level detection. First, graphene is a two-dimensional (2D) material and its whole volume i.e., all carbon atoms are exposed to the analyte of interest [84]. Second, graphene is highly conductive with low Johnson noise (electronic noise generated by the thermal agitation of the charge carriers inside an electrical conductor at equilibrium, which happens regardless of any applied voltage), therefore, a little change in carrier concentration can cause a notable variation of electrical conductivity. Finally, four-probe measurements can be made on single crystal graphene device with ohmic electrical contacts having low resistance [85,86]. Owing to these characteristics, various graphene-based sensors have been developed for both chemical and biological uses.

For example, a rugged and flexible graphene-based sensor was fabricated using inket printing technique, followed by patterning of rGO onto flexible

PET substrate (Figure 11) [87]. When inkjet-printed rGO/PET films are exposed to electron- withdrawing vapors, the conductivity increases drastically. The sensing performance of the rGO/PET sensor is attributed to the effective adsorption of NO_2 vapors on the rGO surface. In general, the NO_2 is a strong oxidizer with electron-withdrawing ability. Accordingly, electron transfer from rGO surface to adsorbed NO_2 vapors leads to enriched hole concentration and enhanced electrical conduction in the rGO/PET sensor. Consequently, it can be considered that the rGO/PET sensors can reversibly and selectively detect the general class of electron-withdrawing vapors such as NO_2, Cl_2, etc.

Recently, Shan et al. has demonstrated biosensing, i.e., glucose properties of graphene [88]. With glucose oxidase (GOD) as an enzyme model, Shan et al. and their group constructed a novel polyvinylpyrrolidone protected graphene/polyethylenimine-functionalized ionic liquid/GOD electrochemical biosensor. Through the sensor, they reported direct electron transfer of GOD, demonstrating graphene's potential application for fabrication of glucose sensors. A linear response up to 14 mM of glucose was observed in their work. Furthermore, Alwarappan et al. has demonstrated that graphene electrodes exhibited a superior biosensing performance toward dopamine detection in the presence of common interfering agents, such as ascorbic acid and serotonin [89].
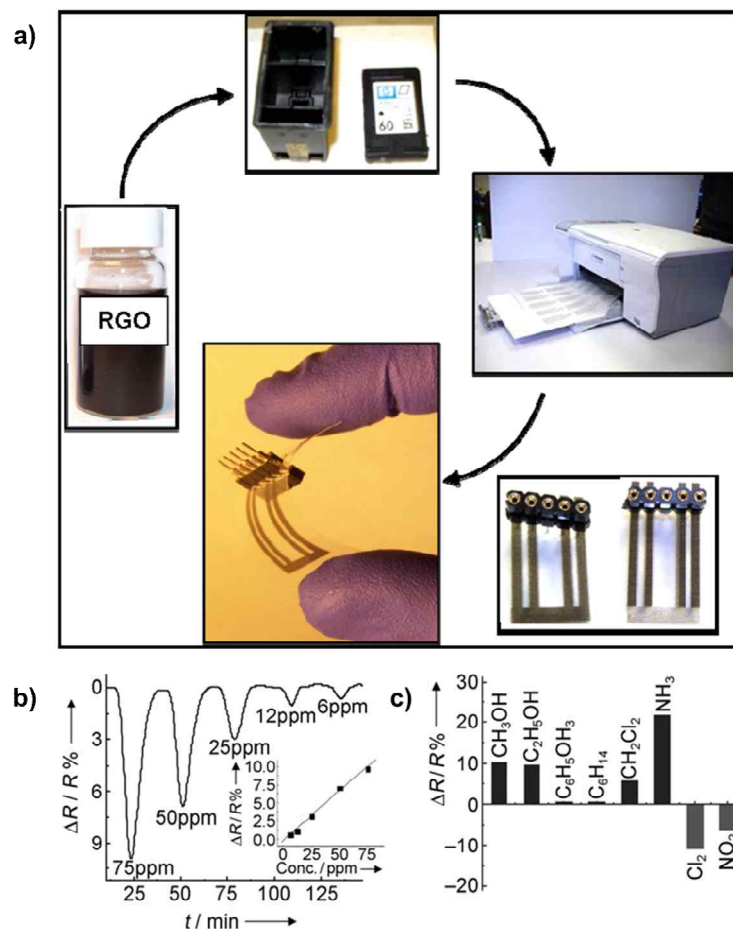
Figure 11. a) Sensor fabrication procedure. Inset: Digital images of thick (left) and thin (right) bottom strips inkjet printed sensors. Vapor sensing by inkjet-printed rGO/PET obtained by ascorbic acid reduction of dispersed graphene oxide. b) Plot for resistance versus time when the film was exposed to a Cl_2 vapor. Inset: Plot of resistance versus vapor concentration. c) Selectivity plot: sensor exposed to saturated organic vapors, NH_3 (100 ppm), NO_2 (100 ppm), and Cl_2 (100 ppm). Reproduced with permission from Ref. 87. Copyright 2010 Wiley-VCH Verlag GmbH & Co. KGaA.

1.1.3.4. Supercapacitor

Graphene also competes with its carbon relatives to make better supercapacitors. It is important that the material acting as electrochemical double layer used in the capacitor provide high specific surface area and high conductivity [90,91]. Previously used activated carbon materials had high surface area but low conductivity. Carbon nanotube based supercapacitors also showed limitations of high contact resistance between carbon nanotube and the current collector. The specific surface area of a single graphene sheet is 2630 m^2 g^{-1}, larger than that of activated carbon and carbon nanotubes. These superior characteristics make graphene a most promising material for supercapacitors [92–94]. In addition, its mechanical strength and flexibility are attractive as conformal electrode materials particularly for flexible supercapacitors.

Using chemically reduced GO in hydrazine provided high conductivity, large specific surface area and chemical stability, resulting in specific capacitance of up to 205 F/g in aqueous electrolyte [95]. Other supercapacitors were fabricated from chemically modified graphene with high surface area and achieved specific capacitances of 135 and 247 F g^{-1} in aqueous electrolytes [96,97]. A facile fabrication of graphene-based supercapacitor was developed using direct laser writing of micro-supercapacitors on hydrated GO films [98].

This technique provides the patterning of GO surface into rGO–GO–rGO structures in various geometries with micrometer resolution. Both in-plane and conventional sandwich electrodes with reduced graphite oxide were also patterned (Figure 12). The as-prepared laser-patterned devices (rGO–GO–rGO) demonstrated the excellent electrochemical performance without the use of an external electrolyte. The substantial amounts of trapped water in the graphite oxide made it simultaneously a good ionic conductor and an electrical insulator. A very interesting route to graphene-based electrode has been proposed by directly patterning the graphite on cellulose paper [99]. The shear peeling method was introduced in order to increase the graphite surface area for supercapacitor application. The rough surface structure of paper enabled the exfoliation and adhesion of the graphitic materials. It formed continuous conducting paths on the surface, and provided significant adsorption area for double layer formation. As a result, the patterning of graphite on paper produced multilayer graphene with a large portion of edge structures. The as-fabricated paper supercapacitor demonstrated stable long cycling performance with 90 % capacity retention after 15,000 cycles and a high areal capacitance of 2.3 mF cm^{-2}. In addition, the solvent-free deposition technique represented a low cost, environmentally friendly, highly scalable and versatile fabrication method for integrated paper-based energy devices.
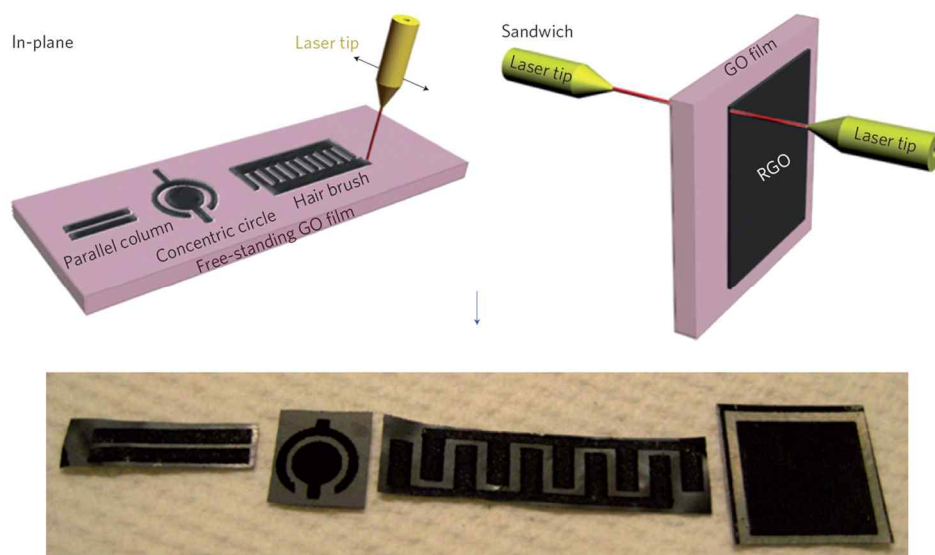
Figure 12. Schematics of CO_2 laser-patterning of free-standing hydrated GO films to fabricate rGO–GO–rGO devices with in-plane and sandwich geometries. The black contrast in the top schematics corresponds to rGO, and the light contrast to unmodified hydrated GO. For in-plane devices, three different geometries were used, and the concentric circular pattern gives the highest capacitance density. The bottom row shows photographs of patterned films. Reprinted with permission from Ref. 98. Copyright 2011 Right Managed by Nature Publishing Group.

1.2. Objectives and Outline of the Study

1.2.1. Objectives

In the preceding section, the importance of graphene thin films were introduced from the viewpoint of academic research and practical applications. The aim of this dissertation is to present synthetic methodologies to fabricate the various graphene mateirals and flexible graphene thin films via solution process such as inkjet and screen printing. Furthermore, the properties of the graphene thin films are systematically investigated, and their application fields are also explored, including transparent electrode, acoustic actuator, RFID antenna and patch heater.

1.2.2. Outline

This dissertation involves the following subtopics:

I. Chemically Exfoliated Graphene Thin Films via Inkjet Printing and Their Application

  1. Micropatterning of graphene sheets by inkjet printing and its wideband dipole-antenna application

  2. Flexible and transparent graphene films as acoustic actuator electrodes using inkjet printing

II. Size-Controlled Graphene Thin Films via Screen Printing and Their

Application

1. Graphene size control via mechanochemical method and their electro-responsive properties

2. Highly conductive, flexible and scalable graphene hybrid thin films with controlled domain size as transparent electrodes

III. Multilayered Graphene Thin Films via Screen Printing and Their Application

1. High electrothermal performance of expanded graphite nanoplatelet-based patch heater

IV. Graphene/Polyaniline Thin Films via Screen Printing and Their Applications

1. Graphene/polyaniline/poly(4-styrenesulfonate) hybrid film with uniform surface resistance and its flexible dipole tag-antenna application

2. Fabrication of highly scalable graphene/polyaniline thin film with enhanced electrical and mechanical property and its monopole antenna application

A detailed outline of the study is as follows:

1. Patterned graphene sheets on flexible substrate were successfully fabricated via inkjet printing and vapor deposition process. Importantly, the hydrophilic property of GO solution could make it possible to overcome the limitations on conductive ink preparation to be printed through a nozzle including optimization of suitable solubility, viscosity and surface tension. Prepatterned GO was transformed into a few layers of graphene sheet with reduction process. Patterned graphene line had much higher resolution compared to the other conducting polymers. Furthermore, the graphene-based thin film exhibited sustained electrical conductivity, and manipulating gradient pattern offered an attractive opportunity to control the sheet resistance at designed positions. In this study, the graphene-based thin films were applied for the electrodes of practical wideband dipole antenna and transparent flat-panel speaker. The simple inkjet printing method offered a great possibility to fabricate the graphene films in the large quantities without the loss of printing materials.

2. Highly dispersible GO sheets with controlled domain size were successfully synthesized by using a mechanochemical method. The domain size of the GO sheets was easily controlled by adjusting the ball-milling time, and it transformed the morphology of the GO sheets into a spherical

form. The effect of the GO size and morphology on the electrorheological activity was investigated as a function of the shear rate, GO volume fraction, and electric field strength. Such a simple route to control the graphene domain size with uniformity will open immense opportunities for advances in graphene commercialization with high quality, scalable production. Moreover, flexible graphene thin films with controlled domain size were successfully fabricated in the large-scale via screen printing and pressure-assisted reduction process for transparent electrodes. Importantly, as a connecting bridge, submicrometer-sized graphene sheets increased the dispersibility and the interfacial interactions between graphene sheets with micrometer size, which caused the increase in conductivity related to the high reduction efficiency. In this study, the graphene hybrid thin films exhibited uniform conductivity and outstanding flexibility.

3. Sub-kilogram quantities of expanded-graphite nanoplatelets (EGnP), composed of multilayered graphene, have been synthesized via intercalation derived from the mild oxidation of graphite with an oxidizing agent and acid, expansion using sonication, and vacuum filtration. In addition, micropatterned EGnP-based line heaters were prepared by screen printing. The EGnP-based line heaters exhibited sustained electrical and thermal conductivity, and consumed much less power compared to other

graphene-based heaters. The trapped water in EGnP makes it a good ionic conductor, while allowing it to serve as an electrolyte with ion transport characteristics. Furthermore, the steady-state temperature of the EGnP-based line heater could be controlled by manipulating the applied voltage and bending radius. Most importantly, the properties of EGnP synthesized by simple step oxidation process and its ease of use in the design of heaters of a particular shape and size by screen printing suggests its feasibility as a cheap, lightweight patch heater for industrial application.

4. Graphene/conducting polymer hybrid thin film with uniform surface resistance and outstanding flexibility was successfully fabricated via screen printing. The polyaniline/poly(styrene-sulfonic acid) (PANI/PSS) nanofiller was inserted into the multilayer graphene matrix by mechanical blending. High concentrations of PSS resulted in a hybrid film with good electrical connectivity and good adhesion to a flexible substrate. Changes in surface resistance as a function of graphene content, hybrid thin film thickness, and the response of the films to repeated bending were evaluated, and it was applied to the dipole tag antenna. Moreover, graphene (G)/PANI thin films were prepared via in-situ polymerization and screen printing. Most of all, the strong $\pi - \pi$ interaction between the graphene and the PANI caused more compact packing of the PANI chains by inducing more fully

expanded conformation of the PANI chains, leading to improvement in the mechanical, electrical property and permittivity. High conductivity and permittivity G/PANI thin films made it possible to have a high efficient monopole antenna with smaller size.

2. EXPERIMENTAL DETAILS

2.1. Chemically Exfoliated Graphene Thin Films via Inkjet Printing and Their Applications

2.1.1. Micropatterning of graphene sheets by inkjet printing and its wideband dipole-antenna application

The graphite flakes used in the majority of experiments was purchased from Sigma-Aldrich (Product Number 332461). GO was printed using a commercial office inkjet printer (Canon Pixima IP1300). Poly (ethyleneterephtalate) (PET, 3M) film was used as a substrate for inkjet printing. Aniline monomer (99%) and ammonium persulfate (APS, 98%) were obtained from Sigma Aldrich Co. Ltd, and pyrrole monomer (99%) was obtained from Acros Organics and used without further purification. Hydrochloric acid (HCl, 35 wt.% in H_2O) was purchased from Samjun Chem. Co. and used for doping of PANI.

GO was synthesized from natural graphite by a modified Hummers and Offeman method as originally presented by Kovtyukhova and colleagues. Synthesized purified GO suspensions were dispersed in water. Exfoliation of GO was achieved by sonication of the dispersion for 3 h to avoid the nozzle blockage. The obtained brown dispersion was then washed for 5 cycles of centrifugation at 3,000 rpm to remove any unexfoliated graphite oxide.

The ink cartridge (printer head) was disassembled and washed several times by ethanol and distilled water after removing all inks. The exfoliated GO in distilled water was injected into the modified cartridge as an alternative ink. Subsequently, the completely sealed ink cartridge was placed in the printer body and prepared to use for further experiments.

For patterning of graphene sheets onto the PET film, oxygen plasma treatment was performed in order to modify the surface energies of target substrate (gas flow rate: 20 sccm, power: 100 W, time: 20 s). The complex patterned architectures were designed by computer software in advance (Microsoft PowerPoint 2003). The exfoliated GO solution was printed on the flexible PET film as the designed images using the modified inkjet printer. Subsequently, the printed film was properly cut and located in VDP chamber containing hydrazine and ammonia solution. The graphene sheets patterns were formed immediately at low temperature (90 $^\circ$C, 1 h).

For patterning the conduction polymers such as polypyrrole (PPy) and polyaniline (PANI), oxidant agent APS 0.15g in distilled water (5 mL) was injected into the modified cartridge as an alternative ink. In the case of PET film, low temperature oxygen plasma treatment (gas flow rate: 20 sccm, power: 100 W, time: 20 s) was also conducted to increase the hydrophilic property of surface. The oxidant APS solution was printed on the PET film as the designed

images. Subsequently, the patterned oxidant was properly cut and located in the vapor deposition (VDP) chamber containing pyrrole and aniline monomer (1mL). In case of patterned PANI, dilute hydrochloric acid solution (1 mL of HCl solution in 10 mL distilled water) was also added in the VDP chamber. Immediately, the patterned PPy and emeraldine salt form of PANI were fabricated by thermal treatment (90°C).

A 300 nm thick, 300×30 mm rectangle GO film on glossy photo paper treated with oxygen plasma was obtained by inkjet printing repeatedly for 30 times. The rectangle GO/PET section was cut using scissors and placed at 90°C VDP chamber with hydrazine and ammonia solution for 1 h. Patterned graphene sheets of dipole antenna were connected by silver paste to the power supply source.

Transmission electron microscopy (TEM) image was taken with a JEOL 6700F and the X-ray photoelectron spectroscopy (XPS) spectra were recorded using Kratos Model AXIS-HS system. Field-emission Scanning electron microscope (FE-SEM) images were acquired with JSM-6700F microscope (JEOL, Tokyo, Japan) at an acceleration voltage of 10 keV, and the atomic force microscopy (AFM) topography of the GO solution deposited on Si wafer was obtained by a Digital Instrument Nanoscope IIIA from veeco systems in tapping mode using silicon tips with a resonance frequency of of 320 KHz.

Raman spectrum was obtained on a Jobin-Yvon T64000 spectrometer. Optical micrographs were taken using a Leica DM2500 P and the plasma reactor was the parallel electrode type with a 13.56 MHz radio-frequency generator. The viscosity was measured by rheometer (AR 2000 Advanced Rheometer, TA Instruments) and the surface energy was calculated by Owens-Wandt equation after measuring the contact angle of distilled water droplet on the film surfaces. Analysis of the static contact angles was carried out using a DSA 100 drop shape analysis system (Kruss GmbH). The measurement of electrical resistances was performed with a Keithley 2400 sourcemeter at 25 $^{\circ}$C by a four-probe method. The sheet resistance was measured at 10 different locations of graphene sheets based films and calculated as an average value. For the Radio Frequency Identification (RFID) antenna characteristics, E5071B ENA RF Network Analyzer of Agilent Technologies was carried out (300 kHz to 8.5 GHz). Impedance was plotted on the smith chart by first normalizing to the characteristic impedance of the system (50 ohms).

2.1.2. Flexible and transparent graphene films as acoustic actuator electrodes using inkjet printing

The GO was printed using a commercial office inkjet printer with a piezo-based print-head (dispenser system) with an inner diameter of 50 μm. The driving voltage applied to the piezo was 24 V and the dot spacing, which was the center-to-center distance between two adjacent droplets, was *ca.* 70 μm. Poly (vinylidene fluoride) (PVDF, Fils Co., Ltd) with 60 μm thickness was used as a substrate for inkjet printing.

The ink cartridge (printer head) was disassembled and washed several times by ethanol and distilled water after removing all inks. The exfoliated GO in distilled water (0.1 wt%) was injected into the modified cartridge as an alternative ink. Subsequently, the completely sealed ink cartridge was placed in the printer body and prepared to use for further experiments.

For fabricating of graphene onto the PVDF film, low-temperature oxygen plasma treatment was performed in order to modify the surface energy of PVDF substrate (gas flow rate: 20 sccm, power: 100 W, time: 120 s at 5 $^{\circ}$C). The 10×10 cm rectangular architectures were designed by computer software in advance (Microsoft PowerPoint 2003), and GO ink printed on both sides of the PVDF film by inkjet printing repeatedly for several times. Subsequently, the printed GO film was properly cut and located in 90 $^{\circ}$C VDP chamber

containing hydrazine and ammonia solution for 30 min under vacuum. The graphene were immediately formed at low temperature. Then, the graphene electrodes of acoustic actuator were connected by Cu tape to the amplifier and sound source, which was used to reduce the electrode contact resistance. The transducers were excited to produce sound by a 50 root mean square voltage (V_{rms}) white noise signal. The range of frequency response was from 40 Hz to 20 kHz (audible frequency range) and measured at 1 m distance from the film along the centerline axis. As a commercial thin film speaker, poly(3,4-ethylenedioxythiophene):poly(styrenesulfonate) (PEDOT:PSS)-based acoustic actuator had the 85 % transmittance and 10 × 10 cm rectangular size. For active noise cancellation (ANC) application, a soft substrate (3M VHB 4910 acrylic form tape, Young's modulus = 105 kPa) was attached to graphene-based PVDF thin film in order to make an ANC actuator.

For the acoustic actuator characteristics, Brtiel and Kjaer 2012 audio analyzer was carried out (40 kHz to 20 kHz). Film transmittance was measured using a UV–visible spectrometer (Lamda-20; Perkin-Elmer, Waltham, MA, USA) at a resolution of 1 nm.

2.2. Size-Controlled Graphene Thin Films via Screen Printing and Their Applications

2.2.1. Graphene size control via mechanochemical method and their electro-responsive properties

The reagents including potassium permanganate ($KMnO_4$), sulfuric acid (H_2SO_4), hydrogen peroxide (H_2O_2), H_2SO_4 and ethanol were obtained from the Aldrich Chemical Co. Distilled water was used in all of the experiments. Silicone oil (Aldrich, poly(methylphenyl siloxane), viscosity = 100 cSt) was used as a dispersing medium for electro rheological (ER) fluid applications.

Graphite (5.0 g) was placed in a wet planetary ball mill capsule along with three sizes of balls (diameters: 1, 2, and 5 mm). The grinding bowls and balls were made from zirconium oxide. The capsule was then fixed in the planetary ball mill, and agitated at 550 rpm. The milled product was collected by sieving.

Size-controlled GO was synthesized from ball-milled graphite using a modified Hummers method. Typically, ball-milled graphite (1.0 g) was added to 70 mL of H_2SO_4 in an ice bath, followed by the addition of $KMnO_4$ (3.0 g) and sodium nitrate ($NaNO_3$) (0.5 g). After stirring for 4 h, 70 mL of distilled water was slowly added, and the suspension was kept in the ice bath for 30 min. Subsequently, H_2O_2 solution was added until the color turned a brilliant brown, which indicated complete oxidation. The ball-milled graphite oxide slurry was

exfoliated to generate size-controlled GO nanosheets by sonicating for 3 h in an ultrasonic cleaner (42 kHz, 100 W, Bransonic 3510, Branson Ultrasonics Corp., Danbury, CT, USA). Finally, the mixture was separated by centrifugation, washed repeatedly with 5% HCl and distilled water, and dried in a vacuum oven at 40°C for 24 h.

All of the dried size-controlled GO samples were dispersed in silicone oil for ER evaluation. ER properties were measured with a rheometer with a concentric conical cylinder geometry (cup radius: 15 mm), a temperature controller, and a high-voltage generator (Trek 677B). The gap distance was 1.00 mm. After loading a sample in the rheometer, direct current (DC) voltage was applied to the plate. The volume fraction of the ER material in the silicone oil was controlled at 0.5−3.0 vol%, and the shear rate was varied from 0.5−500 s^{-1}. All measurements were performed at room temperature. The yield stress value of prepared ER fluids is typically obtained from the flow curve of a controlled shear rate (CSR) mode experiment. The stress value of the transition point at which the shear viscosity abruptly decreased was taken as the dynamic yield stress.

Dynamic light scattering (DLS) measurements were carried out using a Photal dynamic laser scattering spectrometer DLS-7000 (Otsuka Electronics Co. Ltd., Tokyo, Japan) with an argon laser with 488 nm.

2.2.2. Highly conductive, flexible and scalable graphene hybrid thin films with controlled domain size as transparent electrodes

The concentration of GO solution (1 mg/mL) was obtained by mixing of the GO suspension with ethanol at a volume ratio of 150% ethanol to water. For the GO hybrid dispersion with controlled domain size, ball-milled GO and pristine GO (non-milling) powders were mechanically mixed, and they were dispersed in water/ethanol solvent (1 mg/mL concentration) by sonication.

For patterning of graphene sheets onto the poly(ethersulfone) (PES) film, oxygen plasma treatment was performed in order to modify the surface energies of PES substrate (gas flow rate: 20 sccm, power: 100 W, time: 20 s). The patterned architectures were designed by screen printing mesh. The size-controlled GO solution was printed on the flexible PES film by screen printing, and the printed film was properly cut, and located in vapor deposition chamber containing hydrazine solution (1mL, Sigma Aldrich). The chamber was sealed and placed in an oven at 90°C for 1 h. The color of the size-controlled GO thin film changed from brown to metallic gray by chemical reduction. Pressure-assisted reduction was carried out using hot press between stainless-steel plates at 180°C for 5 min. For the fabrication of graphene hybrid thin film, GO hybrid solution was printed on PES film, and identical reduction processes were conducted.

2.3. Multilayered Graphene Thin Films via Screen Printing and Their Application

2.3.1. High electrothermal performance of expanded graphite nanoplatelet-based patch heater

The natural flake graphite of 500 g was added into a mixed solution composed of sulfuric acid and potassium persulfate (KPS). The molar concentration of sulfuric acid was 15 M and that of oxidizing agent was changed from 0 to 300 mM. After being stirred at 80 oC for 8 h, the expansion of intercalated graphite was achieved by sonication for 3 h. The mixture was filtered by vacuum filtration using nylon membrane (0.2 μm, Whatman), and the black solid like cake form was washed with deionized water until the pH value of the solution was up to 7. Subsequently, the expanded-graphite nanoplatelets (EGnP) was dried at 60 ^{o}C for 24 h.

For line patterning of EGnP onto the polyimide (PI) film by screen printing, 30 wt% EGnP aqueous solution by sonication was prepared for a screen printing ink. Furthermore, oxygen plasma treatment was performed onto the PI film in order to modify the surface energies of target substrate (gas flow rate: 20 sccm, power: 100 W, time: 20 s). Since the attached mask on PI film formed open areas of mesh as a line patterning, EGnP ink could be transferred onto a substrate as a sharp-edged image by squeegee movement across the screen

mask. The EGnP-based line patterns of 100 mm length and 2.5 mm width were formed onto a PI film treated with oxygen plasma by screen printing repeatedly. Then, it was located within PI substrates to prevent the reduction of heat loss. The copper tape was used to lower the contact resistance between power source and EGnP-based line heater and maintain the controlled output voltage.

X-ray diffraction (XRD) patterns were collected using a MAC Science Co. M18XHF-SRA model and the power type of EGnP was prepared for sample preparation. For sample preparations of XPS and Raman analysis, EGnP aqueous solution was deposited on Si wafer using screen printing (Sunmechanix, SM-S550) and drop casting, respectively. In order to evaluate the EGnP-based line thickness, vernier callipers (Mitutoyo, IP 65) was used. The voltage was supplied by a DC power source (ODA, OPS-503) and the average line resistance was obtained by using a digital multimeter. The surface temperature distribution was characterized by an infrared thermal image (FLIR T200) and the water temperature was measured in real time by an infrared thermometer (Testo 925).

2.4. Graphene/Polyaniline Thin Films via Screen Printing and Their Applications

2.4.1. Graphene/polyaniline/poly(4-styrenesulfonate) hybrid film with uniform surface resistance and its flexible dipole tag-antenna application

Natural flake graphite (Sigma-Aldrich, < 20 μm, 10 g) was added to a mixed solution composed of sulfuric acid and potassium persulfate. After being stirred at 80°C for 6 h, exfoliation of the intercalated graphite was facilitated by exposure to microwave radiation for 5 min (700 W). The mixture was vacuum filtered through a nylon membrane (0.2 μm, Whatman). The resulting black, solid-like cake was washed with deionized water until the pH of the solution reached 7. The multilayer graphene was then dried at 70°C for 24 h.

PSS was synthesized by radical polymerization in an aqueous solution at 50°C. The 4-styrenesulfonate sodium salt (Sigma-Aldrich, 2 g) was introduced into distilled water (40 mL) and stirred vigorously for 2 h. The polymerization of styrenesulfonate was initiated with a,a′-azobisisobu-tyronitrile (0.06 g) for 6 h at 50°C, resulting in an aqueous PSS solution. The PANI/PSS mixture was fabricated by the addition of an aqueous PSS solution into an aqueous, well-dispersed PANI solution. PANI nanoparticles were synthesized by introducing aniline monomer (1.06 mmol) dropwise in a 0.5-M aqueous HCl solution (50

mL) and stirring for 1 h. The polymerization of aniline was conducted using APS (1.38 mmol) as an oxidizing agent for 10 h at 30 °C. After mixing, a dark green (the typical color of emeraldine salt) PANI–PSS nanoparticle solution was obtained.

Graphene (G)/PANI/PSS-based conducting paste was obtained by mechanically blending the synthesized multilayer graphene with the aqueous PANI/PSS solution. Terpineol and butyl cellosolve with content ratio were used as organic solvents for the preparation of the graphene-based conducting paste, and it could be easily prepared by grinding graphene with solvents in an agate mortar.

A circumscribed circle of G/PANI/PSS-based film (5.5 mm inner diameter, 7 mm outer diameter) was screen-printed onto photo paper. The ring-patterned, hybrid film-based, dipole tag antenna was placed at a fixed distance from a reader antenna in an anechoic chamber, oriented in the direction of maximum gain. For the synthesis of pristine graphene-based thin film, 30 wt% of graphene paste was used as a conducting ink for screen printing.

Fourier transform infrared (FTIR) spectrometer (Bomem MB 100, USA) were also used.

2.4.2. Fabrication of highly scalable graphene/polyaniline thin film with enhanced electrical and mechanical property and its monopole antenna application.

The GO powder was dissolved in deionized water (3 mg/ml) and hydrazine monohydrate was added to the solution (the volume ratio of hydrazine mono hydrate : water = 1 : 1000). And this solution was heated at 80 °C for 12hr. After reduction process, the graphene solution was filtered by filter paper with excess deionized water and was dried in vacuum oven, as in powder form, for further use.

The as-prepared graphene powder was added to HCl solution (2.5 M, 40 ml) in Erlenmeyer flask. The solution was sonicated for 24 hr and aniline monomer was added, keeping vigorous stirring. After that, chloroform (60 ml) was added to the mixture, leading to the phase separation (chloroform phase at the bottom, aqueous phase on the top). Then the initiator, APS (the weight ratio of APS : aniline = 1.2:1) in HCl solution (3.75 M, 16 ml), was added to the above bi-phase solution and stirred for 24 hr at - 40 ^{o}C, resulting in the low-temperature interfacial polymerization. After polymerization process, the solution was centrifuged and dried. The feeding weight ratio of aniline to graphene was 12:1. Primary doped G/PANI powder was dispersed in ammonia solution (1.2 M, 215 ml) and vigorously stirred for 24 hr to de-dope the PANI

chains on the graphene, resulting in the De-G/PANI. This solution was centrifuged again and dried to collect powder. The real weight percentages of the PANI component in the De-G/PANI were calculated as 76 %. The De-G/PANI powder was mixed with the CSA (the mole ratio of PANI : CSA = 2:1) to re-dope the PANI chains on graphene, resulting in the Re-G/PANI. The Re-G/PANI powder was added to the m-cresol/chloroform solution (the volume ratio of m-cresol : chloroform = 7:3) to be as 2.38 wt % of total mass of solution and stirred for 3 hr and sonicated for 24 hr. The Re-G/PANI solution was drop-casted onto glass substrate and was annealed at $40\,^{\circ}C$ for 16 hr. Finally, the free standing G/PANI film was obtained by detaching the annealed film from the glass substrate in the water. The synthetic procedures of the PANI (ES state), De-PANI (EB state), and Re-PANI film were identical to those of the primary doped G/PANI, De-G/PANI, and Re-G/PANI film except incorporation of the RGO.

Solvated G/PANI could be used as conducting ink in screen printing, and the smaller sized thin films (3 cm x 500 μm) of graphene, PANI and G/PANI-based thin films were screen-printed onto photo paper. The permittivity was measured using a Solatron SI 1260 impedance/gain-phase analyzer with a Solatron 1296 dielectric interface. Three types of film-based, monopole tag antenna was connected to an RF network analyzer for monopole antenna tests.

3. RESULTS AND DISCUSSION

3.1. Chemically Exfoliated Graphene Thin Films via Inkjet Printing and Their Applications

3.1.1. Micropatterning of graphene sheets by inkjet printing and its wideband dipole-antenna application

The overall procedure for line patterning of graphene sheets by inkjet printing is illustrated in Figure 13. In general, ideal ink for inkjet printing is required to have viscosity between 1 and 20 mPa s and to match surface tension of the ink with surface energy of the substrate [100,101]. In this experimental condition, exfoliated GO aqueous solution had excellent dispersibility due to its hydrophilic property [102,103]. The viscosity value of GO aqueous sloution was measured to be *ca.* 2.2 mpa s that was applicable to be used as an ink for inkjet printing without any other additives. In addition, in order to match between surface energy of a substrate and surface tension of GO ink (72.8 mN m^{-1}), PET film was treated with oxygen plasma that caused the surface energy of the substrate to increase from 41.0 to 68.7 mN m^{-1}. The GO-based ink meeting the above conditions could be printed out precisely onto the substrate via loading GO solution into modified ink cartridge (Figure 13a). Inherently, GO is electrically insulating because of its structural defects and oxidized GO domains [104,105]. Therefore, an additional reduction step is
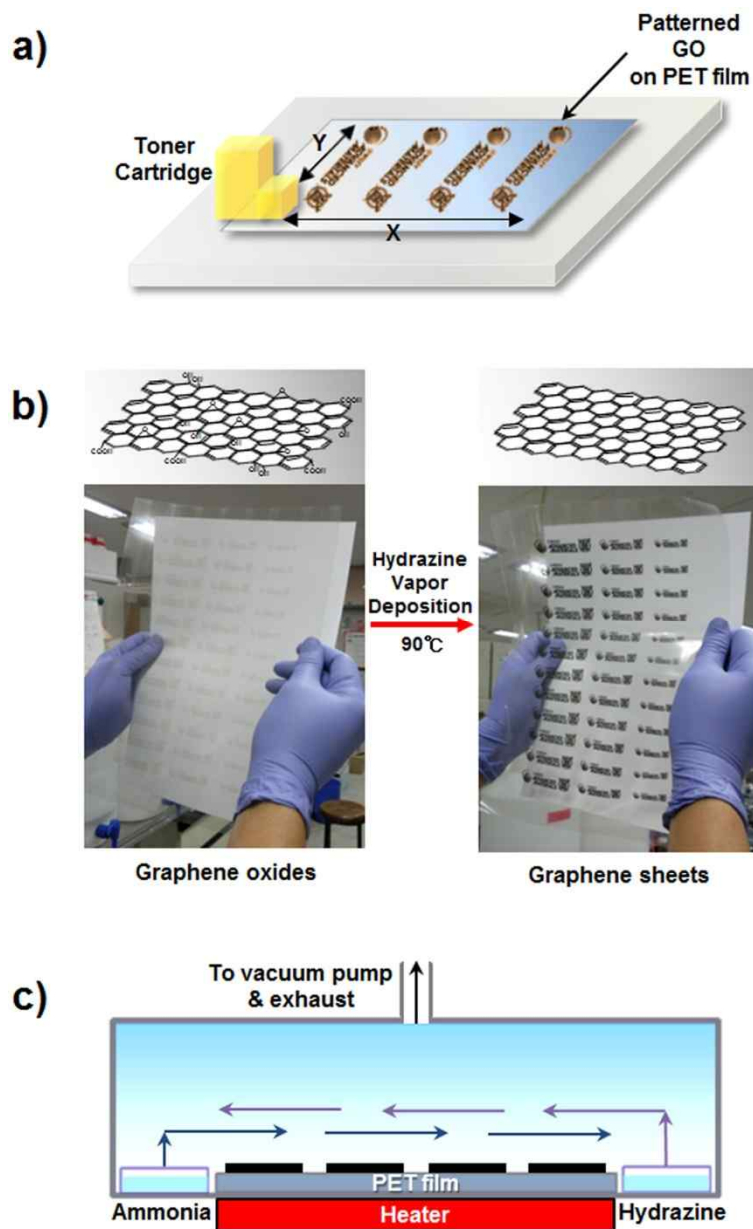
Figure 13. a) The fabrication of patterned GO on PET film by inkjet printing. b) Large-area patterned GO (left image) and graphene sheets resulted from the reduction procedure (right image). c) The reduction process was performed by mild-thermal annealing at 90 °C with hydrazine and ammonia vapor.

needed to make it electrically active. In this study, this reduction process was performed using the hydrazine VDP and mild thermal annealing (Figure 13c) [106,107]. As a result, patterned GO and graphene sheets could be efficiently synthesized in large area (Figure 13b).

The AFM topography image (Figure 14a) displays that the exfoliated GO is composed of a few micron-sized monolayer (< 1.5 nm), bilayer (2−3 nm) and multilayer (> 3 nm). In addition, TEM image also reveals that the GO ink consist of exfoliated graphene sheets, dispersing in a stable aqueous solution (Figure 14b). To confirm the successful reduction from GO to graphene, XPS and Raman spectrum analysis were conducted. The deconvoluted C1s XPS spectrums of patterned GO by inkjet printing for 30 passes and graphene sheets by reduction procedure are presented in Figure 15a. Generally, the C1s signal of GO mainly consists of three components, which are C=C/C−C in aromatic rings (285.0 eV), C−O (286.5 eV) and C=O (288.5 eV) peaks [108]. While the C−O component comes from epoxy and hydroxyl groups, the C=O bond originates from carboxy and carbonyl groups. The result was that ratio of the $I_{C−O}/I_{C−C}$ decreased from 1.1440 (GO) to 0.2432 (graphene sheets). The Raman spectrum of patterned graphene sheets on the PET film is exhibited in Figure 15b. It is well-known that the G peak (around at 1,586 cm^{-1}) indicates graphite carbon structure, whereas the D peak (around at 1,355 cm^{-1}) means typical
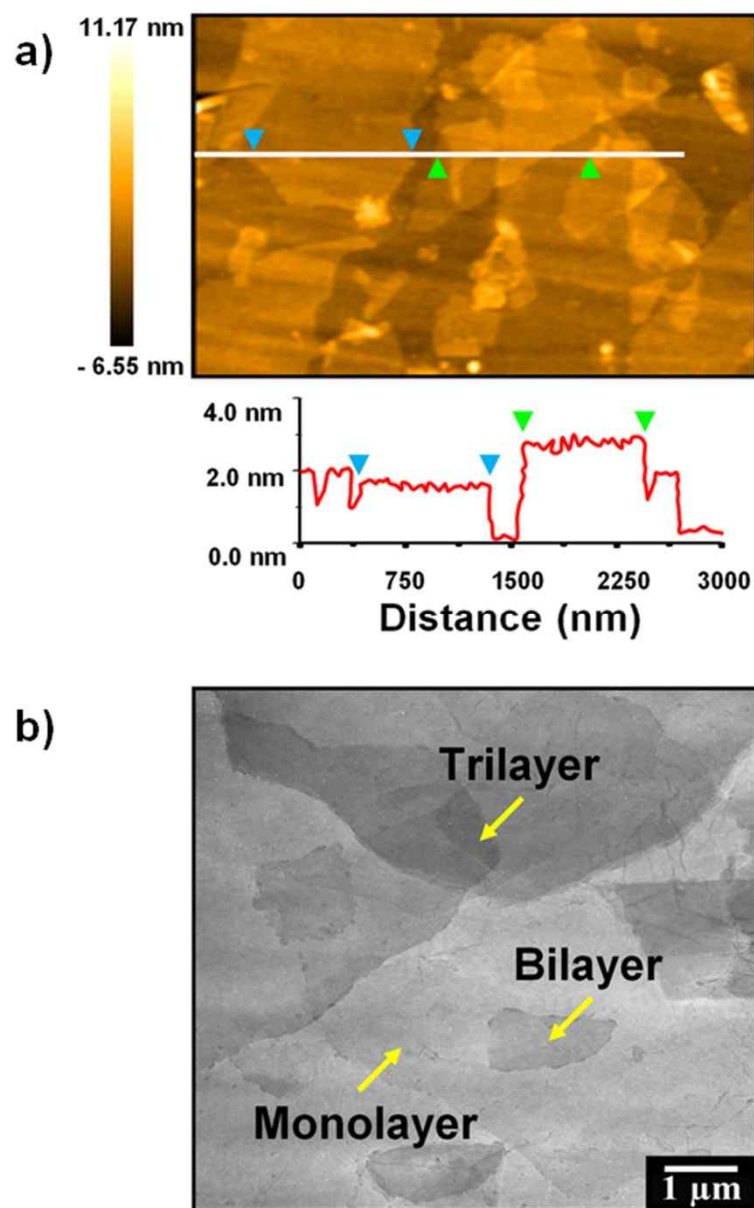
Figure 14. a) Representative AFM and b) TEM image of the exfoliated GO as a conducting ink for inkjet printing. For the sample preparation, the exfoliated GO solution was deposited on Si wafer and copper grid, respectively.
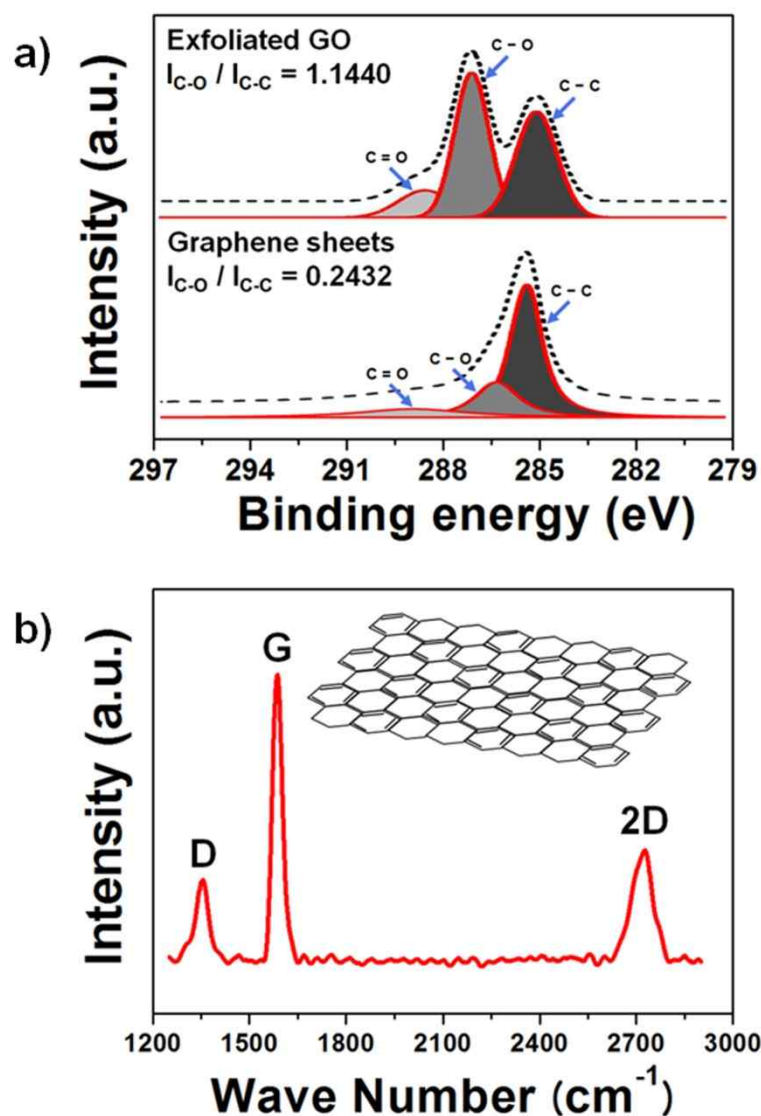
Figure 15. a) Deconvoluted XPS spectrum of patterned GO films by repeat inkjet printing for 30 passes (top image) and graphene sheets resulted from the reduction procedure (bottom image) in the C1s region. Fit lines are labeled as: C−C, C−O and C=O bonds. b) Raman spectra of patterned graphene sheets on the PET film showing G and 2D peaks. A weak D peak is apparent, consistent with edge effects.

defects ascribed to the structural edge effects, such as epoxides covalently bonded to the basal plane [109]. The intensity ratio of I_D/I_G for patterned graphene sheets was *ca.* 0.28 at a mild-temperature, which demonstrated a higher degree of graphitization than that of reduction process at high temperatures (> 400 $^{\circ}$C) [110,111]. The 2D peak position (around at 2,726 cm^{-1}) of graphene sheets was also clearly observed. Geim et al. showed that electronic structure of graphene was uniquely captured in its Raman spectrum that clearly evolved with the number of layers [112,113]. Raman fingerprints for single-, bi-, and few-layer graphene reflect changes in the electronic structure and allow unambiguous, high-throughput and nondestructive identification of graphene layers. Therefore, it is possible to identify the number of graphene layers from the shape of the 2D peak. From this point of view, it could be implied that the patterned graphene based thin film consisted of the multi-layer graphene sheets.

In order to measure the thickness of the graphene-based thin film, AFM analysis was also performed to the film acquired by inkjet printing for 1 pass and VDP process. Figure 16a shows that the film thickness was estimated to be *ca.* 10 nm. As a result of up to a printing number of 30, it was noticed that the film thickness was linearly increased with increased printing number, and the average layer thickness was considered to be *ca.* 10−15 nm (Figure 16b).
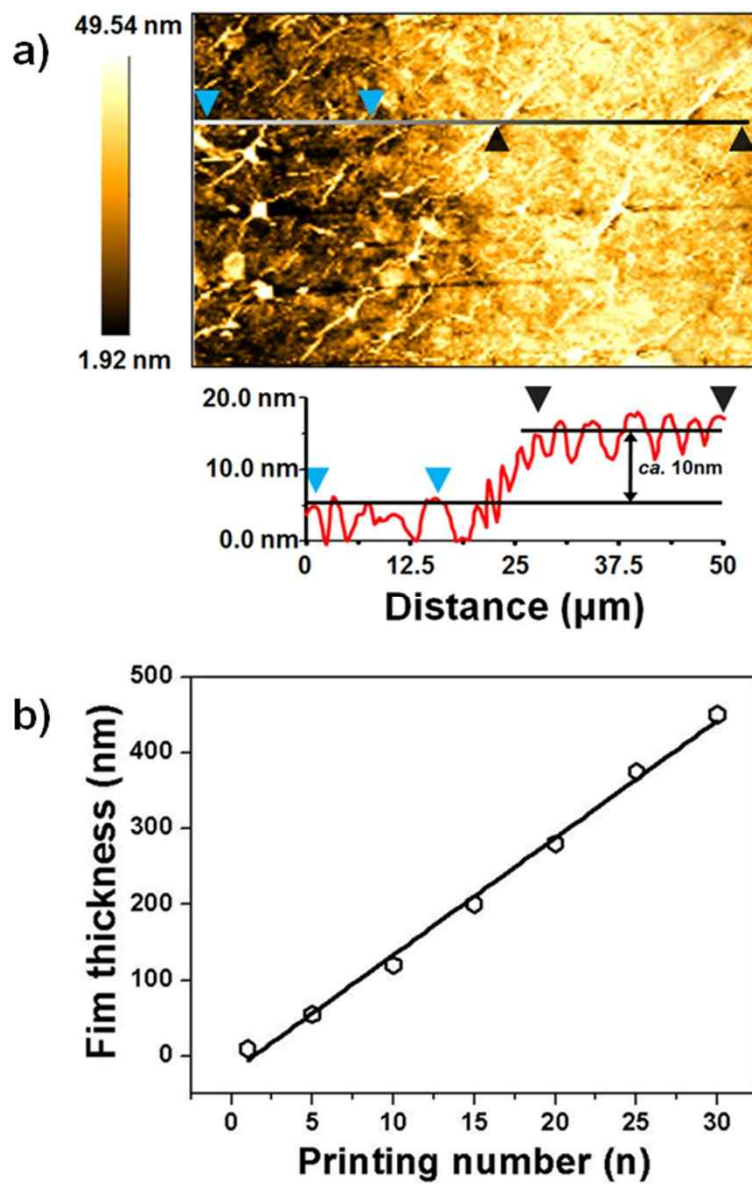
Figure 16. a) AFM image of patterned graphene sheets with 70 μm line width obtained by inkjet printing for 1 pass and reduction process (observable range of AFM : 50 μm) b) The film thickness of patterned graphene sheets as a function of printing number. The average layer thickness considered to be *ca.* 10−15 nm.

Judging from these results, it was evident that graphene-based thin film consisted of a few layers of graphene, and the GO was successfully reduced to graphene sheets by the hydrazine vapor as a reducing agent.

The graphene sheet patterns prepared by inkjet printing was compared with the other conducting polymers such as polypyrrole (PPy) and polyaniline (PANI) onto PET film via the same inkjet printing and VDP method [114,115]. In general, conducting polymers are insoluble into common solvents because the delocalized electrons of conducting polymer hinder solubilization in polar solvents. For this reason, PPy and PANI patterns were fabricated via chemical oxidative polymerization of vaporized monomer on inkjet-printed oxidant patterns in the VDP chamber. Figure 17 demonstrates that well-defined patterns with various shapes and line widths of patterned graphene sheets were more clearly observed than those of the other conducting polymers on the PET film. For the definite comparison of line resolution, the patterned lines with *ca.* 70 μm were fabricated, which was the minimum line width (Figure 18). It also showed that the resolution of patterned graphene line was much higher than those of the others. The difference of resolution could be attributed to rapid polymerization process, matching surface energy between substrate and ink and grain property on domain structure. In other words, as evaporated monomers were promptly deposited and polymerized on the patterned oxidant
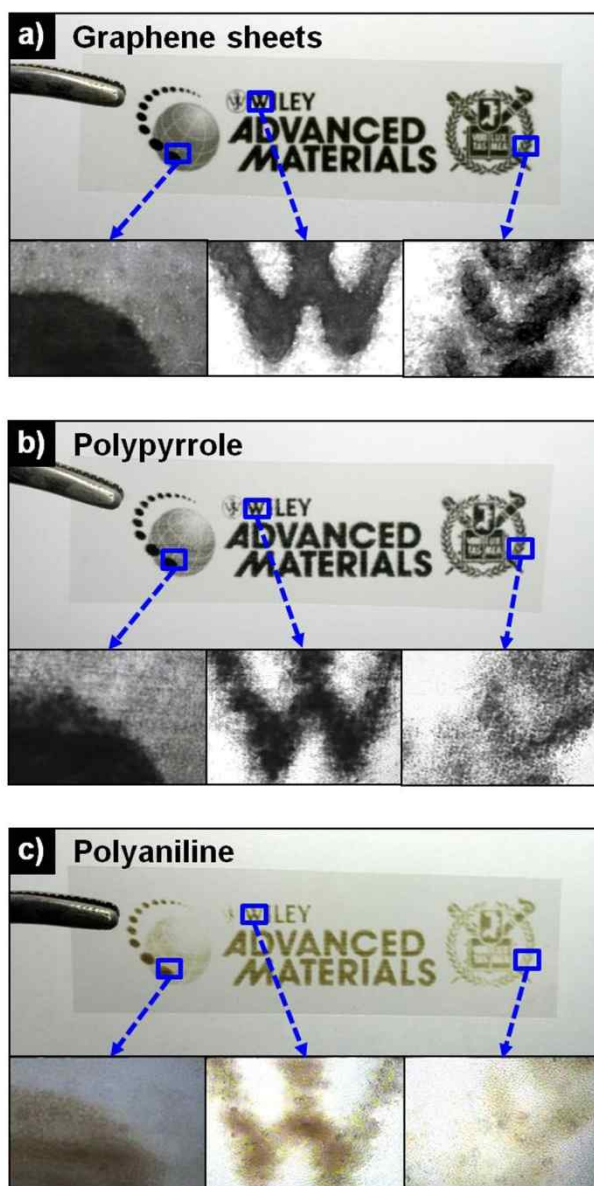
Figure 17. The various optical images of a) graphene sheets, b) PPy and c) PANI patterns prepared by inkjet printing and VDP method. The optic images were magnified at marked areas. The PET film was treated with oxygen plasma at low temperature to increase surface energy of the substrate (gas flow rate: 20 sccm, power: 100 W, time: 20 s, and inkjet printer resolution: 4800 x 1200 dpi)

66
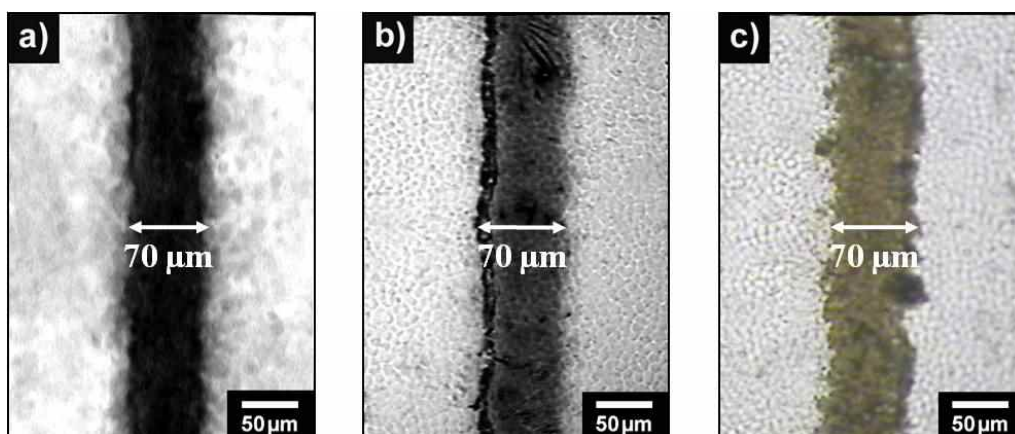
Figure 18. The optical micrographs of patterned straight lines of a) graphene sheets, b) PPy and c) PANI with the width of *ca.* 70 μm. In all images, the scale bar is 50 μm.

APS film, polymer nanoparticles on surface were aggregated, leading to cracked and wrinkled form. Furthermore, high difference of surface tension between APS ink and oxygen-treated PET film caused matching problem of surface energy, resulting in forming line-edge waveness, and Figure 19 shows stacks of planar structure of patterned graphene sheets on the large domain. For these reasons, high resolution of patterned graphene could be obtained.

In addition, the patterned graphene sheets with various line widths were successfully fabricated (Figure 20a, b and c). To clarify how well-defined patterns was formed without ink spread, dotted line having a gap of 70 μm between dots was printed and then current was measured by 2-probes of the multimeter connecting to the both ends of the dotted line. The current of the dotted line was zero unlike that of the full lines, which indicated that each dot of the dotted line was electrically distinct from each other, and the patterned graphene sheets were synthesized properly without ink spread (Figure 20d).

Moreover, the successful designed gradient pattern reveals that the electrical conductivity can be readily regulated in the same line, and suggests the possibility to fabricate various types of electrodes (Figure 21). The changes in concentration of GO ink and the number of printing were also capable of tuning the sheet resistance finely. The surface resistance of patterned graphene sheets is plotted as functions of GO concentration and printing number (Figure
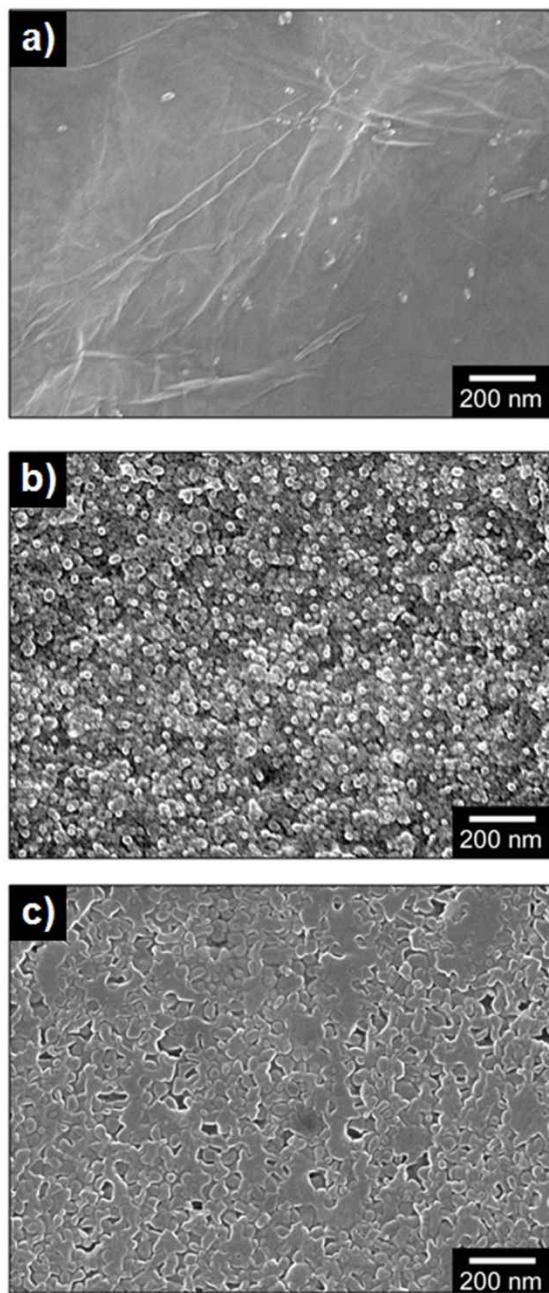
Figure 19. FE-SEM images of the surface morphology for patterned a) graphene sheets, b) PPy and c) PANI on PET substrate.
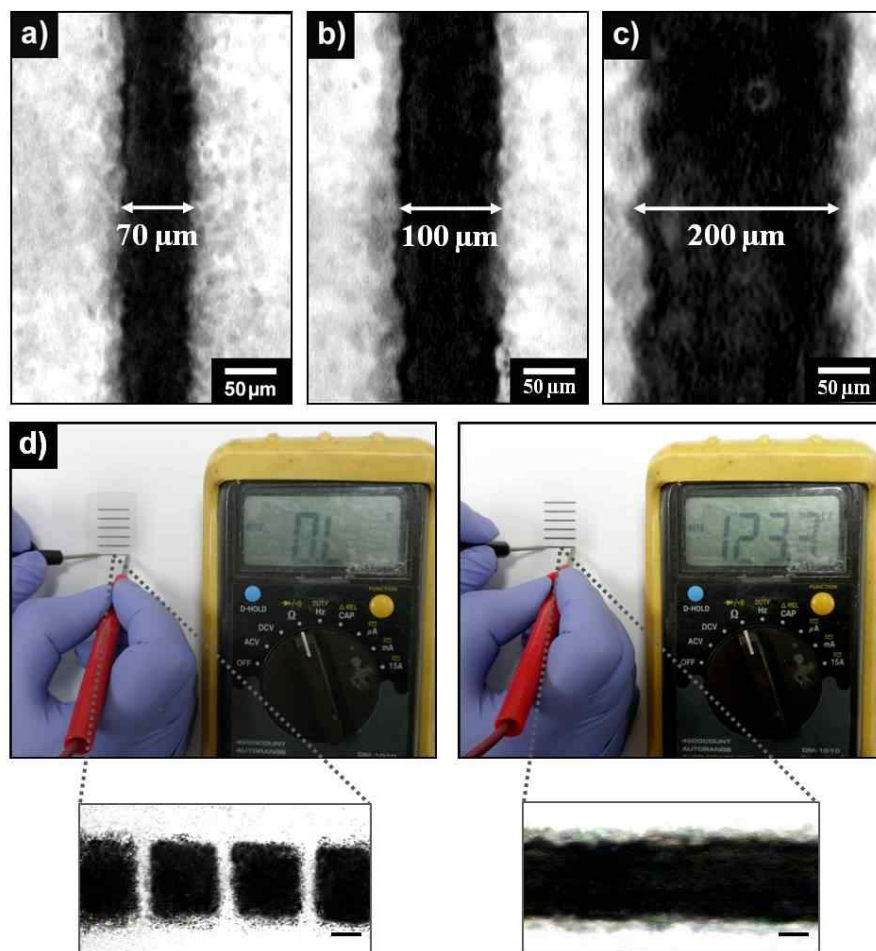
Figure 20. The optical micrographs of patterned graphene-based thin film with the width of *ca.* a) 70, b) 100 and c) 200 μm. In all cases, the scale bar is 50 μm. d) The electrical measurement of the full line and consecutive repeated pattern having a gap of 70 μm between dots in the dotted line. The pattern was magnified by optical microscopy (scale bar: 125 μm).
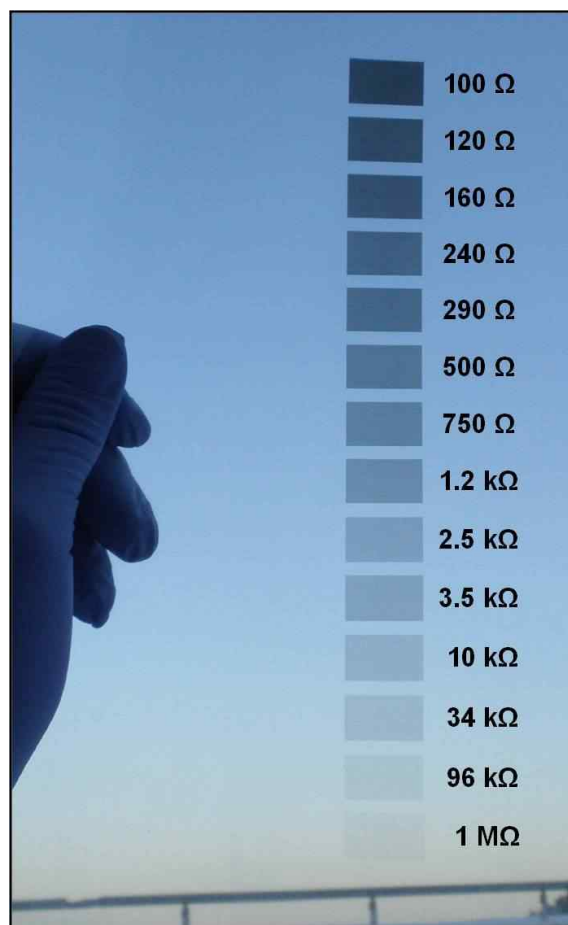
Figure 21. The photo image of gradient patterned graphene sheets with controlled surface resistance as a function of lightness. Grayscale images were designed by computer software in advance (Microsoft PowerPoint 2003).

22a). To evaluate the electrical characteristics, the surface resistance of patterned graphene sheets was measured by four-probe method. When the printing number and GO concentration increased, the resistances of patterned graphene sheets decreased gradually. After the minimum surface resistance of patterned graphene sheets was obtained by repeat inkjet printing for 30 passes with 0.7 % GO ink, the value was estimated to be *ca.* 65 Ω sq^{-1}. From the data, it can be inferred that the surface resistance of the patterned graphene-based thin films exhibits 3-fold reduction compared with that of surfactant-mediated graphene film owing to the insulating property of the additive [116,117].

On the basis of the above analysis, we have demonstrated for the first time that the graphene-based thin film was able to be applied for electrode of wideband RFID antenna. It is wireless communications technology which can transfer large amounts of information over a very wide-band with relative low-power compared to the existing spectrum. The practical dipole antenna composed of two wires was chosen for this implementation [118,119]. Since the bandwidth is determined by the length of the dipole antenna, the length should be *ca.* 30 cm to fabricate the 500 MHz dipole antenna.

Two key parameters such as bandwidth and voltage standing wave ratio (VSWR) or return loss (RL) of the antenna have to be considered to evaluate the performance of the designed antenna [120,121]. The bandwidth is basically
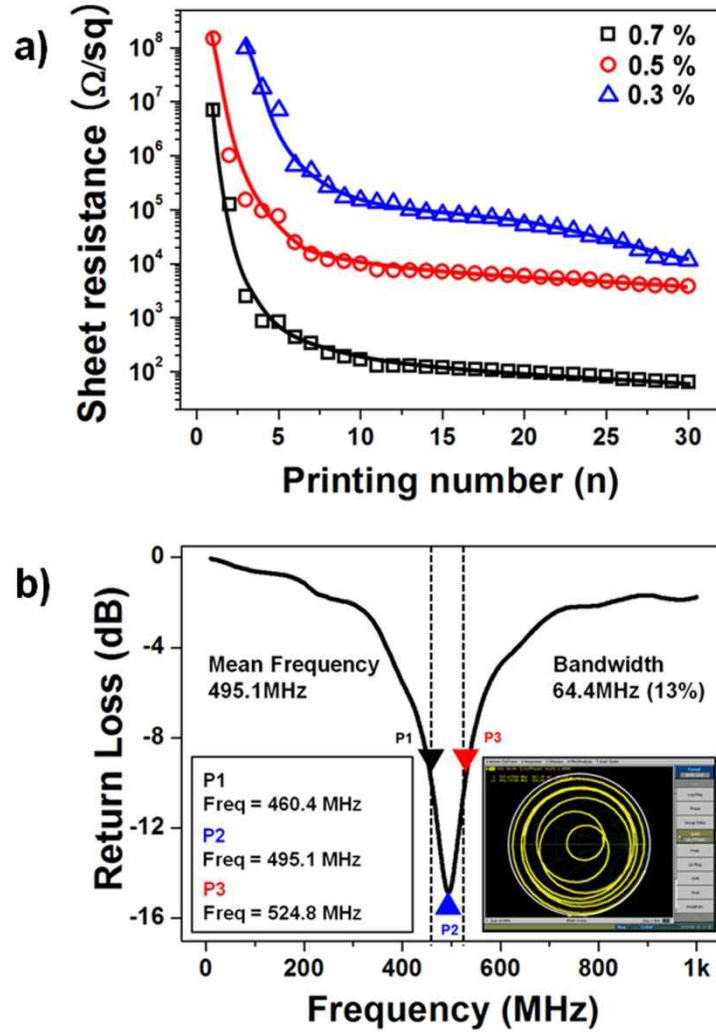
Figure 22. a) Surface resistance of patterned graphene sheets as functions of the GO concentration and printing number. The surface resistance was measured by four-probe method. b) The return loss curve of the dipole antenna application using patterned graphene sheets electrode. (inset: Smith chart impedance diagram of designed dipole antenna).

frequency that the antenna is required to radiate, and the VSWR represents that how efficiently frequency power is transmitted from a power source. A large positive return loss indicates that the reflected power is smaller than the incident power, and implies good impedance matching between source and load.

Figure 22b shows the return loss curve of the dipole antenna using patterned graphene sheets electrode. The bandwidth of simulated RL was ranged from 460.4 MHz to 524.8 MHz with respect to 10 dB standard. Furthermore, the VSWR and RL at the center frequency are displayed in Table 1 and high transmitted power efficiency of 96.7 % is obtained using patterned graphene sheets electrode. The inset photograph indicates a typical Smith chart impedance diagram of the dipole antenna. The chart, the graphical representation of the mathematical properties of a network, is widely used to represent port impedances and VSWR. From the data, the impedance point of passband was located near the center of Smith chart. It meant that the smaller return loss was, the closer impedance point located to the center [122]

Table 1. VSWR and RL of patterned graphene sheets-based dipole antenna.

VSWR	RL[a]	Reflection Coefficeint (Γ)	Transmitted Power	Reflected Power
1.44	14.9	0.144	96.7	3.3

[a] This value was acquired in the E5071B ENA RF Network Analyzer of Agilent Technologies.

3.1.2. Flexible and transparent graphene films as acoustic actuator electrodes using inkjet printing

The structure and functional principle of graphene-based PVDF thin film speaker using converse piezoelectric effect was illustrated in Figure 23a. When a time variable voltage (AC electric field) was applied to graphene electrodes on the piezoelectric PVDF film, it could produce the sound wave as attractive and repulsive forces between internal charge and external field were continued to repeat. Figure 23b shows the photograph of the acoustic actuator that consists of graphene-based transducer connected to the sound source and amplifier.

For fabrication of the graphene film onto the PVDF substrate, exfoliated GO aqueous solution was used as conductive ink, and the thermal annealing for reduction process was performed under vacuum conditions (*ca.* 10^{-3} torr) (Figure 24). The hydrophilic property of GO solution could make it possible to overcome the limitations on conductive ink preparation to be printed through a nozzle including optimization of suitable solubility, viscosity and surface tension [123,124]. Furthermore, in order to prevent the deformation of the film and match between surface energy of substrate and surface tension of GO ink (75.2 mN m^{-1}), PVDF film was modified with low-temperature oxygen plasma. As a result, the surface energy of the film increased from 25.0 to 58.7 mN m^{-1}, indicating that the GO ink could be printed out precisely onto the substrate.

Figure 23. a) Schematic illustration and b) photograph of PVDF-based thin film acoustic actuator using flexible and transparent graphene electrodes. The P and F meant polarization and force of the acoustic actuator, respectively.
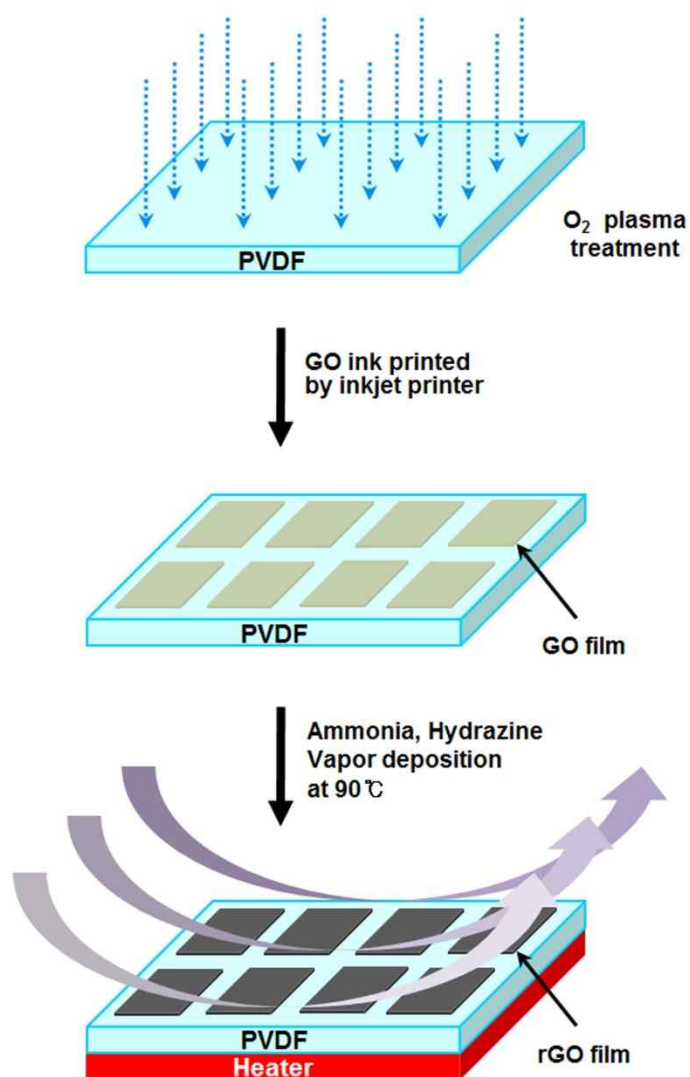
Figure 24. The fabrication of graphene electrodes on PVDF film by inkjet printing and VDP. The reduction process was performed by mild-thermal annealing at 90°C with hydrazine and ammonia vapor. The PVDF film was treated with oxygen plasma at low temperature (5°C) to increase surface energy of the substrate (gas flow rate: 20 sccm, power: 100 W, time: 120 s and print resolution: 4800 x 1200 dpi).

To confirm the successful reduction from printed GO to graphene film onto the PVDF substrate, XPS analysis for different films were conducted (Figure 25). For pristine PVDF film, main peaks of the CF_2, CH_2 and C–C bonding appeared at 290.8, 286.2 and 284.5 eV [125]. After the low-temperature O_2 plasma treatment on the PVDF film, the intensity of the CF_2 peak decreased. On the contrary, the C–O component (286.3 eV) from epoxy and hydroxyl groups and the C=O bond (288.5 eV) from carboxy and carbonyl groups had emerged. It could be originated from the defluorination and oxidation of carbon radical occurred on the PVDF surface [126]. When the GO ink was printed out by repeat printing for 10 passes, it was apparent that the CF_2 peak of pristine PVDF film disappeared. It meant that the PVDF substrate had negligible effect on XPS intensity of GO film. Furthermore, as a result of reduction process for graphene film, the ratio of the I_{C-O}/I_{C-C} decreased from 1.19 (GO) to 0.29 (graphene). The Raman spectrum of GO and graphene film on the PVDF substrate indicated of an increased I_D/I_G intensity ratio via reduction process (Figure 26). This change suggested a decrease in the average size of the sp^2 domains upon reduction of the exfoliated GO. Judging from these data, it was evident that the printed GO was successfully reduced to graphene film without defect by the hydrazine vapor as a reducing agent.

In order to measure the thickness of graphene thin film, AFM analysis was also
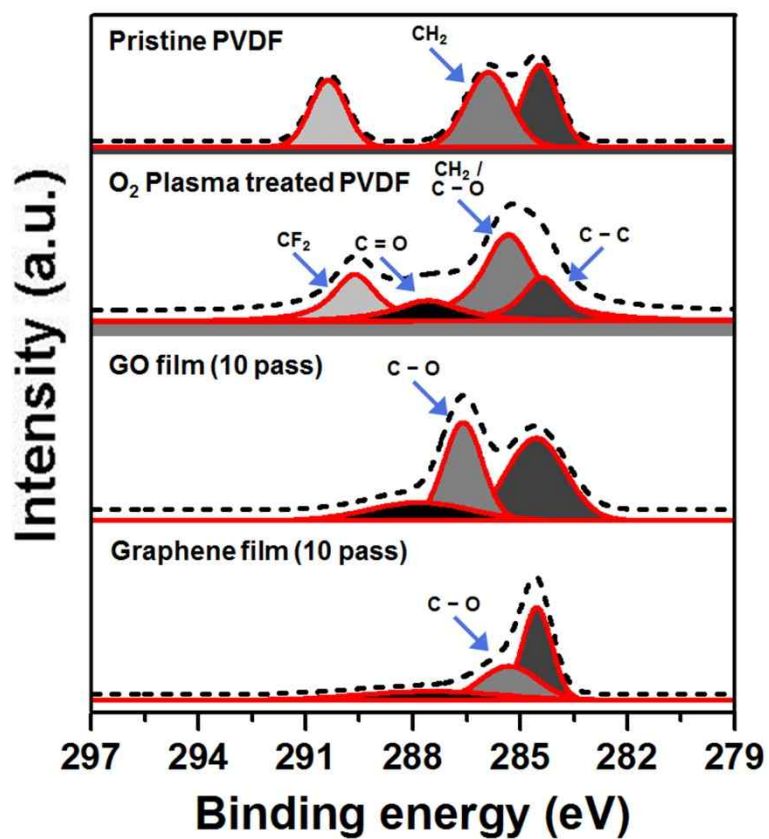
Figure 25. Comparison of deconvoluted XPS spectrum of pristine PVDF, O_2 plasma treated PVDF films, exfoliated GO by inkjet printing for 10 passes and graphene thin films resulted from the reduction procedure onto the PVDF substrate in the C1s region.
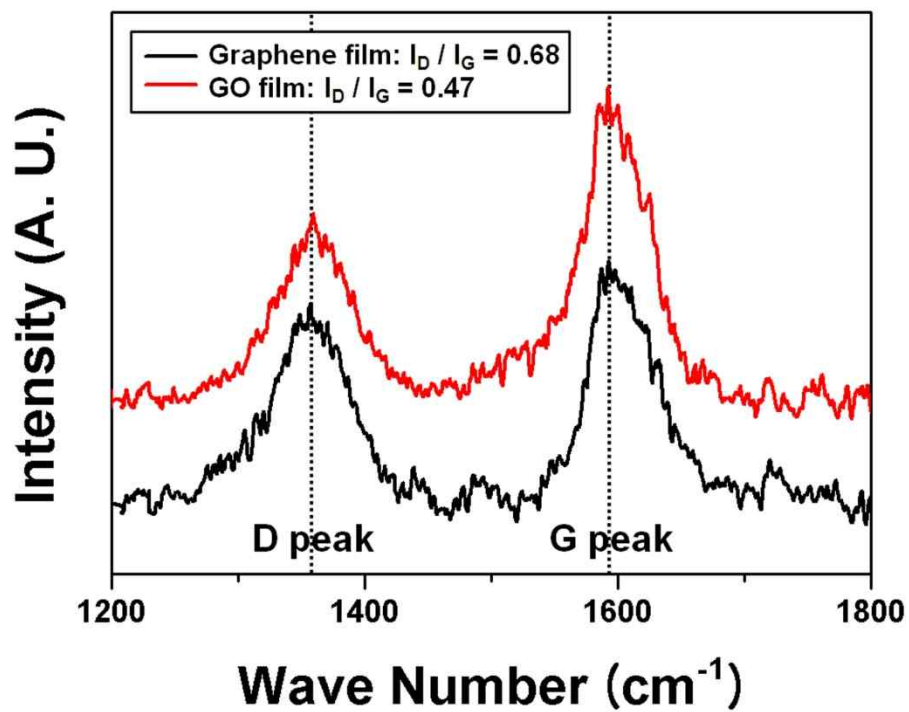
Figure 26. The Raman spectra of GO and graphene film on the PVDF substrate showing G and D peaks.

carried out. Figure 27a presents that the film thickness increased linearly with increasing printing number, and the average of layer thickness was considered to be *ca.* 15−20 nm. The inserted image was AFM topography of graphene film by inkjet printing for 1 pass which had the observable range of 50 μm. Considering this result, it was proved that graphene thin film consisted of multilayers of graphene. Moreover, the fine tuning of the surface sheet resistance and transmittance was accomplished via controlling the number of printing. As shown in Figure 27b, the obtained multilayer graphene films on the PVDF substrate had sheet resistances of 700, 10, 2 and 1.5 kΩ sq^{-1} at room temperature and transparencies (defined as transmittance at a wavelength of 550 nm and presented in the inserted graph) of 92.65, 81.85, 72.35 and 66.94 %, respectively. This result implied that the conductivity of graphene film synthesized by reduction process under vacuum was 7 times higher than that without vacuum, though the graphene film on the both sides of PVDF substrate had lower transmittance than that printed on one side of the substrate.

Figure 28a depicts the acoustic response of graphene-based thin film speaker with different electrode thickness (60, 90 and 120 nm) compared to that of PEDOT:PSS-based commercial thin film. In general, the wavelength of substrate is inversely proportional to frequency, while the film thickness is directly proportional to wavelength [127]. Furthermore, an increase of the film
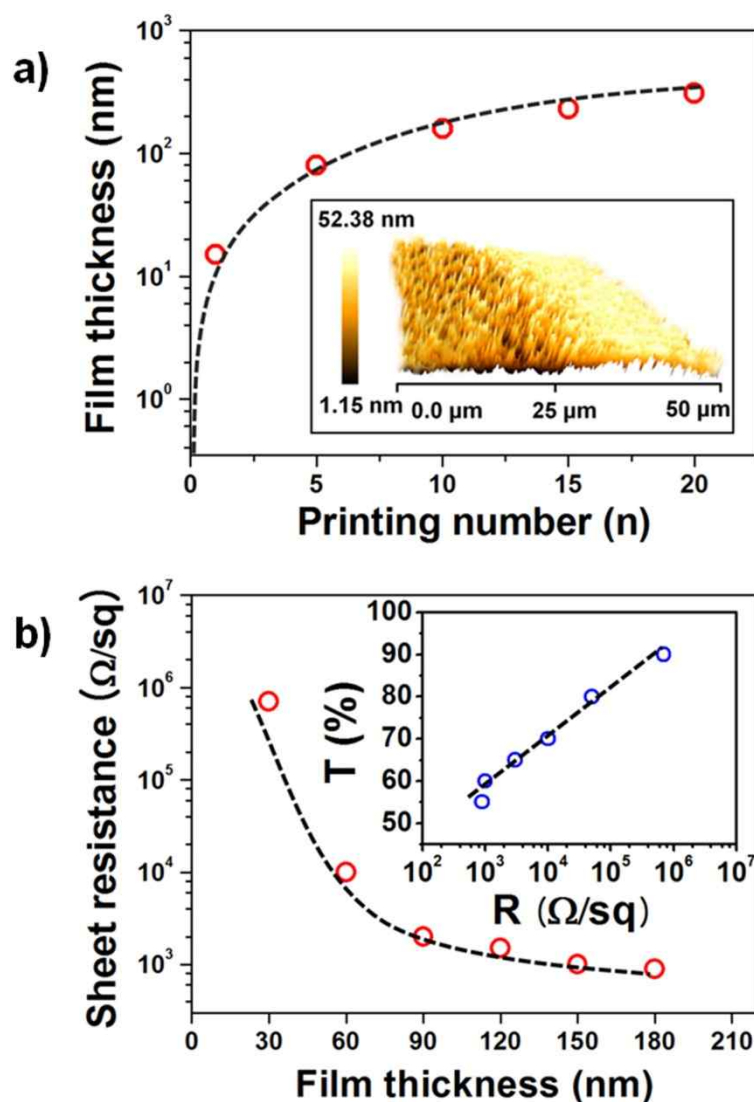
Figure 27. a) The film thickness of graphene electrodes as a function of the printing number using inkjet printing and reduction process (Inset: AFM image of graphene film acquired by inkjet printing for 1 pass which has observable range of 50 μm) b) The surface sheet resistances of graphene-based PVDF films with different film thickness (Inset: the data represented by transmittance versus sheet resistance with the same film thickness).
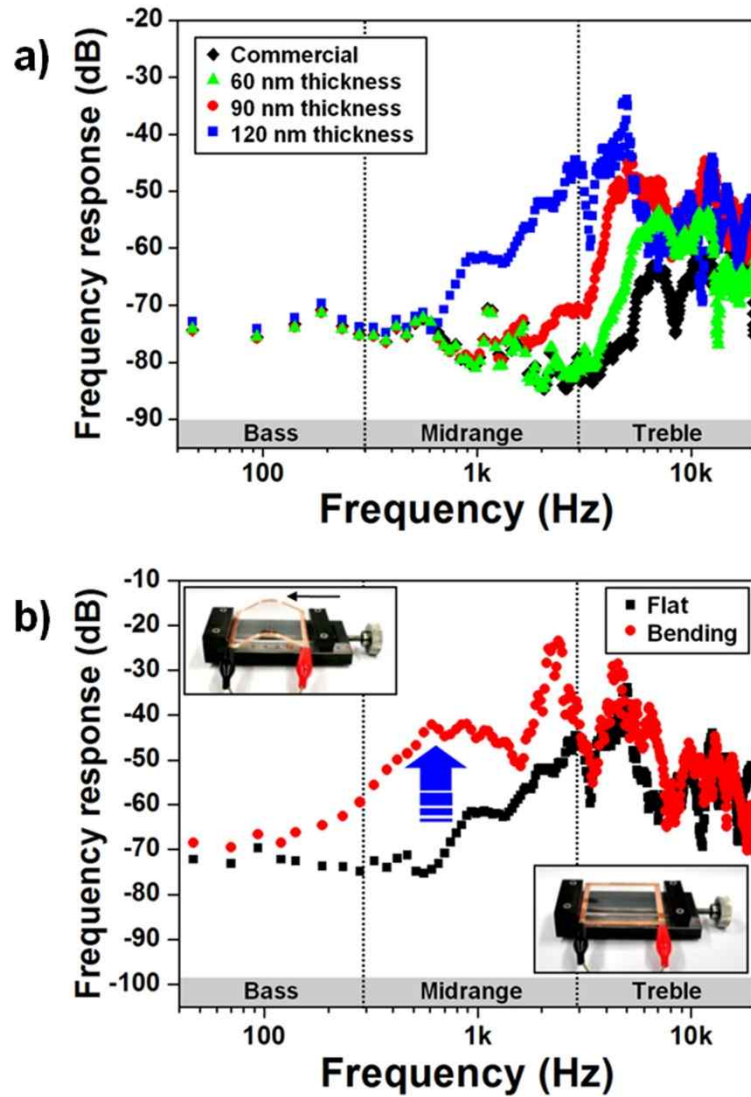
Figure 28. a) The frequency response of the graphene-based thin film transducer with three different electrode thickness (60, 90 and 120 nm) compared to the PEDOT:PSS-based commercial thin film transducer b) Each frequency response at the flat and bending conditions (radius: 6 cm) of graphene-based thin film transducer with 120 nm electrode thickness.

thickness could lead to lower surface sheet resistance. For these reasons, the overall frequency responses were enhanced with increasing the film thickness, particularly over the midrange frequency. In addition, the acoustic actuators with graphene electrode had higher responses over all frequencies than those with PEDOT:PSS electrode. In particular, the graphene-based PVDF film with 60 nm thickness had the 10 dB higher response in the treble frequency range than the commercial thin film, which meant that the sound level of the graphene-based transducer could produce at least 3.1 times higher than that of the commercial transducer at the same driving voltage. Moreover, each frequency response at the flat and bending conditions (radius: 6 cm) of the graphene-based transducer with 120 nm thickness was estimated in Figure 28b. It also showed that the frequency response was obviously enhanced in the bass and midrange frequency at the bending condition compared to the flat condition. This result was based on the principle that waves of sound energy could be focused at the bending condition. From the point of view, the graphene-based acoustic actuator was expected to remove the need for expensive high-power voltage amplifiers due to much less power consumption, and be used as a transparent, extremely thin and lightweight loudspeaker.

It was also found that the performance of the graphene-based acoustic actuator could be optimized for ANC application which was achieved by

introducing a cancelling anti-noise wave of both equal amplitude and opposite phase using a soft substrate [128,129]. The important effect of the soft substrate was that could help to eliminate the nonlinear harmonics of the graphene-based acoustic   actuator. As a result of the 3 kHz tonal signal input, the graphene-based transducer without soft substrate generated harmonic sounds at multiples of 3 kHz (Figure 29). However, the spectrum of graphene-based transducer with soft substrate had attenuated harmonics of 6−21 kHz due to the added damping and amplified 3 kHz frequency response which was considered as desired tonal signal. This finding provides new possibility for ANC application.
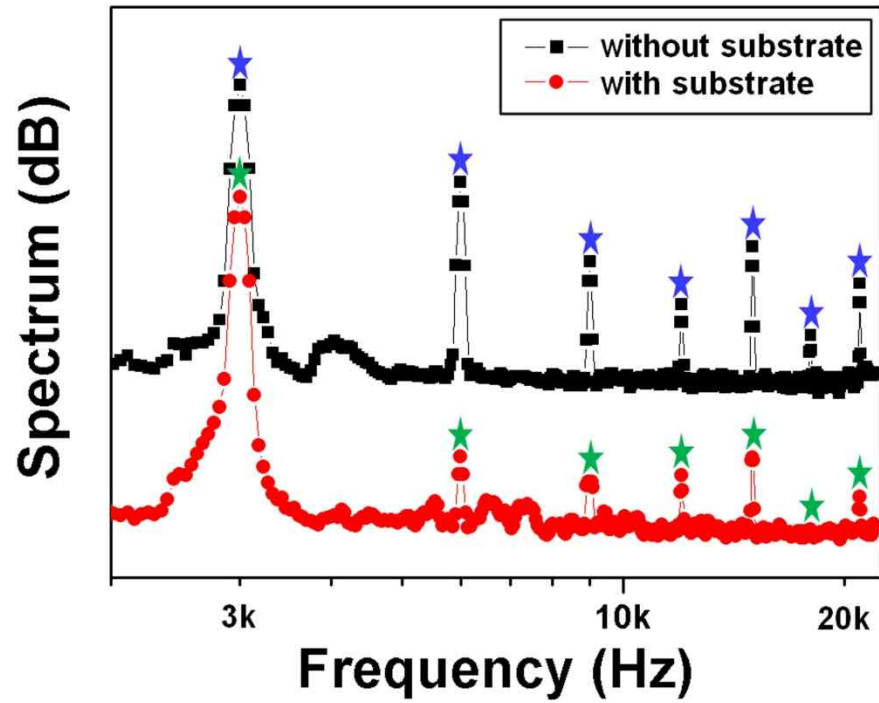
Figure 29. The ANC effect on the harmonics of graphene-based thin film transducer from 3 kHz tonal signal. A soft substrate (3M VHB 4910 acrylic form tape) was cleaved to the film to make an ANC actuator. [stars indicate harmonic sounds at multiples of 3 kHz.]

3.2. Size-Controlled Graphene Thin Films via Screen Printing and Its Applications

3.2.1. Graphene size control via mechanochemical method and their electro-responsive properties

A schematic diagram of the preparation for size-controlled graphite *via* the ball-milling process is shown in Figure 30. Natural flaked graphite (*ca.* 20 μm) is composed of layered graphene nanosheets; the carbon atoms are linked by covalent bonds. However, those carbon atoms positioned in adjacent planes are bound by much weaker van der Waals forces [130,131]. These weak interplanar forces enable the energy provided by ball milling to provide submicrometer-sized flakes whose size can be easily controlled by the ball-milling time (Figure 31). Three ball sizes (diameters: 1, 2 and 5 mm) were used. Size-controlled GO sheets were obtained from ball-milled graphite by a chemical exfoliation process according to a modified Hummers method [132,133]. Figure 32 shows AFM images of size-controlled GO flakes as a function of the ball-milling time. Ball milling reduced the GO particles to submicrometer sizes and concurrently transformed the particle morphology from flake to spherical, with a slight increase in thickness. TEM images shown in Figure 33 reveal that an aqueous dispersion of ball-milled GO had a narrower particle size distribution (*ca.* 400–700 nm) than non-milled GO (*ca.* 0.6–5 μm).
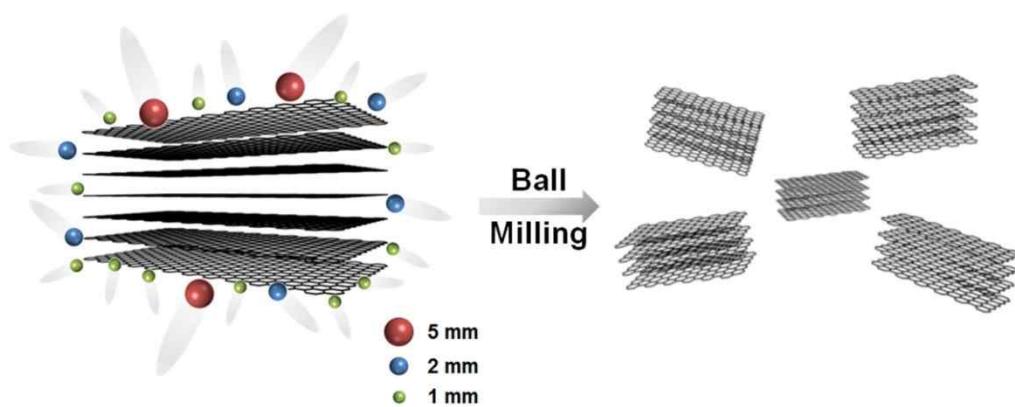
Figure 30. Schematic illustration of the production of size-controlled graphite *via* ball milling using three balls (diameters: 1, 2 and 5 mm).
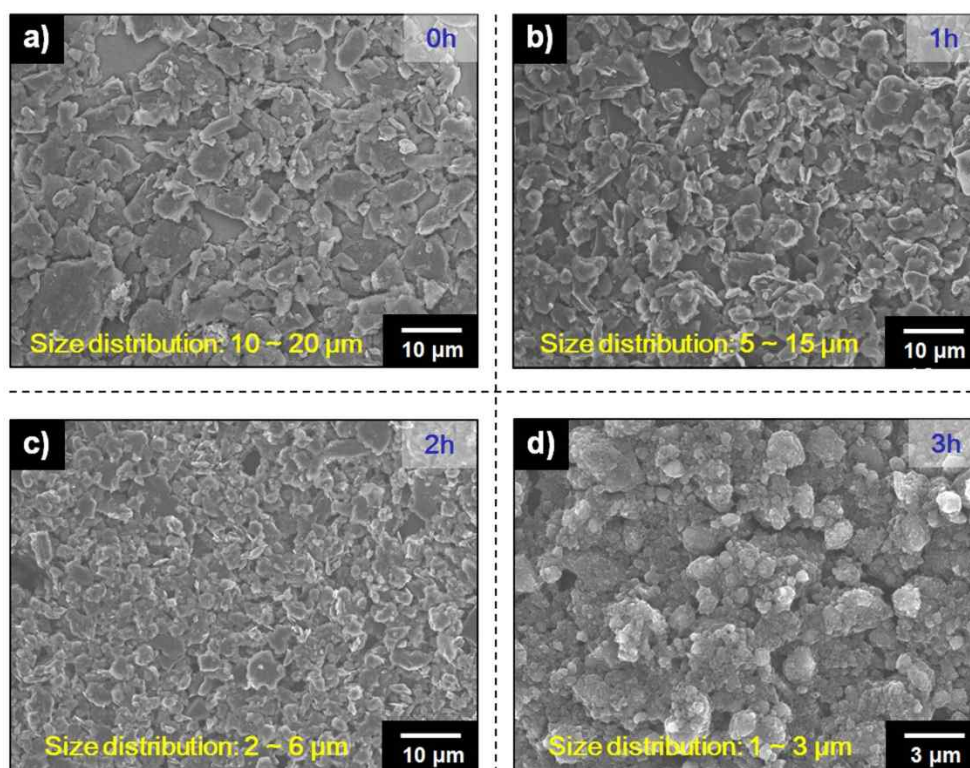
Figure 31. Representative SEM images of size-controlled graphite as a function of ball milling time.
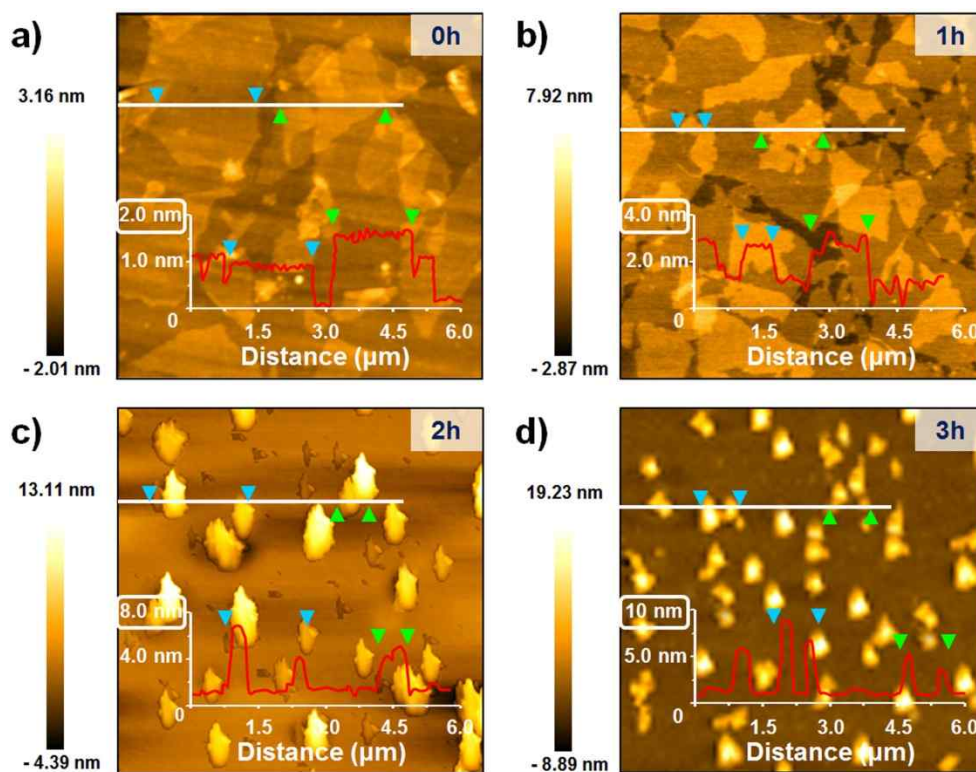
Figure 32. Representative AFM images of size-controlled GO as a function of ball-milling time. The GO solution was deposited on a silicon wafer for AFM analysis.
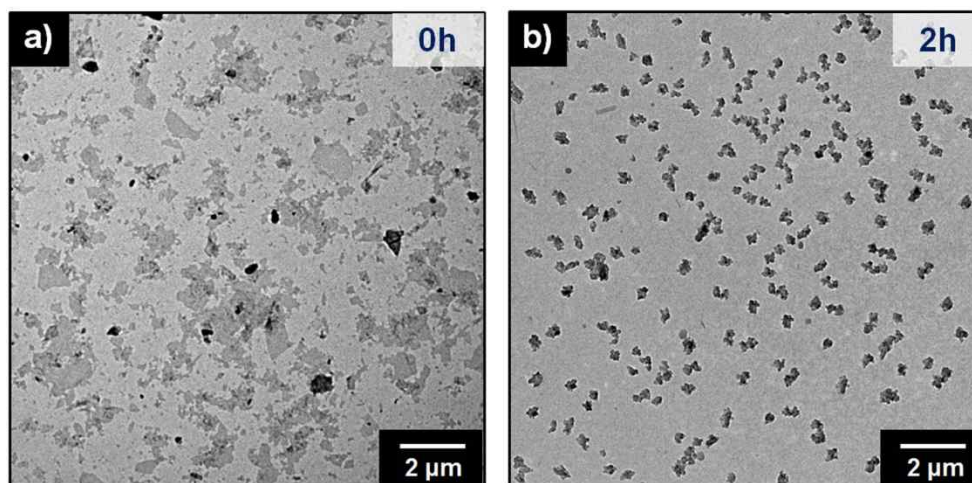
Figure 33. TEM images of a) 0-h and b) 2-h ball-milled GO. TEM samples were prepared by casting a GO solution onto a copper grid.

XPS analysis was used to further understand the effect of ball milling (Figure 34). The GO C 1s signal has three components, which correspond to the C=C/C−C in aromatic rings (284.5 eV), C−O (286.6 eV), and C=O (288.5 eV) functional groups. The I_{C-O}/I_{C-C} ratio increased from 0.45 to 1.31 after 3 h of ball milling. This increase was attributed to an increase in the surface area with decreasing GO size. Oxygen functional groups were introduced into the graphene basal and edge planes *via* the chemical exfoliation process. Active sites on the ball-milled GO surface could bind more oxygen functional groups because of the greatly increased surface area. The electrical conductivities of the synthesized ball-milled GO sheets were measured using a four-probe method. All of the conductivities were less than 1.0×10^{-6} S cm^{-1}, which is sufficient for a direct ER application, without requiring any post-treatment. The smaller size and high numbers of oxygen functional groups on the ball-milled graphene sheets resulted in enhanced dispersibility in silicone oil, eliminating the need for a solvent exchange process.

Figure 35 shows the shear stress and shear viscosity flow curves as a function of the shear rate for synthesized GO-based ER fluids at a volume fraction (vol%) of 3 under 1 kV mm^{-1} of electric field strength. Under an applied electric field, all of the prepared ER fluids displayed a shear stress plateau region over a broad range of shear rates, typical of Bingham plastic
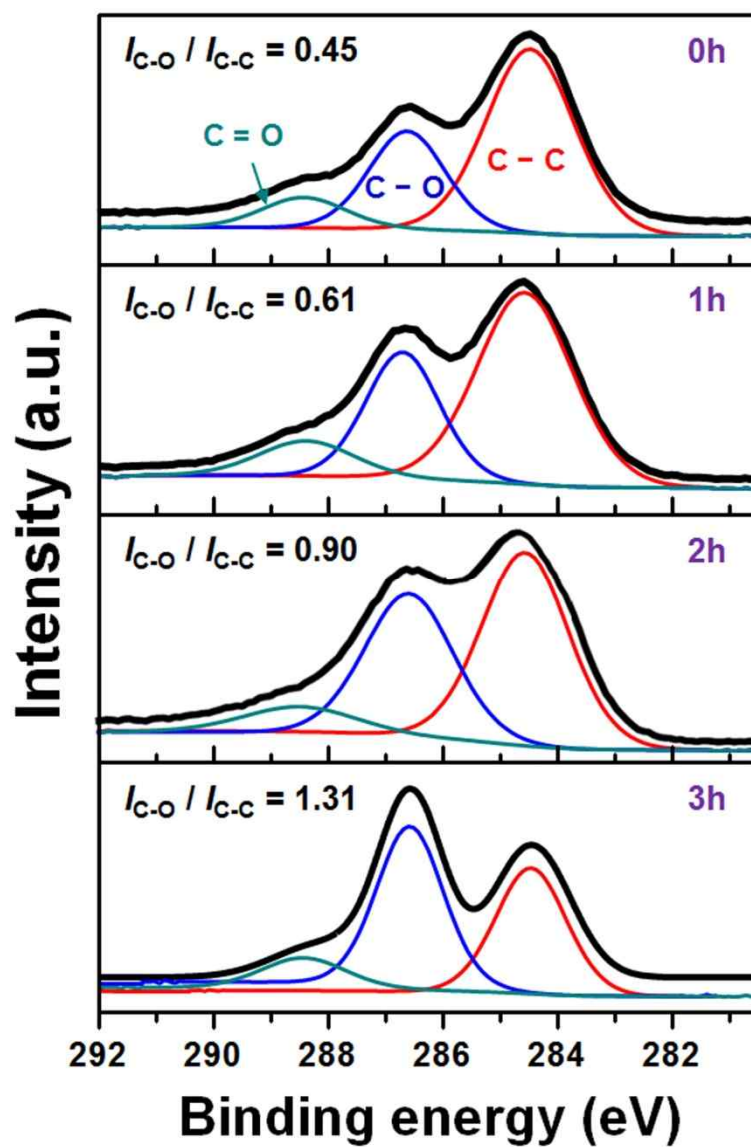
Figure 34. Deconvoluted XPS spectra in the C 1s region of size-controlled GO as a function of ball-milling time. Powdered samples were used for the XPS analysis. The fitted peaks correspond to the C−C, C−O, and C=O functional groups.
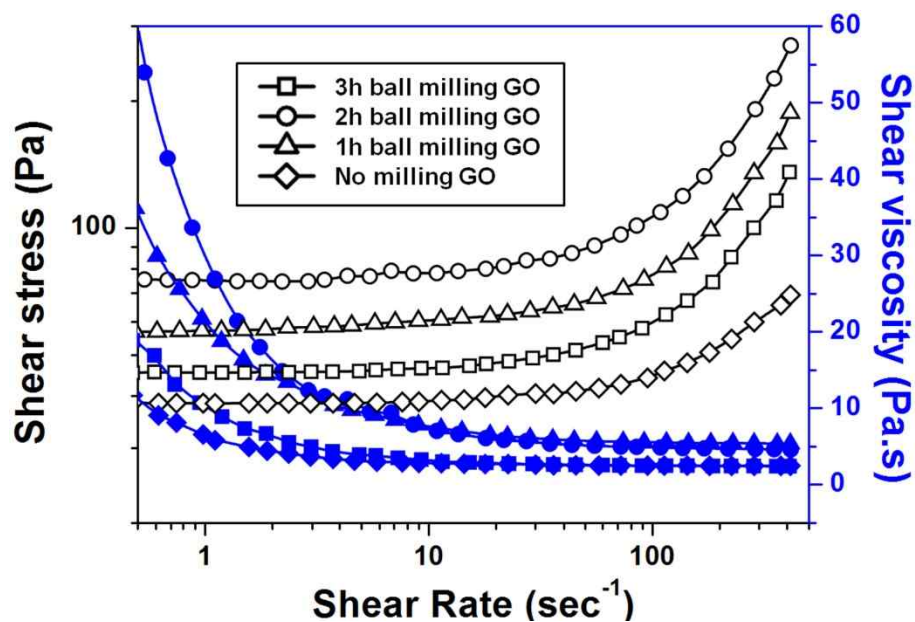
Figure 35. Shear stress (open symbols) and shear viscosity (closed symbols) of size-controlled GO-based ER fluids (3 vol% in silicone oil under a 1 kV mm^{-1} electric field).

behavior [134,135]. These results indicate that the interface of the synthesized GO began to polarize; electrostatic interactions between the GO sheets could occur through such interfacial polarization. The hydrostatic force generated by the shear flow opposed these interactions. Beyond the critical shear rate ($\dot{r}_{crit}$), the shear stress increased gradually with increasing shear rate, corresponding to typical Newtonian fluid behavior [136,137]. Notably, all of the ball-milled GO-based ER fluids displayed similar flow curves in the high shear rate region, behavior that was ascribed to shear deformation. The chain-like structure of the ER fluids began to degrade under the high shear forces in the high shear rate region, whereas the structural stability was maintained at low shear rates. The GO-based ER fluids containing GO ball-milled for 2 h had the best ER performance. This result was attributed to the size and morphology of the graphene sheets. In terms of the graphene-based ER fluid behavior, a flake-like morphology enhances performance relative to a spherical form because of the higher shear stress applied per unit sheet area. Smaller particles can also improve the performance because of stronger dipole polarization in the chain-like structure. The permittivity (ε') was obtained as a function of the GO size (Figure 36). The addition of GO significantly improved the permittivity of the pristine silicone oil-based ER fluid. The values slightly increased with decreasing GO particle size. Ball milling reduced the particle size and
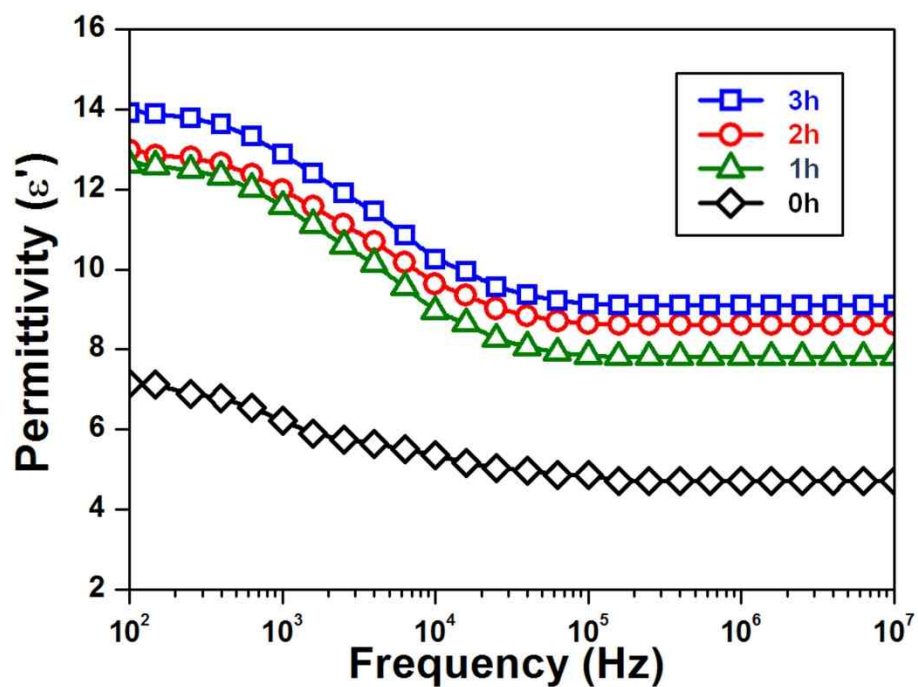
Figure 36. Permittivities of size-controlled GO-based ER fluids as a function of the ball-milling time. The measured permittivity of the pristine silicone oil-based ER fluid was *ca.* 2.4 at 105 Hz.

concurrently increased the number of polar groups. This facilitated the transportation of charges *via* rearrangement, and thereby improved the permittivity of the ball-milled GO-based ER fluids. The ER characteristics reached a maximum at 2 h of ball-milling time (shear stress of 78.5 Pa at a shear rate of 1 s^{-1}); this ER efficiency was double that of the non-milled GO-based ER fluid. The shear viscosities of the synthesized GO-based ER fluids were also measured. Apparent shear thinning behavior was clearly observed in the low shear rate region according to the Bingham model. Ball-milled GO sheets with outstanding dispersibility had a relatively high off-field viscosity compared with non-milled GO sheets. The value of the 3-h ball-milled GO-based ER fluid was *ca.* 0.623 Pa s, which is 2.6 times that of the non-milled GO-based ER fluid (Table 2).

An applied electric field (1 kV mm^{-1}) was alternately turned on and off to evaluate the real-time responses of the synthesized GO-based ER fluids (Figure 37). The shear stress values of all of the prepared ER fluids immediately increased once the electric field was applied. In contrast, the values rapidly decreased back to their original levels when the electric field was turned off. This indicates that the stress response of the prepared GO-based ER fluids was reversible and reproducible. Additionally, all of the GO-based ER fluid samples displayed low current leakage. The electric density was less than 10

Table 2. ER activity of size-controlled GO-based fluids.

Ball-milling time [a] (h)	0	1	2	3
Off-field viscosity (Pa s)	0.244	0.512	0.588	0.623
Response time (s)	16.4	7.6	4.9	5.5
Recovery time (s)	7.1	5.0	3.8	4.4
ER efficiency (%)	305	510	630	450

[a] Size-controlled GO was dispersed at 3 vol% in silicone oil (shear rate of $1 \ \mathrm{s}^{-1}$).
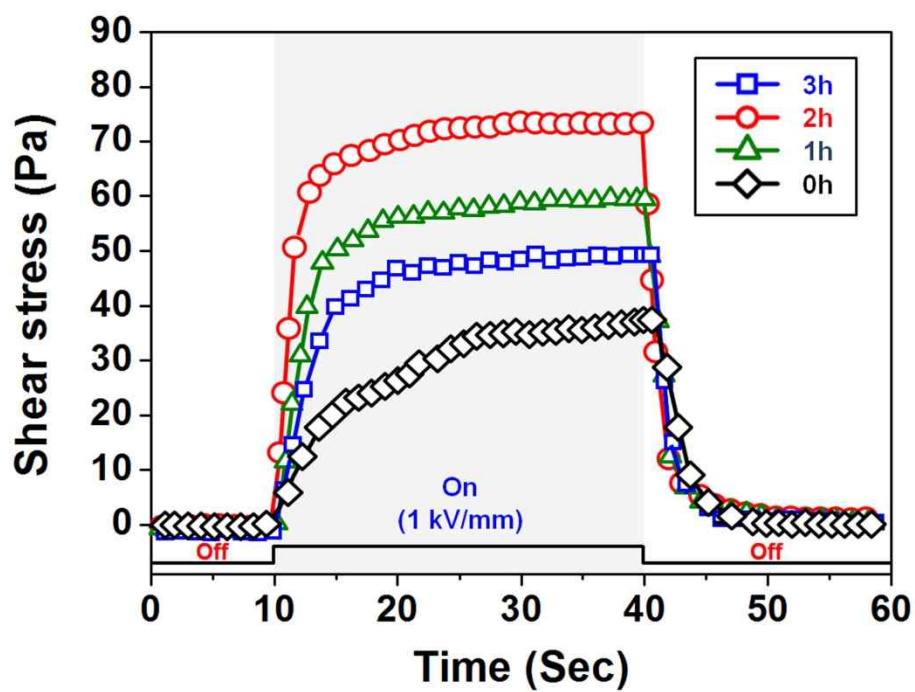
Figure 37. Effect of switching the applied electric field on the shear stress of sized-controlled GO-based ER fluids (at a shear rate of 1 s^{-1}).

μA cm^{-2} at an electric field strength of 1 kV mm^{-1}. However, the synthesized GO-based ER fluids had variable response times (t_{res}) and recovery times (t_{rec}) (defined as the time required for the response or recovery to reach 90% of its final or initial value). The response and recovery times tended to decrease with increasing ball-milling time because the size of the GO sheets affected the viscous drag forces (Table 2). Smaller GO particle sizes could potentially form chain-like structures rapidly and with higher mobility. The synthesized GO-based ER fluids also displayed significantly different ER activities in terms of their ER efficiencies (defined as $(\tau_E - \tau_o)/\tau_o \times 100$, where τ_E and τ_o are the shear stresses with and without an applied electric field strength, respectively). At a shear rate of 1 s^{-1}, 2-h ball-milled GO had a much higher ER efficiency (630 %) than non-milled GO sheets (305 %).

The influence of the GO vol% on the dynamic yield stress was evaluated for an in-depth insight into the ER activity of the synthesized GO-based ER fluids. Figure 38 shows that the yield stress increased dramatically with the GO vol%. Notably, the yield stress of 2-h ball-milled GO-based ER fluid at 3 vol% was 5.3 times higher than that of the same ER material at 1 vol%. Improved interplanar interactions of the GO sheets caused a greater resistance to deformation in shear flow at the higher vol%. Additionally, the maximum yield stress of the GO-based ER fluids increased with decreasing diameter of the GO
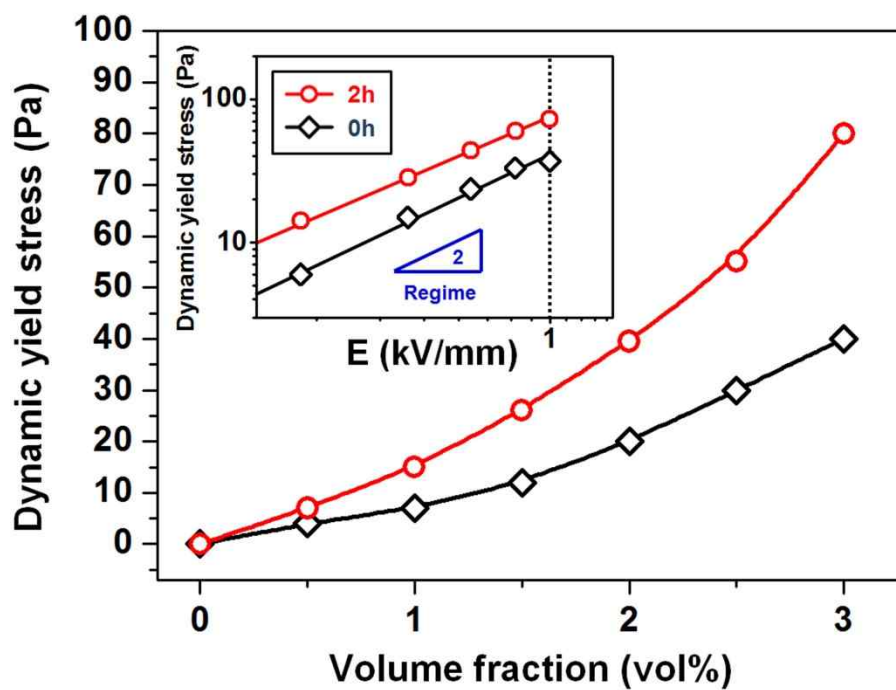
Figure 38. Dynamic yield stress as a function of the vol% for 0-h and 2-h ball-milled GO-based ER fluids under a 1 kV mm^{-1} electric field (inset: dynamic yield stress *vs.* electric field strength).

sheets. Electrostatic interactions were sufficient to counteract the hydrodynamic interaction in shear flow stemming from the high surface area of the ball-milled GO. The relationship between the yield stress (τ_y) and the electric field strength is plotted on a log–log scale in Figure 38 (inset). As with most ER fluids, the yield stresses of all of the synthesized GO-based ER fluids were directly proportional to the square of the applied electric field strength, as indicated by the slope of 2.0, in agreement with the polarization model of the ER mechanism [138,139].

A microstructural transition of 2-h ball-milled GO-based ER fluid was observed by optical microscopy under an applied electric field. An ER device with a gap distance of 1.00 mm was designed to investigate the GO-based ER fluid behavior in an electric field (Figure 39). Once the electric field was applied, the randomly dispersed GO sheets began to form a fibrillar structure in the direction of the applied electric field (Figure 40). It took only a few milliseconds to form the chain-like structure. It is known that the electrostatic interactions between ER materials are enhanced by increasing the electric field strength. The aligned fibrous structure, formed by electrostatic interactions between the GO sheets, rapidly reforms its structure under a shear force and has better resistance to shear flow.
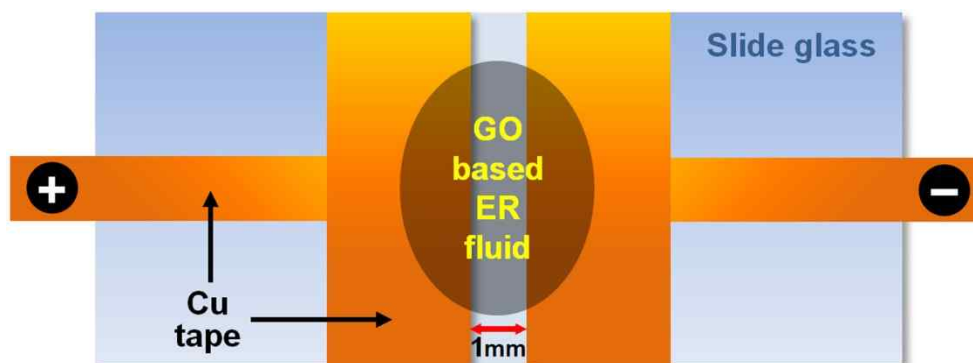
Figure 39. Device designed for the study of GO-based ER fluid behavior in an electric field. Copper tape was used to lower the contact resistance with the power source and to maintain the output voltage.
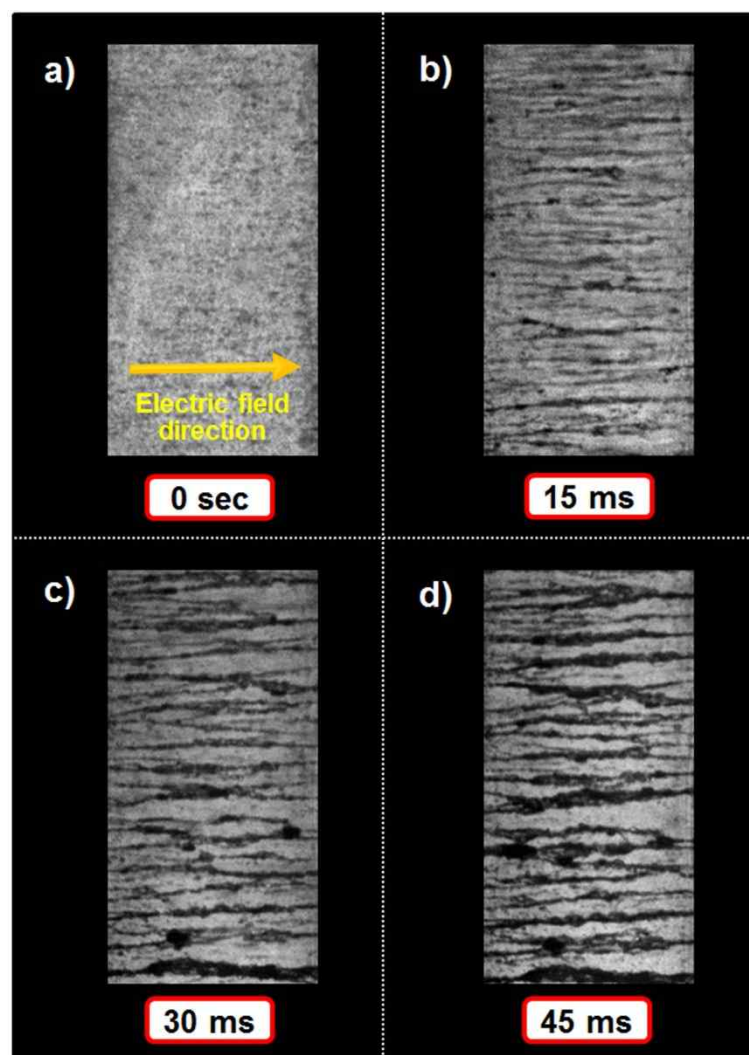
Figure 40. Optical microscopy images of 2-h ball-milled GO dispersed at 3 vol% in silicone oil under a 1 kV mm^{-1} electric field. The gap between the two electrodes was fixed at 0.5 mm.

DLS was used to investigate the particle size distribution of 2-h ball-milled GO in silicone oil (Figure 41a). The average diameter was *ca.* 3.43 μm, and the inset shows the outstanding dispersibility in silicone oil. The 0-h ball-milled GO-based ER fluid had a broad particle size distribution, with an average diameter of *ca.* 80.45 μm (Figure 41b). These findings demonstrated that the ball-milled GO had much better dispersibility in silicone oil than 0-h ball-milled GO because of its smaller size and higher oxygen functional group content.

Notably, ball-milled GO dispersed at 3 vol% in silicone oil had a better sedimentation ratio than the equivalent non-milled GO dispersion (Figure 42). Increasing the ball-milling time greatly decreased sedimentation; no sediment was evident after ninety days. This superb dispersion stability relates to the sedimentation velocity (V_g), which is a significant factor in particle precipitation. Stokes' law is commonly used to calculate the rate of sedimentation; it indicates that the motion of a particle in a viscous liquid reaches an equilibrium condition having a uniform velocity or sedimentation rate. Stokes' law is expressed as follows:

$$V_g = d^2 \, (\rho_p - \rho_l) \, / \, 18\eta \times G$$

where d is the particle diameter, ρ_p is the particle density, ρ_l is the liquid density, η is the viscosity of the liquid, and G is the gravitational acceleration.
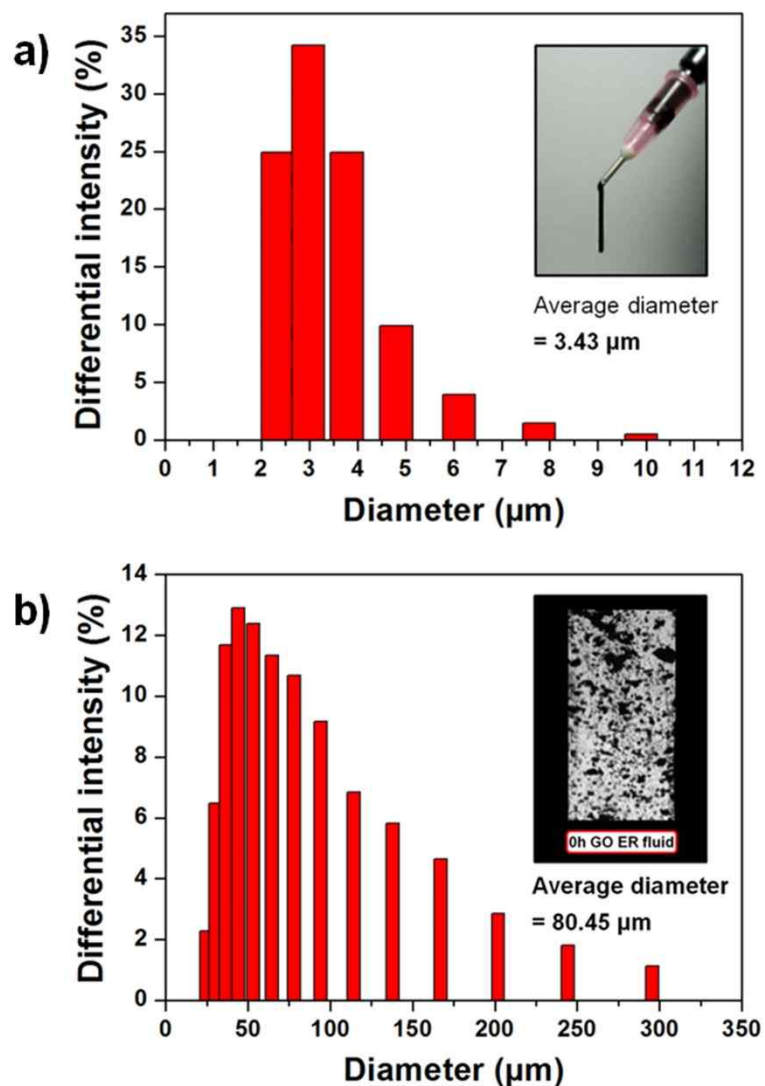
Figure 41. DLS analysis of a) 2-h and b) 0-h ball-milled GO dispersed at 3 vol% in silicone oil (inset: extrusion of 2-h ball-milled GO-based ER fluid from a needle and optical microscopy image of 0-h ball-milled GO-based ER fluid in the absence of an electric field).
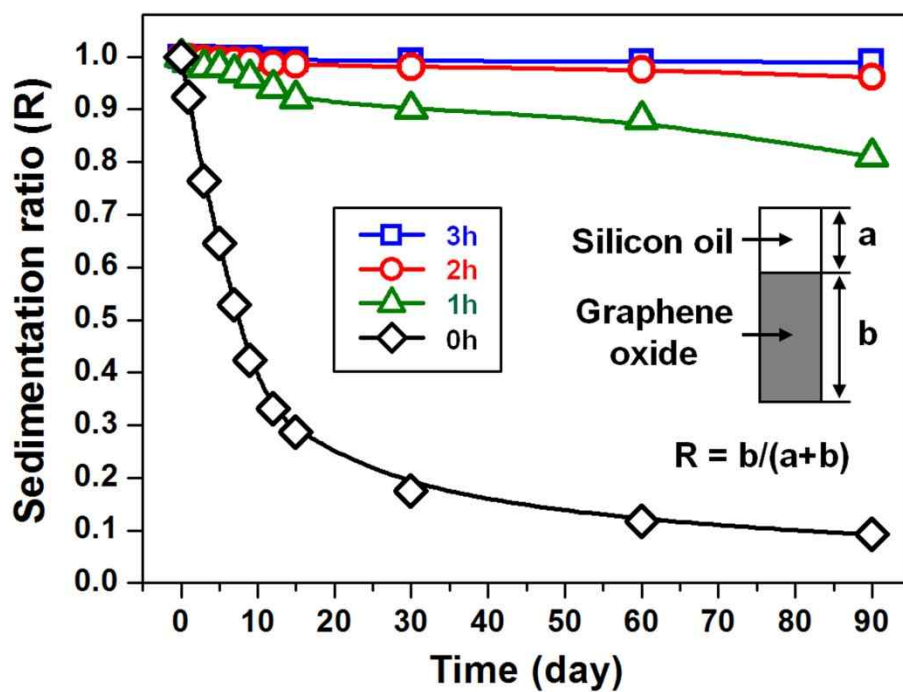
Figure 42. Sedimentation properties of size-controlled GO-based ER fluids (3 vol% in silicone oil) (inset: definition of the sedimentation ratio).

The density of the ball-milled GO was measured using a pycnometer (25 mL), and it was calculated by the equation as follows:

$$\rho_p = \frac{(W_0 - P)}{(W_2 - P) - (W_1 - W_0)} \times D$$

where P is the pycnometer mass and W_0, W_1, and W_2 are the masses of the particles, the particles and liquid, and the liquid in the bottle, respectively. The density (D) of water used as the liquid was taken as 1 g cm^{-3}. The densities slightly decreased with increasing ball-milling time (Table 3). Changes in pressure or temperature can affect densities. Ball-milled GO was obtained by chemical exfoliation of ball-milled graphite, which involved mechanical impact and heat generation. This process caused the GO flake morphology to transform into a spherical shape, and increased the particle thickness and volume. This morphological transformation *via* the mechanochemical process played a key role in reducing the GO density. As a result, the V_g of 2-h ball-milled GO sheets was *ca.* 77 times slower than that of non-milled GO sheets. The low settling velocity of isolated GO sheets and the electrostatic repulsions between oxygen functional groups on the GO sheets are expected to have a combined effect on the anti-sedimentation property.

Table 3. Physical parameters and V_g value of size-controlled GO in silicone oil.

Ball milling time (h)	0	1	2	3
GO diameter [a] (nm)	600–5000	700–1500	400–700	200–300
GO thickness [a] (nm)	0.5–1.5	1.5–3	3–8	4–10
GO density [b] (g cm^{-3})	1.83	1.78	1.56	1.53
Fluid density [c] (g cm^{-3})	0.97	0.97	0.97	0.97
Fluid viscosity [c] (Pa·s)	0.097	0.097	0.097	0.097
V_g [d] (m s^{-1})	2.057×10^{-7}	2.590×10^{-8}	2.702×10^{-9}	2.351×10^{-10}

[a] The average GO diameter and thickness were determined by AFM and TEM analysis.

[b] The GO density was measured by pycnometr at 20°C.

[c] Silicone oil (poly(methylphenylsiloxane), viscosity = 100 cSt) was used as the dispersing medium.

[d] The sedimentation velocity was calculated using Stokes' equation.

3.2.2. Highly conductive, flexible and scalable graphene hybrid thin films with controlled domain size as transparent electrodes

The properties and structure variation of size-controlled GO and graphene as a fuction of ball milling time are shown in Figure 43. Size-controlled GO was used as a conducing ink for screen printing. The reduction process for graphene sheets was performed by mild thermal annealing with hydrazine vapor deposition and pressure-assisted heat treatment using hot press [140]. As a result of the mechanochemical method, the diameter of GO sheet highly reduced (200–300 nm), whereas the thickness gradually increased (4–10 nm) (Figure 43a). To gain more insight into the size-controlled GO and graphene property, XPS and Raman analysis were conducted (Figure 43b). The result was that I_{C-O}/I_{C-C} ratios of 0h and 3h ball-milled GO decreased from 0.85 and 1.51 to 0.35 and 0.77 via reduction process, respectively (Figure 44). Moreover, the Raman spectrum indicated an increased I_D/I_G intensity ratio and reduced 2D peak intensity (Figure 45). The increased defects can be attributed to the structural edge effects from the average size reduction of the sp^2 domains. Namely, active sites of ball-milled GO sheets with small domain size could afford to bind more oxygen functional groups on basal and edge planes due to their high surface area. For this reason, ball-milled graphene sheets had low conductivity comparing to non-milled graphene sheets.
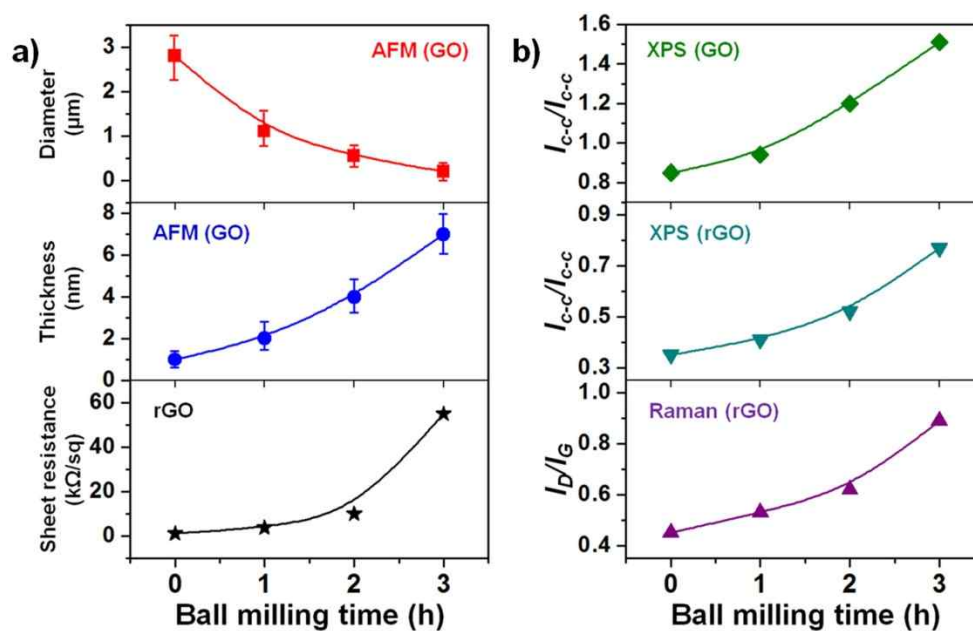
Figure 43. Properties and structure variation of size-controlled GO and graphene as a function of ball milling time. Size and thickness were detected by AFM analysis, and peak intensity ratios of the C−O to C−C and the D to G were obtained from XPS and Raman spectra, respectively.
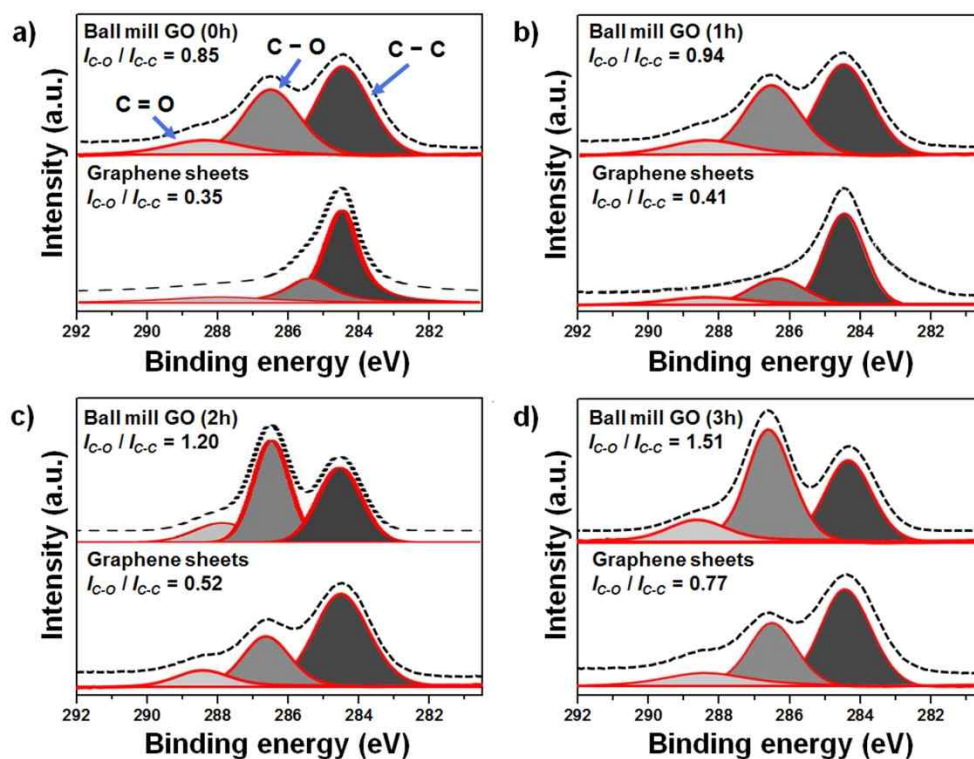
Figure 44. Comparison of deconvoluted XPS spectrum of size-controlled GO and graphene-based thin films as a function of ball milling time in the C1s region.
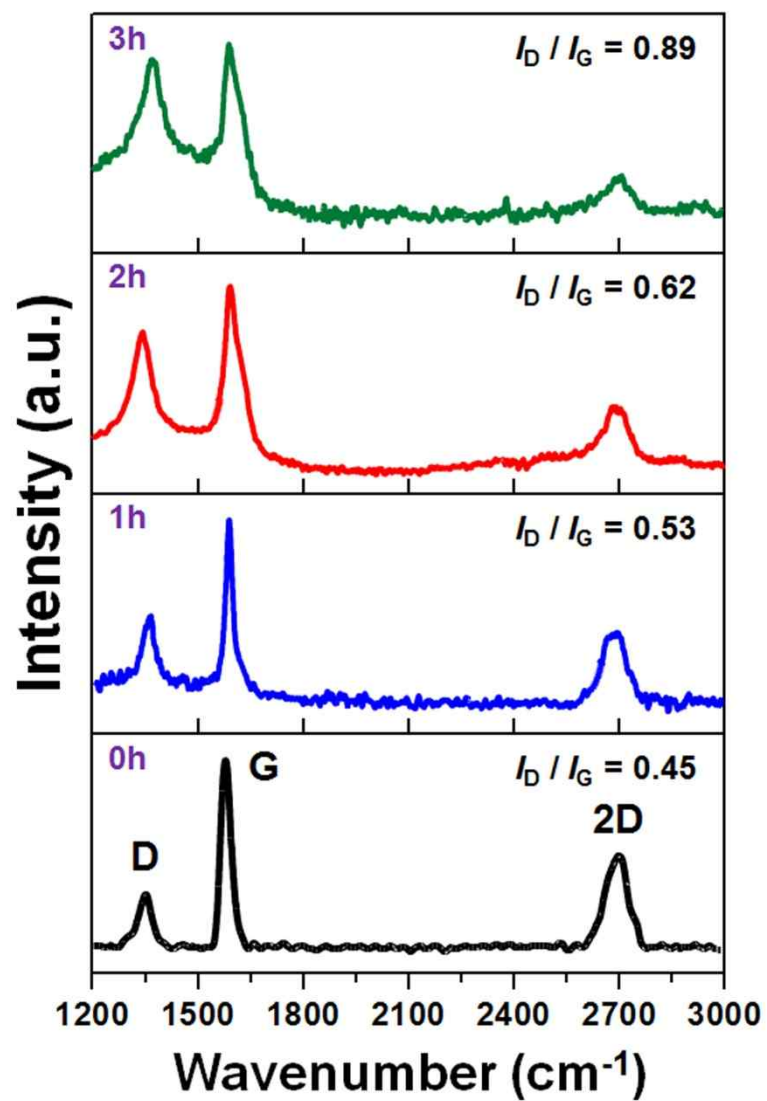
Figure 45. Raman spectra of size-controlled graphene-based thin films according to ball milling time showing D, G, and 2D peaks.

In order to investigate the size confinement effect to electrical property of graphene sheets for transparent conductive electrode, graphene hybrid thin films with controlled domain size were fabricated on PES film according to the weight content (wt%) of size-controlled graphene under same transmittance of 81 % (Figure 46a). As a result, it was noteworthy that the hybrid thin film with 20 wt% of 2h ball-milled graphene had a low sheet resistance of 0.73 kΩ sq^{-1}. This is *ca.* 1.5 times lower than the sheet resistance of pristine graphene thin film, thus suggesting a bridging effect of small domain-sized graphene (400–700 nm) between adjacent graphene layers with micometer size along the horizontal and vertical axes. In the case of 1h ball-milled graphene, the sheet resistance has been minimized at 10 wt%. As the concentration increased to over optimum point, the conductivity of graphene hybrid thin film decreased. In particular, when the 3h ball-milled graphene was mixed in graphene hybrid film, this phenomena has disappeared due to its very small domain size and low conductivity, which is insufficient to play a connection role. Furthermore, the fine tuning of the surface sheet resistance and transmittance was accomplished by controlling the number of screen printing (Figure 46b). Overall, the transmittance and sheet resistance of graphene hybrid thin films have decreased as increased printing steps. Especially, the graphene hybrid thin films with 2h ball-milled graphene had sheet resistances of 0.49, 0.66 and 1.51
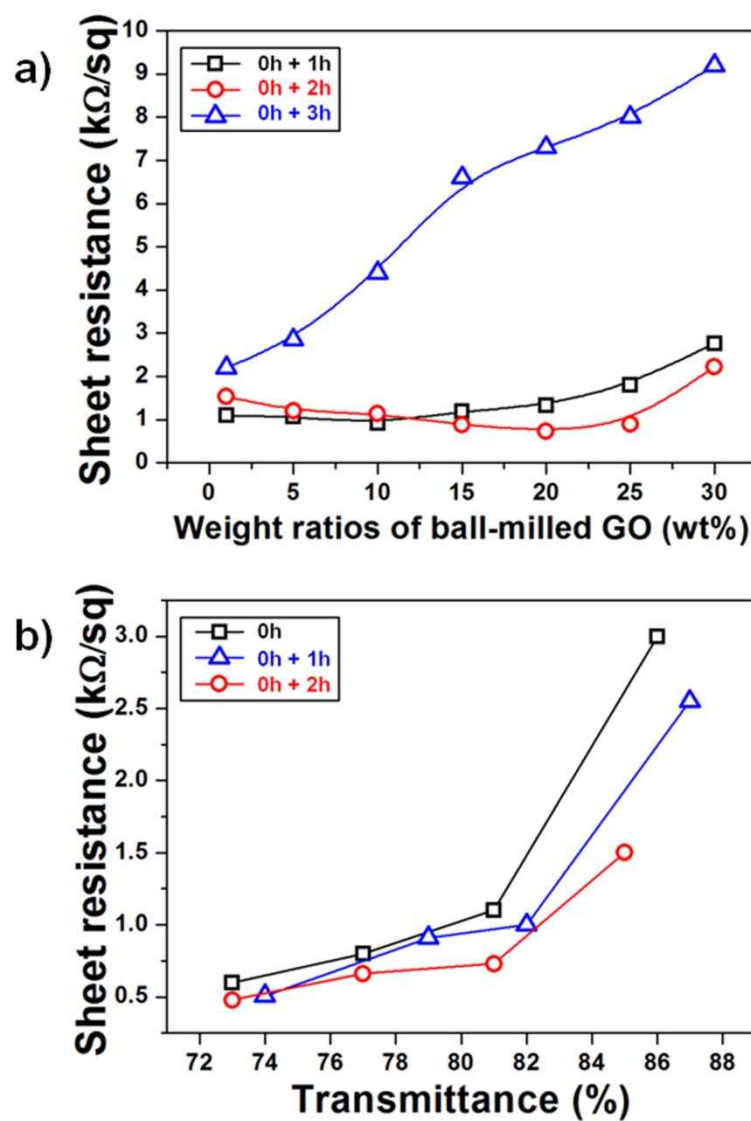
Figure 46. Sheet resistance of graphene hybrid thin film as a function of a) ball-milled GO concentration and b) transmittance. Film transmittance was controlled by adjusting the number of screen-printing steps.

kΩ sq^{-1} at room temperature and transmittance (550 nm wavelength) of 73.25, 77.58 and 85.65 %, respectively.

To achieve an in-depth insight into the bridging effect by controlled domain size of graphene sheet, 3D AFM analysis of graphene hybrid thin film with 2h ball-milled graphene was conducted in comparision with that of pristine graphene thin film (Figure 47). As a result, it was proved that graphene hybrid thin film consisted of micrometer and submicrometer-sized graphene sheets. Most of all, the vacant lattice sites in the pristine graphene sheets have been filled with submicrometer-sized graphene sheets, which caused the short electron transport pathway. DLS analysis also shows that GO hybrid solution has various peak diameter with dense size distribution relative to pristine GO solution, which demonstrates a mixed domain size (Figure 48). In addition, GO hybrid solution exhibited a superior sedimentation ratio compared to that of pristine GO solution, and there is no sediment deposited after ninety days (Figure 49). According to the Stoke's equation, V_g values were 2.375 × 10^{-7} and 8.825 × 10^{-9} m s^{-1} for pristine GO and hybrid GO solution, respectively. It means that the V_g value of GO hybrid sheet is *ca.* 27 times slower than that of pristine GO sheet. Therefore, these filled domain property and outstanding dispersibility could lead to high reduction efficiency and low I_{C-O}/I_{C-C} ratio under pressure-assisted heat treatment (Figure 50). In other words, sufficient
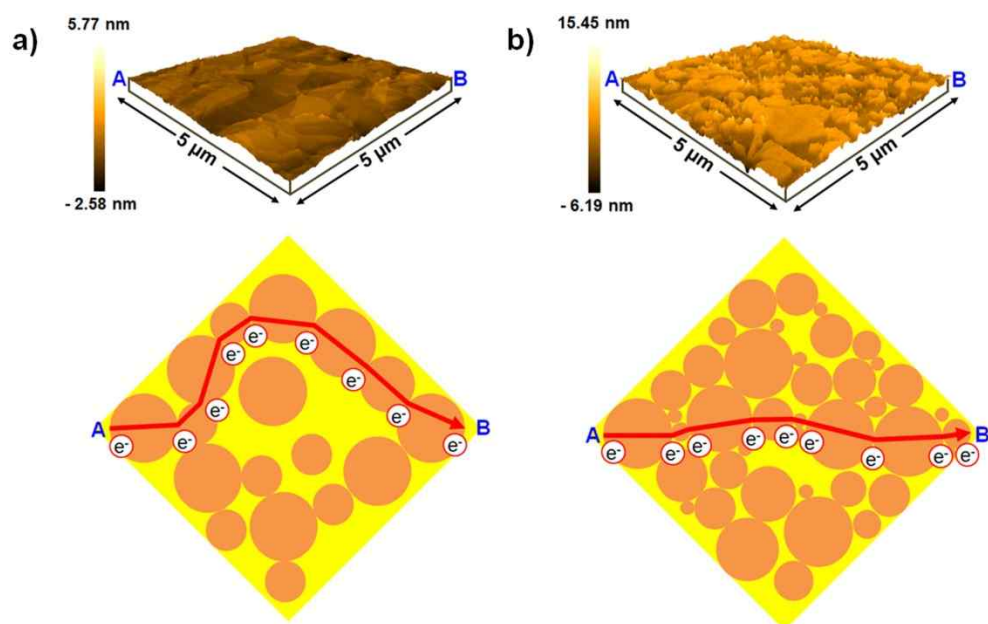
Figure 47. The 3D AFM images and schematic illustration showing electron pathway of a) pristine graphene and b) graphene hybrid thin films.
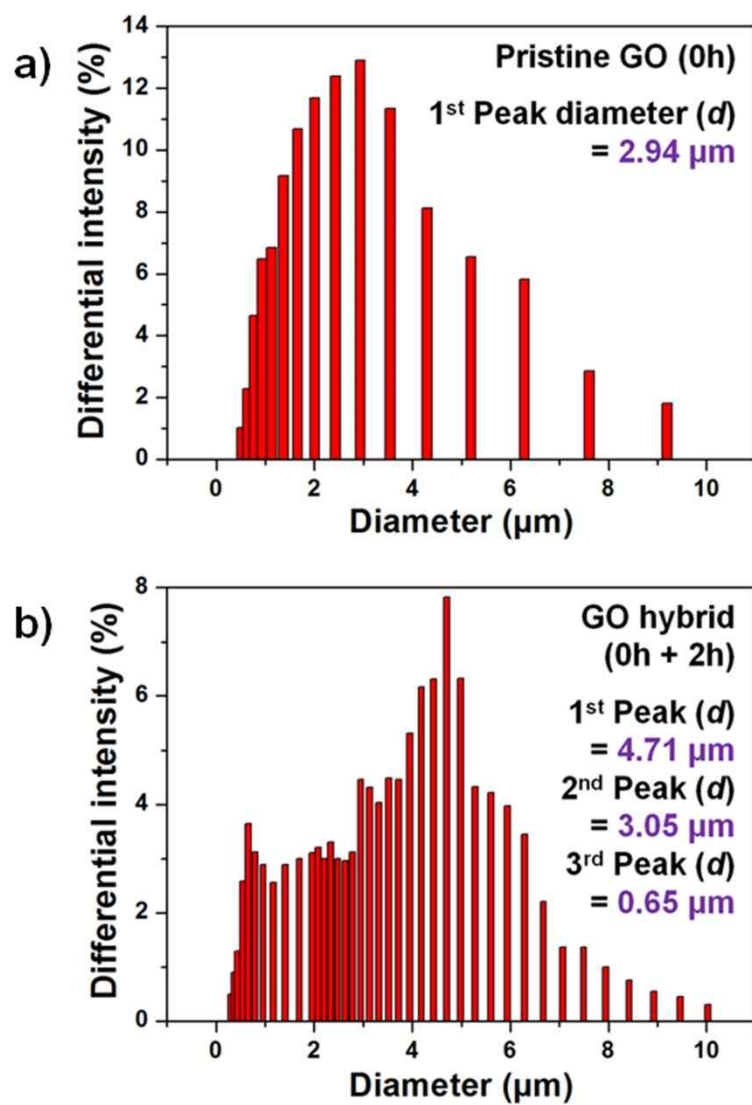
Figure 48. DLS analysis of a) pristine GO and b) GO hybrid solution.
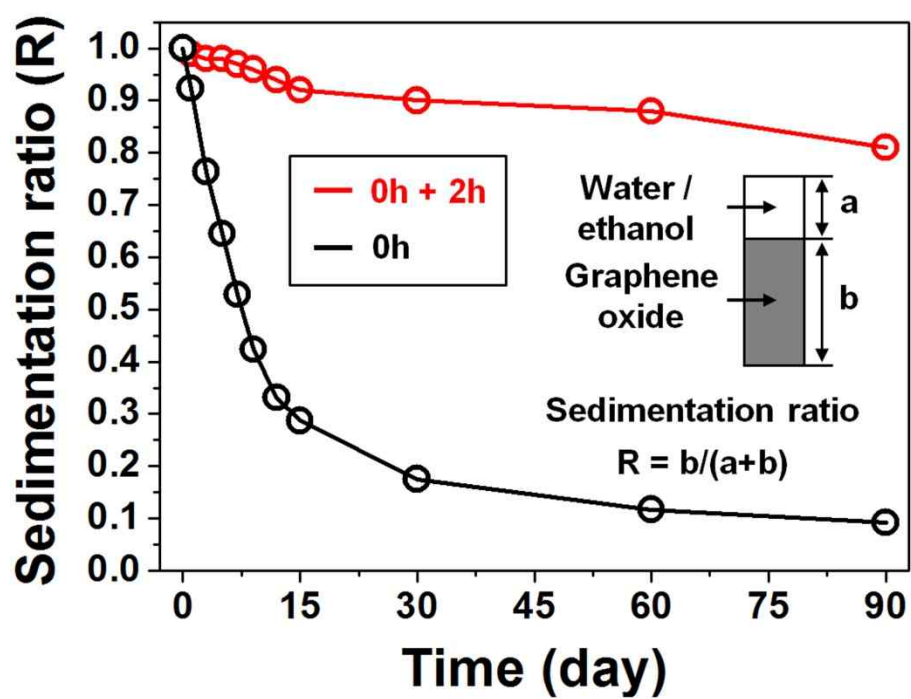
Figure 49. Sedimentation properties of pristine GO and GO hybrid solution (inset: definition of sedimentation ratio).
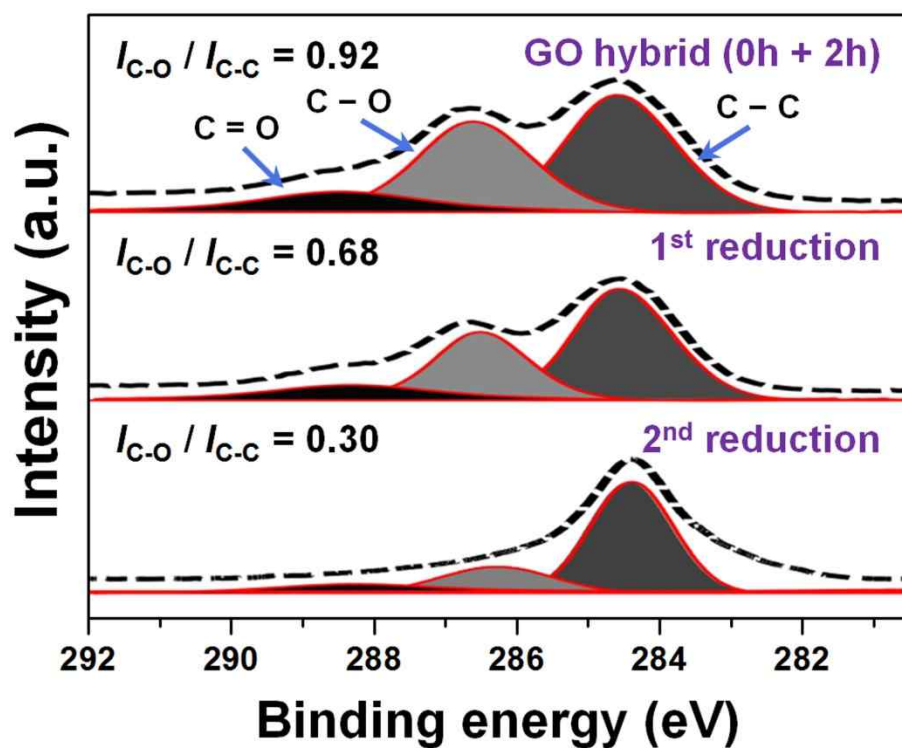
Figure 50. XPS spectrum of GO and graphene hybrid film via two step reduction process.

thermal energy by direct contact can be effectively trasferred to dissociate functional groups from GO hybrid thin film, minimizing the number of voids and maximizing the area of heat flow.

To assess the uniformity and flexibility, the pristine and graphene hybrid thin film with a 15-cm square pattern were fabricated via screen printing. The sheet resistance change is expressed as $\Delta R/R_s = (R-R_s)/R_s$, where R and R_s are the measured and initial average sheet resistance, respectively. Figure 51 shows that the graphene hybrid thin film had good interplanar electrical contact between the graphene sheets over about 14% of the sheet resistance distribution, compared to a 38% for pristine graphene thin film. Furthermore, electrical fatigue tests were performed using an external force. The overall sheet resistance increased in proportion to the folding angle (Figure 52a). Folding the hybrid thin film −180 ° (acute angle) and +180 ° (obtuse angle) led to approximately 10 and 12.5 % increases in sheet resistance, respectively. In the case of pristine graphene thin film, increased values were *ca.* 15.6 and 17.4 %, respectively, which indicated of high electrical fatigue damage. In addition, when the samples were released from bending after 500 cycles, R value of the pristine graphene and hybrid thin films increased by *ca.* 3.9 and 1.27 kΩ sq^{-1}, respectively (Figure 52b). This indicates a high degree of structural stability in the graphene hybrid thin film. Judging from these result,

Figure 51. Distribution of sheet resistance for pristine graphene and graphene hybrid thin films for a 15-cm square pattern.
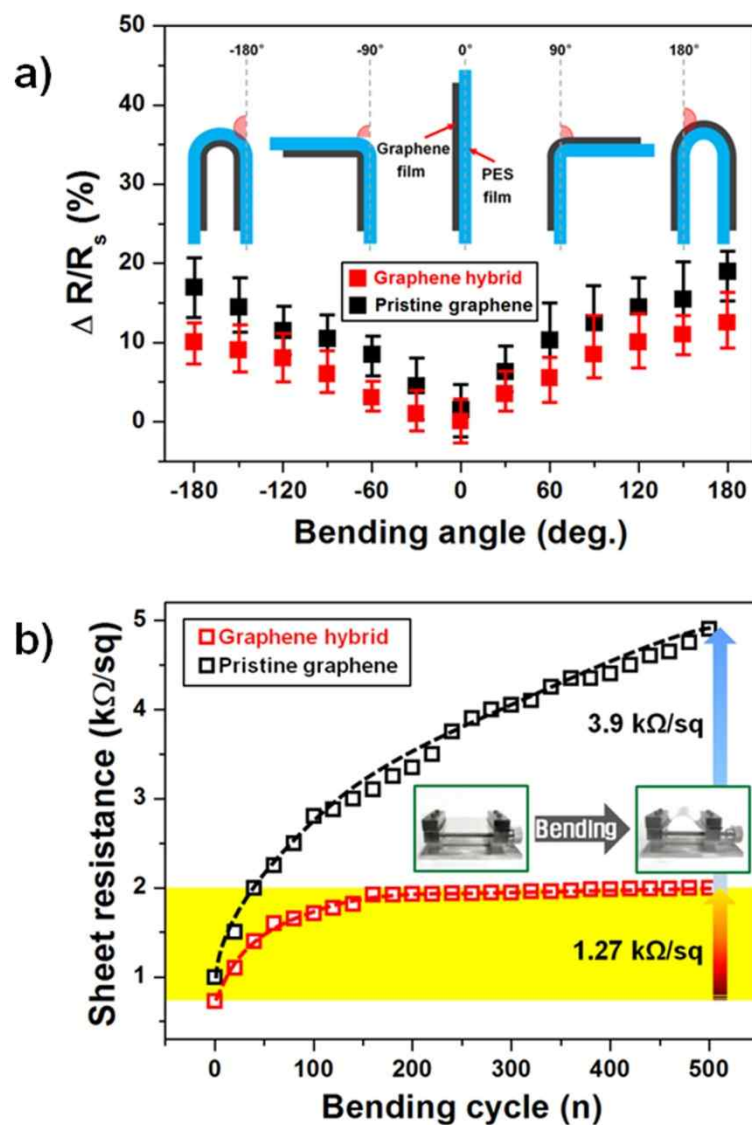
Figure 52. Sheet resistance changes of pristine graphene and graphene hybrid thin films according to the bending a) angle and b) cycle. Inset in (b): schematic diagram of folded film on PES substrate under compressive strain.

it was evident that domain size-controlled graphene acted as a bridge connecting graphene with micrometer size, and enhanced the interfacial interactions between graphene sheets. Moreover, outstanding dispersibility could make it possible to have improved adhesion of the graphene hybrid thin film to the flexible PES substrate.

3.3. Multilayered Graphene Thin Films via Screen Printing and Their Application

3.3.1. High electrothermal performance of expanded graphite nanoplatelet-based patch heater

A schematic of the fabricated EGnP via intercalation, expansion, and vacuum filtration is shown in Figure 53. The graphite intercalation compound was made from natural flaked graphite treated by chemical or electrochemical processes at 80 °C using an oxidizing agent and sulfuric acid, and the expansion process was conducted using sonication (Figure 54a). Figure 54b shows a Petri dish containing sub-kilogram quantities (*ca.* 0.5 kg) of EGnP, a very large quantity in laboratory synthesis. Generally, pristine graphite is composed of layered graphene nanosheets; the carbon atoms are held by covalent bonds. However, the graphite's carbon atoms positioned in adjacent planes are bound by much weaker van der Waals forces. For this reason, the weak interplanar forces can afford to intercalate certain atoms, molecules, and ions into the interplanar spaces of the graphite. As a result, small amounts of strong oxidants and acid enter into the graphite's interlayers more easily at lower temperatures, without the need for high temperatures associated with rapid heating. When combined with intercalated oxidants, the graphite allows hydrophilic functional groups to be introduced. SEM images showed that

126
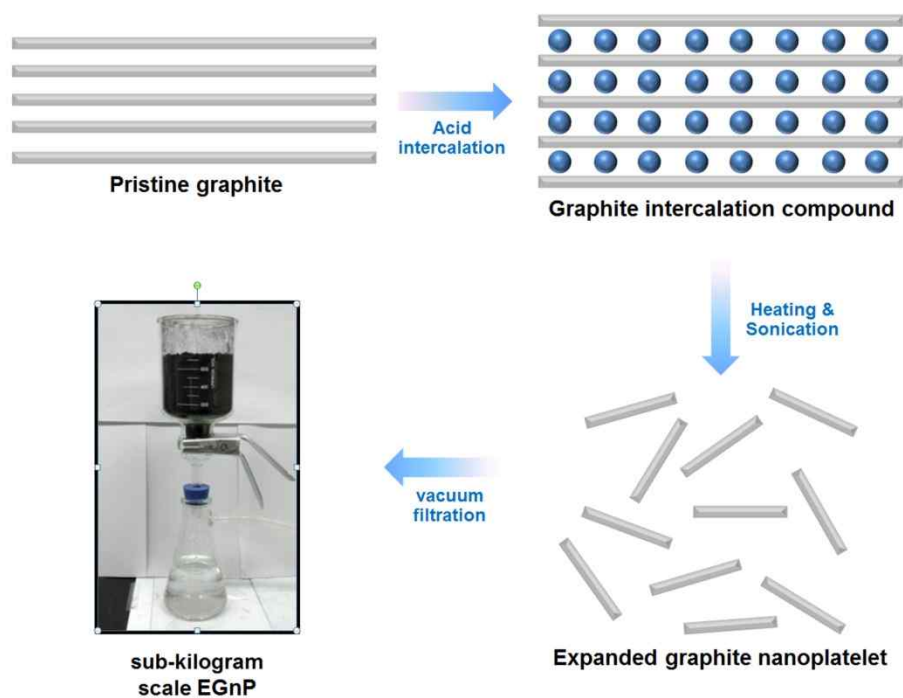
Figure 53. Schematic illustration of mechanism for sub-kilogram scale of EGnP via intercalation, expansion, and vacuum filtration. Intercalation was conducted by oxidizing pristine graphite with KPS and sulfuric acid at 80 °C.
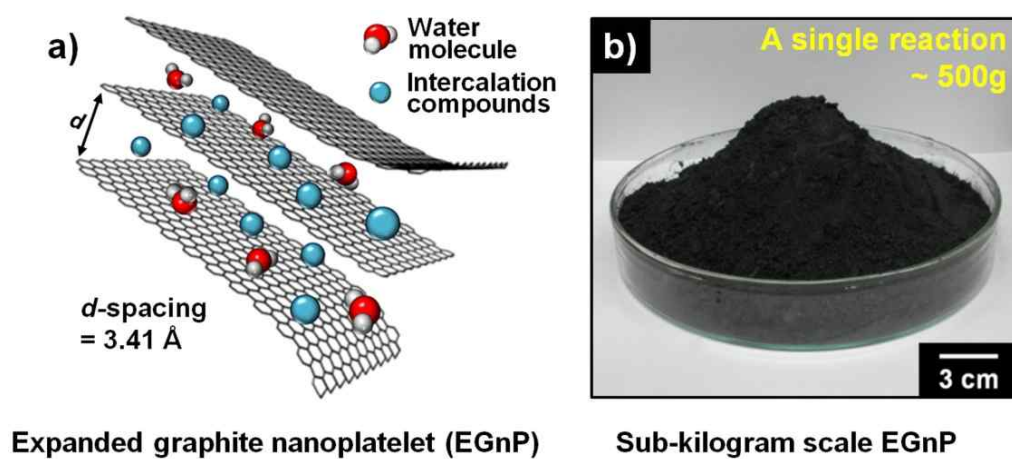
Figure 54. a) Schematic illustration of synthesized EGnP. b) The photo image of a Petri dish containing sub-kilogram quantities (*ca.* 500 g) of EGnP.

EGnP, composed of multilayer graphene, was successfully produced in a layer of 1–5 nm in thickness and 1–10 μm in diameter after intercalation and expansion from densely layered pristine graphite (Figure 55a and b).

To find the optimum conditions for EGnP synthesis in electrothermal applications, the molar concentration of the oxidizing agent was carefully controlled for identical acid concentrations. The surface resistance and interplanar spacing for various oxidizing agent molar concentrations are displayed in Figure 56a. The measurement of the electrical sheet resistance for a dried EGnP pallet after vacuum-filtration was obtained using the four-probe method. The interlayer spacing was calculated from Bragg's law. In general, the electrical conductivity determines the heater performance. EGnP had a low surface resistance, 10 Ω sq^{-1} for 150 mM concentration oxidizing agent, which was 15 times lower than the surface resistance of synthesized EGnP with only sulfuric acid, suggesting its potential as an electrothermal material for heater applications. The d-spacing value increased linearly with increasing initial molar concentration before reaching equilibrium. XRD data showed that EGnP derived from 150 mM concentration oxidizing agent had a sharp peak at 2θ of 26.2 ° in comparison to that of pristine graphite (26.6 °), which corresponded to a d-spacing values of 3.41 Å and 3.35Å, respectively (Figure 56b). The occurrence of this peak confirmed that the individual graphene nanosheets of
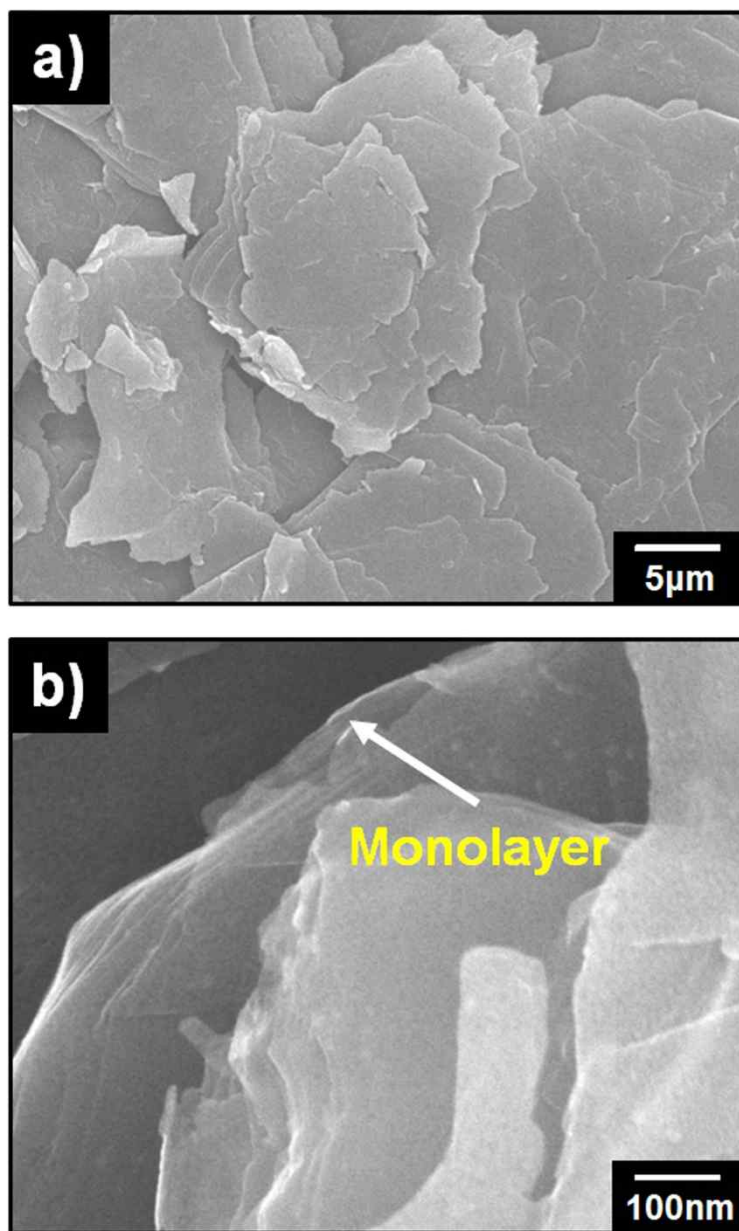
Figure 55. Representative SEM image of synthesized EGnP at a) low and b) high magnification. EGnP is composed of multi-layered graphene.
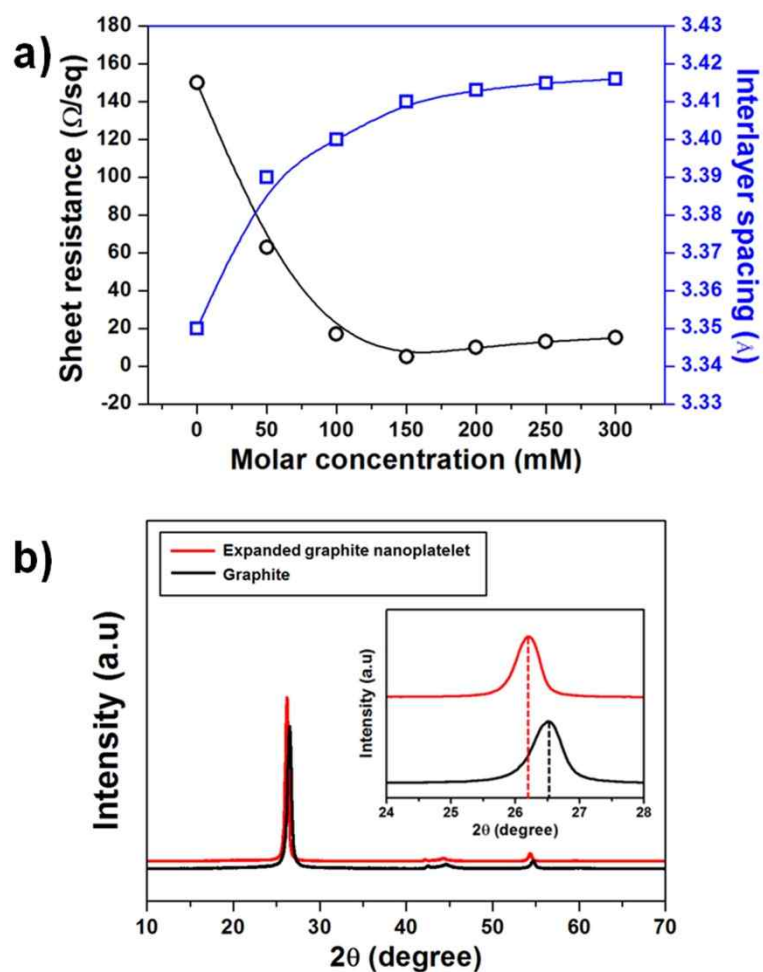
Figure 56. a) Surface resistance and d-spacing value of synthesized EGnP for different molar concentrations of KPS. b) The XRD patterns of pristine graphite and EGnP at 150 mM concentration of the oxidizing agent. The interlayer spacing was calculated from Bragg's law (X-ray wavelength, λ = 0.154 nm). For XRD sample preparation, power-type EGnP was used.

fabricated EGnP had an interlayer spacing of 3.41 Å and that the interplanar spacing had increased [141,142].

To gain insight into the electrical characteristics of EGnP, XPS analysis was performed. The deconvoluted C1s XPS spectra of pristine graphite and EGnP formed with a 150 mM concentration oxidizing agent are presented in Figure 57a. The C1s signal of graphite and EGnP consists mainly of two components: the C–C bonds in the aromatic rings (284.6 eV peak) and the C–OH bond (286.5 eV peak) [143]. The ratio I_{C-OH}/I_{C-C} increased from 0.15 (pristine graphite) to 0.60 (EGnP), as shown by the transformation into single sp^3 bonds during the intercalation process. The O1s XPS region was fitted to a combination of OH^- (532.1 eV) and H_2O (533.8 eV) species derived from H_2O wetting and decomposition (Figure 57b) [144,145]. Physical water adsorption during the expansion process to neat graphite increased the dissociative chemisorption of water. Notably, the I_{water}/I_{OH^-} ratio increased from 0.10 (pristine graphite) to 0.78 (EGnP), indicating the increase of water in synthesized EGnP. With increasing molar concentration of the oxidizing agent, the small amount of trapped water in EGnP clearly enhanced its conductivity, which conferred that the active sites on EGnP become saturated; the excess water molecules were free to rotate and diffuse [146]. In general, water molecules would be strongly bound to the host molecules like several ions at
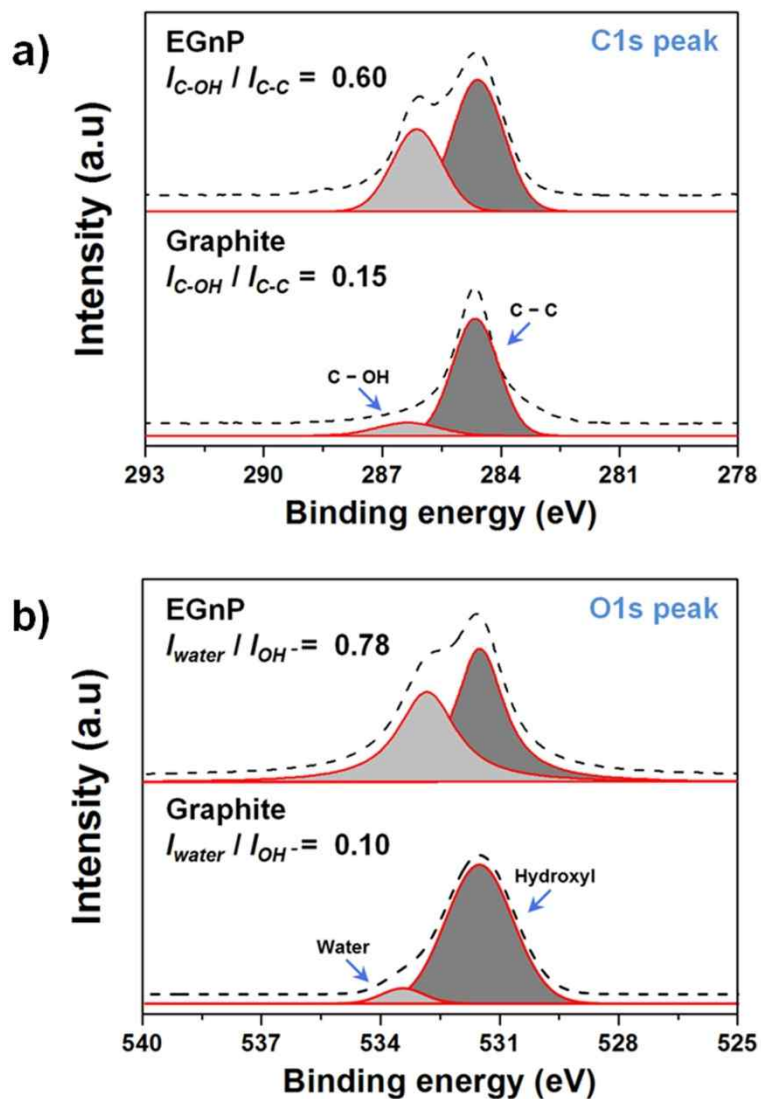
Figure 57. Deconvoluted XPS spectra of graphite and EGnP for a) C1s and b) O1s. The fitted lines of the XPS analysis are labeled as C–C and C–OH bonds in the C1s region, and water adsorption and OH$^-$ in the O1s region. For XPS sample preparation, an EGnP aqueous solution was deposited on a Si wafer using screen printing.

low concentration, being its reorientation highly restricted. However, the rotational freedom of water molecules increases at higher water concentration, since an excess amount of water molecules is surrounded by other water molecules. For this reason, the direct contact with the host molecules can be restricted. From this point of view, the interaction can be key to the ionic conductivity. In other words, the ionic conductivity has maximizing value as the active sites on the graphene sheets by increasing water molecules become saturated.

However, dried GO sample had a very small amount of water molecules on GO sheets, and it had a higher interlayer spacing value (*ca.* 0.567 nm) than that of EGnP, which was mainly attributed to the lamellar structure. Therefore, it indicated that the ion conductivity by water molecules in GO was very low and it has little effect on the conductivity of GO. Furthermore, introducing functional groups between carbon layers of graphite by chemical oxidation method could make Van der Waals bond between the carbon layers weaken, which caused the graphene layers to peel off layer by layer from graphite. As sp^2 hybrid carbon atoms in graphite are partially degraded into sp^2–sp^3 hybrid atoms, fully exfoliated graphene oxide possesses less π–π stacking stability and poor conductivity.

The Raman spectra of EGnP and pristine graphite are shown in Figure 58. Raman analysis was recorded using 514-nm Ar-based laser excitation. Compared
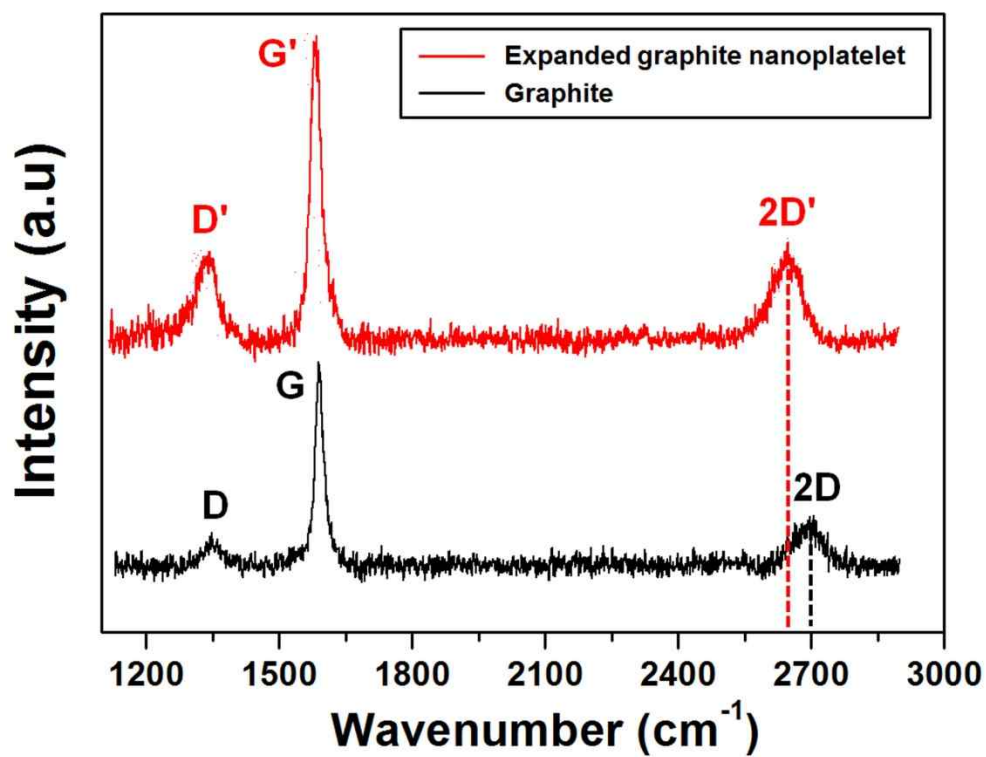
Figure 58. Raman spectra of pristine graphite and EGnP showing the D, G and 2D peaks. For Raman sample preparation, a synthesized EGnP-based aqueous solution was deposited on a Si wafer by drop casting.

to pristine graphite, the D-band of EGnP was slightly shifted to lower wave numbers, *ca.* 12.43 cm^{-1}, and the position of the G band was shifted 5.60 cm^{-1} lower. The downshift of the D and G bands may be attributable to the reduction of the vibration energy resulting from the van der Waals forces between graphene sheets, which are affected by the hydrophilic property of EGnP. The structural change from pristine graphite to EGnP was investigated with respect to the intensity ratio of I_D/I_G; this ratio is inversely proportional to the size of the crystalline grains. To evaluate the crystalline domain size the Tuinstra–Koenig equation was used as follows [147,148]:

$$\frac{I_D}{I_G} = \frac{C(\lambda')}{L_d}, where \ \ C(\lambda') = (2.4 \times 10^{-10} \ nm^{-3}) \times \lambda'^4$$

where L_d is the crystalline domain size and λ' is the Raman excitation wavelength. The crystalline domain size of EGnP was estimated to be *ca.* 27.31 nm, which was lower than that of pristine graphite (99.17 nm). The increase in I_D/I_G was due to the relative high defect concentration in EGnP from intercalation and expansion. In addition, a 2D peak position (near 2,726 cm^{-1}) was clearly evident. Hydroxylation of EGnP and the resulting repulsive interaction between OH$^-$ groups could produce the partial expansion as observed by the 60.03 cm^{-1} downshift of the 2D peak. Moreover, EGnP had a sharper, high-intensity 2D peak compared to pristine graphite, suggesting the formation of the multi-layered graphene-sheet structure of EGnP.

Synthesized EGnP could be used as conducting ink in screen printing due to its hydrophilic property, allowing its application for patterned line-heater production. The procedure for the formation of EGnP line patterns on a flexible substrate by screen printing and the schematic structure of an EGnP-based line-heater is illustrated in Figure 59 The PI film was used as the flexible substrate to prevent film deformation at high temperatures (> 140 °C). To form well-defined, precisely controlled patterns, the surface tension of the ink for screen printing should match the surface energy of the flexible substrate. The surface tension of the EGnP ink was measured to be *ca.* 65.12 mN m^{-1} by the Owens–Wendt equation, which was lower than that of distilled water (72.75 mN m^{-1}). For this reason, the PI film was treated with oxygen plasma, which caused the substrate's surface energy to increase from 44.50 to 63.87 mN m^{-1}, enhancing the wettability of the EGnP aqueous solution with respect to the substrate. The attached mask on the PI film formed an open mesh area, which allowed the EGnP ink to form a sharp-edged image as it transferred to the substrate. In this experiment, EGnP-based 5-lined patterns, 100 mm in length and 2.5 mm in width, were formed on the PI film. To reduce heat loss, the PI substrates were arranged in a "closed" configuration to provide a thermal barrier to atmospheric conditions. Copper tape was used to lower the contact resistance to the power source and to maintain the controlled output voltage.

Figure 59. a) Fabrication of patterned EGnP on a PI film using screen printing and side-view schematic of the EGnP-based line heater with a Cu electrode pair. b) The top-view of the fabrication schematic. The molar concentration of KPS for synthesis of EGnP was 150 mM, and the weight ratio of EGnP ink dispersed in an aqueous solution was 30 wt%. For the reduction of heat loss at high temperatures (> 140°C), the EGnP films were located within "closed" PI substrates and copper tape was used to lower the contact resistance to the DC power supply. The synthesized EGnP-based lines had a width of 2.5 mm and a length of 100 mm.

138

The fine tuning of the surface sheet resistance, as a function of the EGnP-based line thickness, was readily accomplished by controlling the number of screen printings, as shown in Figure 60. The thickness increased with increasing print number, whereas the surface resistance gradually decreased. The minimum surface resistance was obtained for a 70 μm line thickness; the value was estimated to be *ca.* 1 Ω sq^{-1}. From the data, one can infer that the surface resistance of the EGnP-based films decreased by a factor of 2 when compared to that of patterned graphene-based thin films by inkjet printing. Hence, the screen printing method appeared to be more effective in flexible electronic applications using graphene compared to inkjet printing [149,150].

On the basis of the above analysis, we demonstrated for the first time that EGnP-based line patterns, 70 μm in thickness, can be produced for possible electrothermal and patch line-heater applications. The voltage was applied to the EGnP-based line heater using a DC power supply and the electrical current flowing through the heaters was monitored. Figure 61 shows the temperature history of the EGnP line heater as a function of time. An input voltage of 12 V was supplied to the EGnP-based line heater. The line temperature increased rapidly until a steady-state temperature was reached, resulting in the uniform heat distribution of five EGnP-based line heaters.
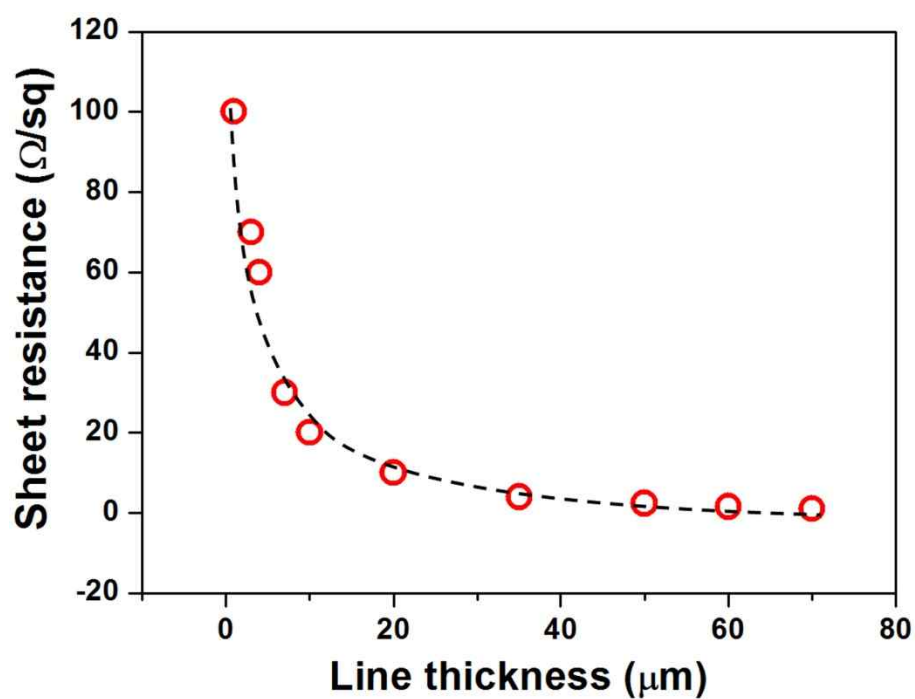
Figure 60. Surface sheet resistances of EGnP-based line with different thicknesses produced by screen printing. The concentration of EGnP in the water solution for screen printing ink was 30 wt%. Different film thicknesses were obtained by controlling the number of prints.
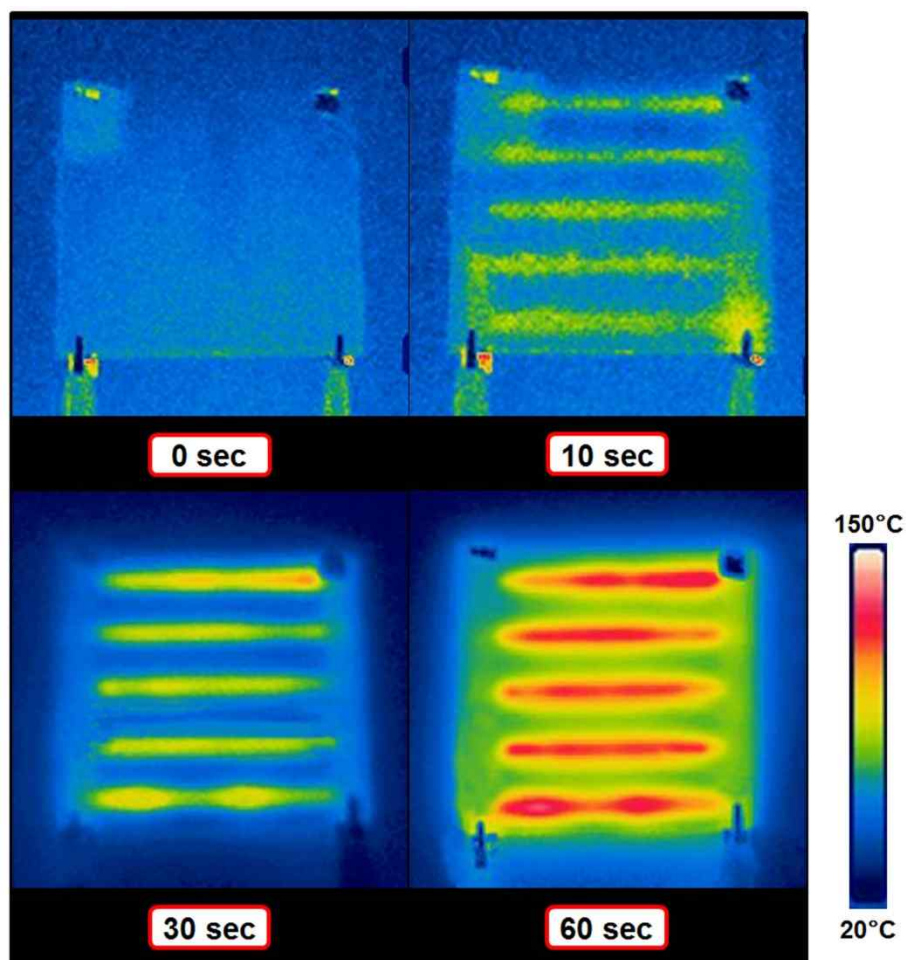
Figure 61. Temperature history of the EGnP-based line heater while applying an input voltage of 12 V. The temperature distribution on the PI substrate was measured continuously by an infrared thermal imager.

Fine tuning of the steady-state temperature was achieved by controlling the applied voltage (Figure 62a). As a result, the steady-state temperature was reached in 120 s and increased as the applied voltage increased. The EGnP-based line heater had a high steady-state temperature of 172.3 °C at a driving voltage of 14 V; the line temperature decreased to 39.8 °C in 80 s after the applied voltage was removed. Time-dependent temperature profiles revealed that the line temperature increased to 80.1, 118.5 and 133.4 °C for applied voltages of 10, 12 and 14 V, respectively, within a time frame of 60 s. The EGnP-based line heater demonstrated efficient heat propagation with uniform temperature distribution. The steady-state temperature and power consumption of the EGnP-based line heater had a linear relationship, as shown in Figure 62b. The insert table shows that the voltage and current of the EGnP-based line heater, for a given applied voltage, varied only slightly. The line temperature increased with heating time. This result suggests that the EGnP-based line heater has a steady resistance of *ca.* 28.5 Ω over a line distance of 10 cm. To compare the heater performance between EGnP and graphene-based heaters, a rectangular form (4 × 4 cm) of the EGnP-based heater was prepared by the screen-printing method (Figure 63). For an applied voltage of 3 V, the surface temperature of the EGnP-based heater reached 94°C within 60 s. The heater performance was similar to that of graphene-based heaters, without expensive
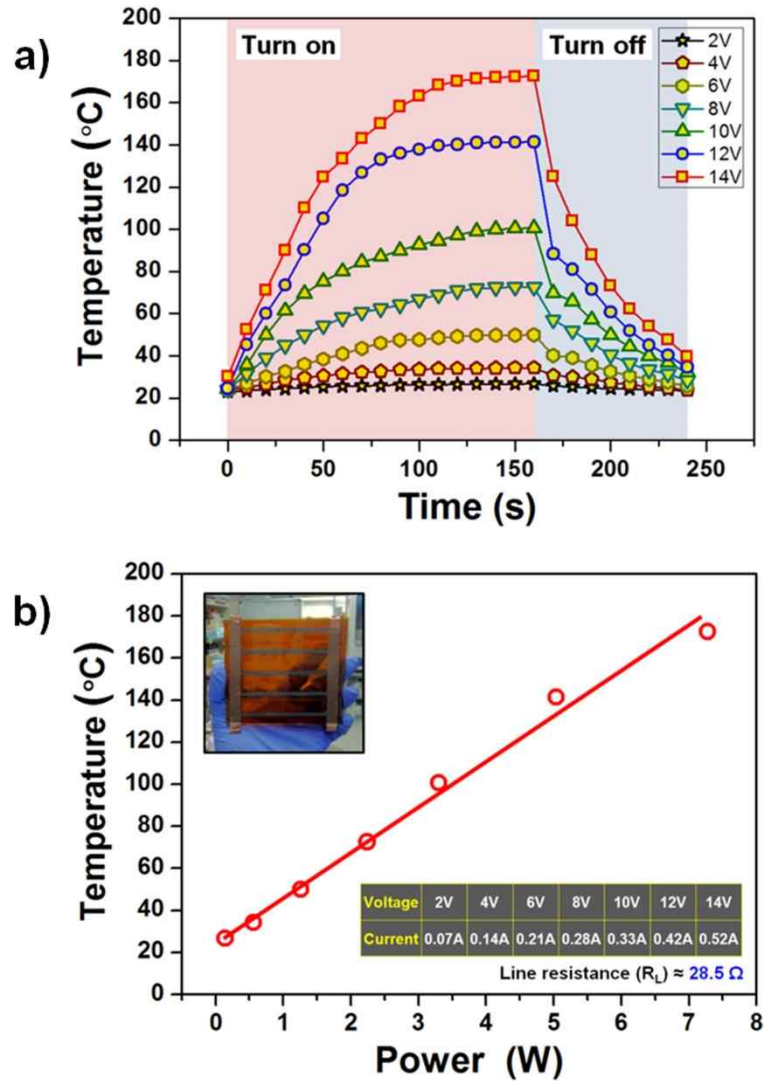
Figure 62. a) Temperature profiles of EGnP-based line heaters for different applied DC voltages. b) Temperature as a function of power consumption for EGnP-based line heaters. The inset table indicates the relationship between the applied voltage and current to the EGnP-based line heater. Using a digital multimeter, the average resistance over the 10 cm line length was *ca.* 28.5 Ω.
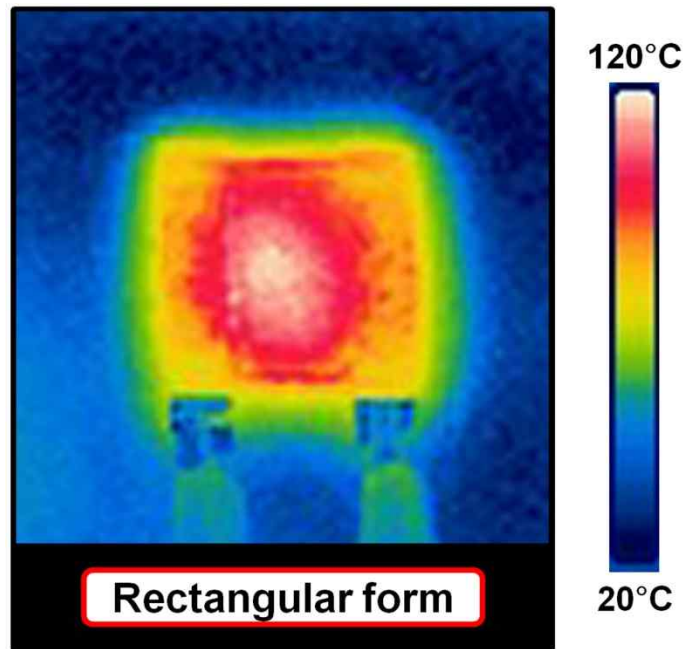
Figure 63. The infrared thermal images of EGnP-based heater while applying an input voltage of 3 V in 60 s. The size of rectangular heater was 4 × 4 cm.

dopant materials. From these result, EGnP-based heaters may be able to reduce energy consumption by up to *ca.* 37 % in comparison to graphene-based heaters [151,152]. The data further suggest that synthesized EGnP-based heaters can transfer large amounts of thermal energy to the surrounding environment without absorbing energy from the heater itself. When we used exfoliated GO and reduced GO for screen printing ink, they had very low heat performance compared to EGnP-based line heater due to their low conductivity, which direct related to the heat performance, originated from the low concentration in aqueous solution.

To elucidate the heat performance of EGnP-based heaters under bending conditions, experimental results from changing the bending radius by mechanical strength were obtained. Note that the temperature distribution of the EGnP-based line heaters was rather homogeneous under bending conditions as well as flat conditions for an applied voltage of 12 V, as shown in Figure 64a. Moreover, the temperature was inversely proportional to the resistance over a line distance of 10 cm (Figure 64b); specifically, the line resistance decreased gradually until the bending radius reached 4 cm, whereas the temperature increased. In particular, the EGnP-based line heaters under a bending radius of 4 cm had a 25 °C higher temperature with 15.1 Ω of line resistance as compared with heaters under flat conditions. The EGnP-based
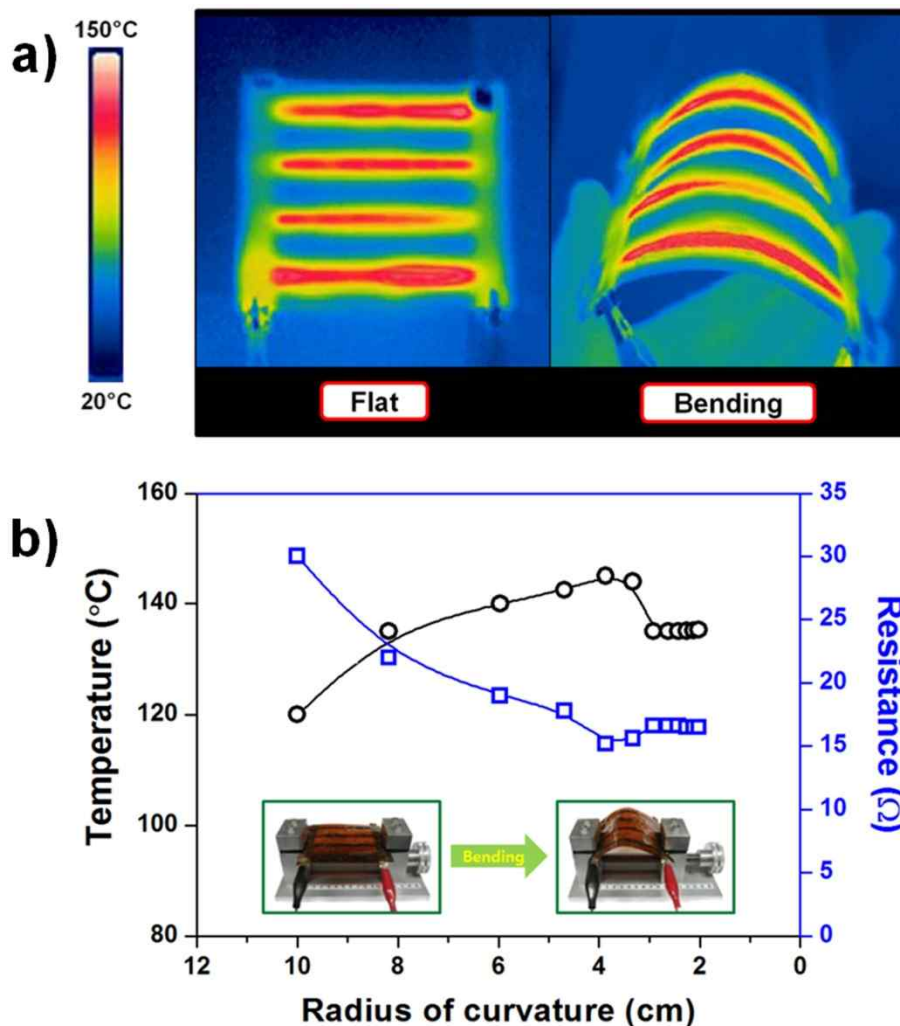
145

Figure 64. a) Infrared image of an EGnP-based heater under flat and bending conditions (radius of curvature: 4 cm). b) The temperature value and resistance of EGnP-based line heaters for a line distance of 10 cm with respect to the bending radius. For the bending test, EGnP-based 4-lines were used with heater and temperature values measured 60 s after applying the 12 V input voltage.

heater also exhibited identical heat performance after 6 months of use. These results suggest that the high performance of EGnP-based line heaters can be attributed to, not only the excellent thermal and electrical conductivity of this material, but also to the highly uniform surface of EGnP films to flexible substrates. The shape and size of the EGnP-based line heaters are easily manipulated using screen printing, thus suggesting the use of this technique in large-scale production of patchable heaters for industrial applications.

The outstanding electrothermal properties of the EGnP-based line heater was applied to the boiling of water. In this experiment, 500 mL of distilled water was placed in a beaker. A thermometer monitored the water temperature. The water boiling test was carried out under ambient conditions. Figure 65 shows that the water temperature increased from 20.1 to 90.2 °C in 30 min under an applied voltage of 14 V. This result implies that the EGnP-based line heater is feasible for practical applications, such as hot plates used for food preparation, window defrosters for the back and side windows of vehicles, and heating pads for warming the body.
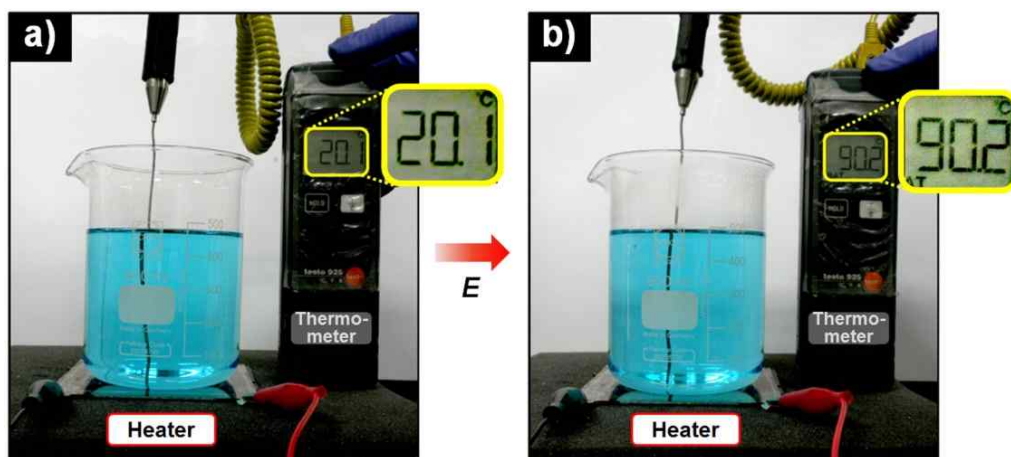
Figure 65. Water heating results a) before and b) after operation of the EGnP-based line heater under an applied voltage of 14 V. The volume of the water used for the boiling test was 500 mL and the time required to raise the water temperature (*ca.* 90.2 °C) was 30 min.

3.4. Graphene/Polyaniline Thin Films via Screen Printing and Their Applications

3.4.1. Graphene/polyaniline/poly(4-styrenesulfonate) hybrid film with uniform surface resistance and its flexible dipole tag-antenna application

Graphene was fabricated by graphite intercalation and exfoliation using an oxidizing agent and microwave radiation without additional reduction processes [153,154]. A multilayer graphene structure with particle diameters of 1–10 μm and thickness of 4–8 nm was formed after intercalation and exfoliation of densely layered pristine graphite. Evidence of this structure is provided by SEM, TEM, AFM and Raman spectra (inset) in Figures 66. PSS was fabricated by radical polymerization and was added to a well-dispersed PANI aqueous solution synthesized by chemical oxidation polymerization because *in-situ* polymerization restricts the availability of PSS [155,156].

As a result of this processing technique, G/PANI/PSS-based conducting pastes could be obtained by simple mechanical mixing of the synthesized multilayer graphene with the PANI/PSS aqueous solution. Figures 67a shows that PANI/PSS was homogeneously coated onto the entire surface of the graphene. To confirm the beneficial effects of PSS injection on the graphene/polymer hybrid in an aqueous system, a graphene/PANI mixture was
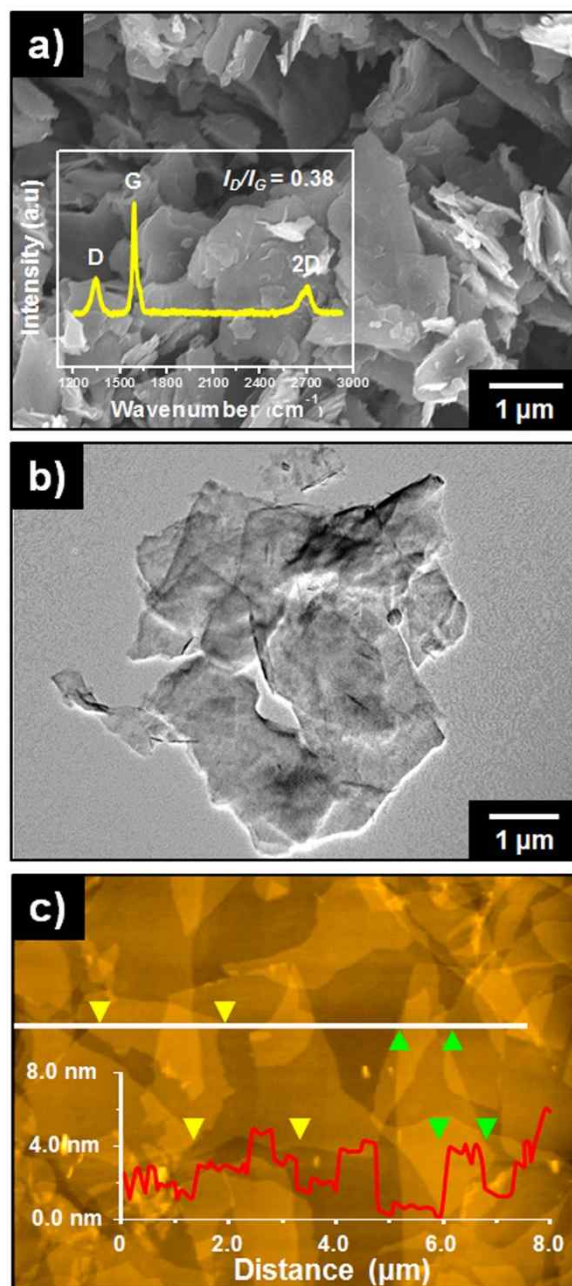
Figure 66. a) SEM, b) TEM and c) AFM images of pristine multilayer graphene, respectively. (inset: Raman spectra of multilayer graphene indicating the D, G and 2D peaks).
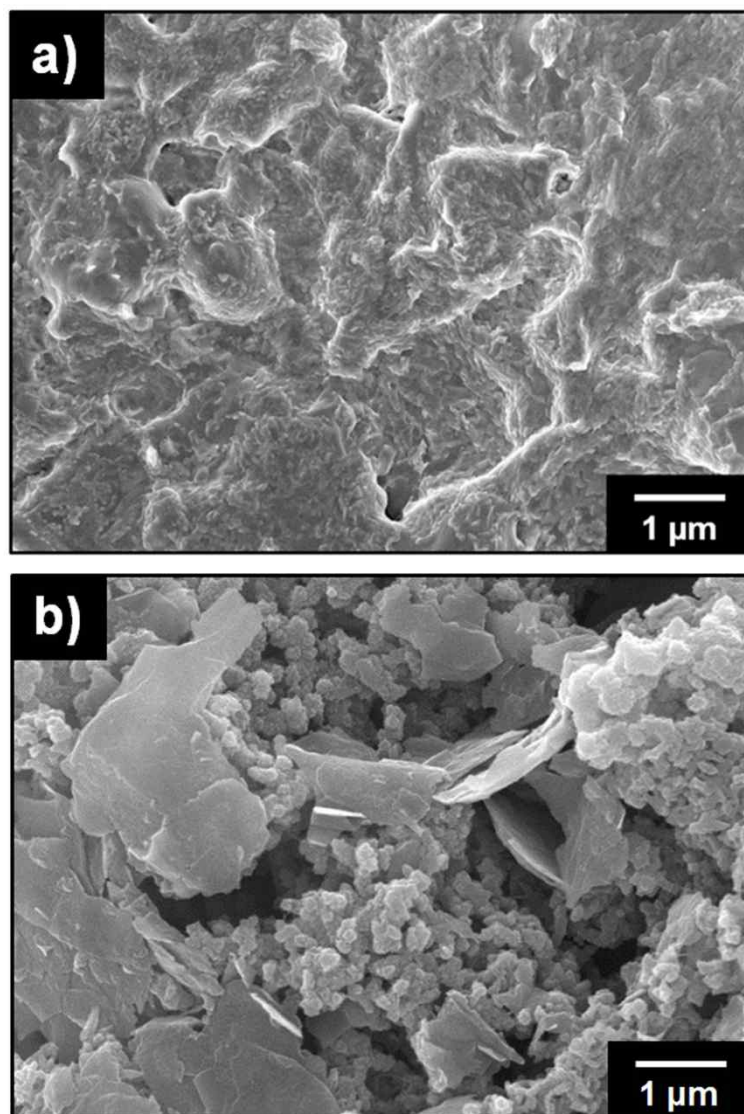
Figure 67. Representative SEM micrographs of a synthesized a) G/PANI/PSS and b) graphene/PANI hybrid films. For SEM sample preparation, 30 wt% graphene powder was mechanically blended with the PANI/PSS or PANI aqueous solution.

also prepared. In the latter system, agglomerates of PANI nanoparticles (200–300 nm) were formed independent of the graphene layers (Figure 67b). Thus, it is clear that PSS plays a key role in dispersing the hydrophobic graphene throughout the aqueous system by enhancing interfacial interactions and mechanical interlocking between the multilayer graphene matrix and the PANI nanoparticles.

FTIR spectra indicate that the as-prepared hybrid films consisted of G/PANI/PSS and PANI/PSS (Figure 68). The peaks at 1122 cm^{-1} and 1010 cm^{-1} in the FTIR spectrum of PANI/PSS are attributed to in-plane skeletal and bending vibrations of the benzene ring, respectively. The peak at 810 cm^{-1} originates from an out-of plane C–H bending on the para-disubstituted phenyl group. The stretching vibrations of the C=C quinonoid ring appear at 1122 cm^{-1} and 1598 cm^{-1}. Furthermore, the peaks at 1495 cm^{-1}, 1422 cm^{-1} and 1299 cm^{-1} are ascribed to stretching of the C=C benzenoid ring and stretching of the C–N bond, respectively. In general, the intensity ratio of the two peaks at 1598 cm^{-1} and 1495 cm^{-1} (I_{1598}/I_{1495}) is related to the protonation state of PANI. In the current experiment, the I_{1598}/I_{1495} ratio was *ca.* 0.76, which indicated that PANI nanoparticles were successfully formed as emeraldine salt (ES) state [157,158]. The presence of PSS was indicated by the peak at 1150 cm^{-1}, which is caused by the asymmetric stretching of the SO_3^- group, and the peak at 1035
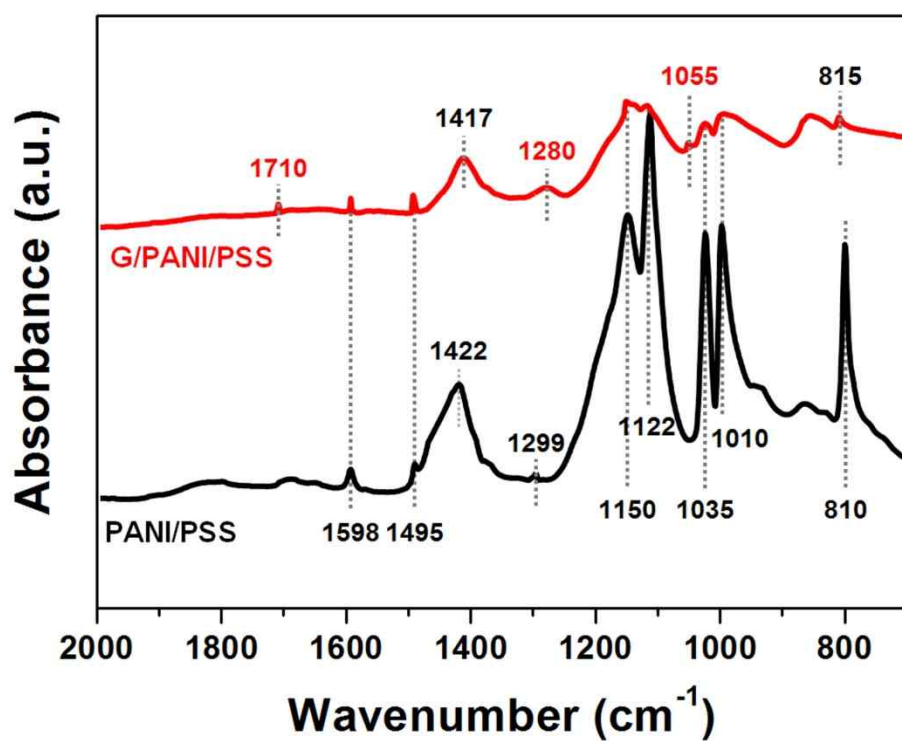
Figure 68. FTIR spectra of PANI/PSS and G/PANI/PSS. Powdered samples were used for FTIR analysis.

cm^{-1}, which is attributed to symmetric stretching of the sulfonic group.

The FTIR spectrum of G/PANI/PSS contains a C=O stretching vibration corresponding to a carboxyl at 1710 cm^{-1} and a C–O vibration at 1055 cm^{-1}. In addition, C–C skeletal vibrations from unoxidized graphitic domains are evidenced by a peak at 1598 cm^{-1}, and stretching of the C=C bonds in the aromatic ring produced a peak at 1495 cm^{-1}. The broad peak at 1280 cm^{-1} originates from a C–O–C stretching vibration. The characteristic peaks of PANI/PSS are also evident, which demonstrates the successful introduction of PANI/PSS nanofiller into the graphene matrix.

To find the optimal conditions for screen printing the G/PANI/PSS hybrid film for flexible electronics applications, the weight content of graphene was carefully controlled. In the PANI/PSS-based screen-printing conducting inks, the weight fractions of PANI and PSS in G/PANI/PSS were assumed to be *ca.* 7 wt% and 10 wt%, respectively. The surface resistance as a function of graphene weight ratio is displayed in Figure 69a. The G/PANI/PSS films had a low surface resistance of 5 Ω sq^{-1} with 30 wt% graphene. This is 20 times lower than the surface resistance of PANI/PSS and is similar to the resistance of a pristine graphene-based film, suggesting a bridging effect between adjacent graphene layers along the horizontal and vertical axes. However, as the concentration of graphene increased to over the 30 wt%, the conductivity of
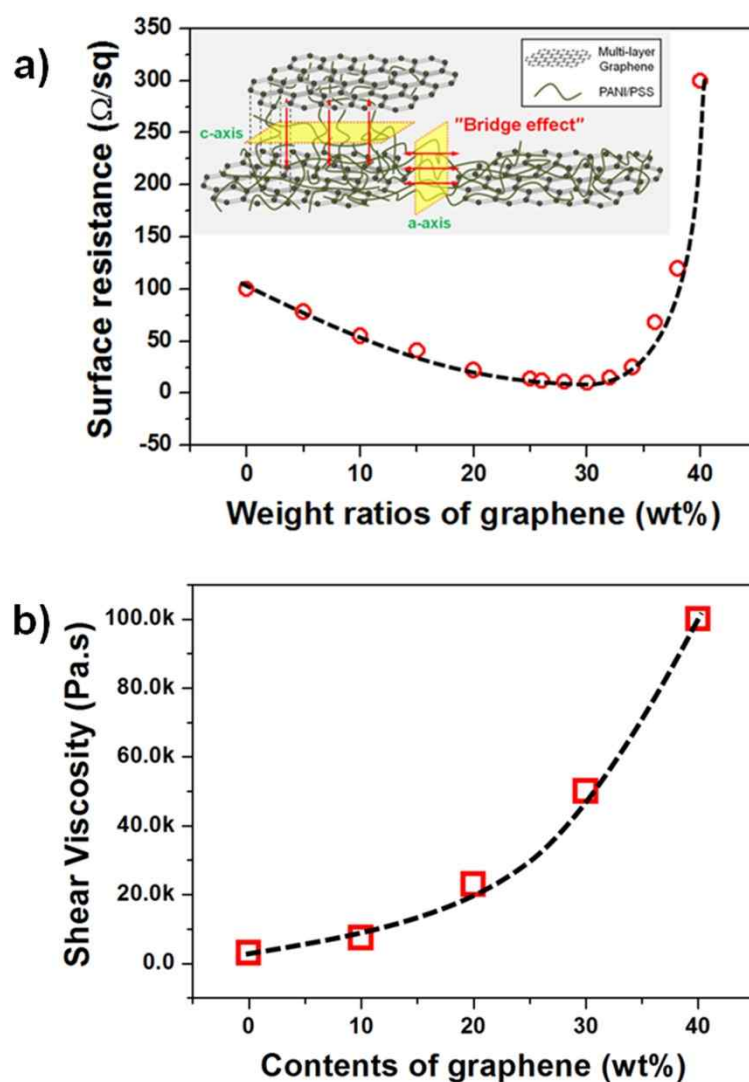
Figure 69. a) Surface resistance of the G/PANI/PSS hybrid film as a function of the graphene concentration. The inset scheme indicates the "bridge effect" of the PANI/PSS in the graphene interlayer. b) Shear viscosity of the G/PANI/PSS-based conducting ink according to the graphene content. The shear rate to measure viscosity was 0.1 s^{-1}.

155

G/PANI/PSS rapidly decreased. At these higher graphene concentrations, low dispersibility due to high viscosity resulted in interfacial defects that hindered electron transport (Figure 69b).

Fine tuning of the surface sheet resistance can be accomplished by controlling the number of screen printings, which adjusts the overall thickness of the G/PANI/PSS hybrid film, as shown in Figure 70a. Hardening of the film surface using resin and curing agent was performed prior to optically measuring film thickness. Additional printing steps increased the hybrid film thickness up to 70 μm with a gradual decrease in surface resistance to a minimum of *ca.* 10 Ω sq^{-1}. The cross-sectional optical image in the inset of Figure 2b shows that the screen-printed film was uniform in thickness. Mechanical delamination from the substrate limited the thickness of the G/PANI/PSS hybrid film equal to 70 μm.

The surface resistance distribution of the G/PANI/PSS hybrid film was compared to that of a graphene-based film at an average fixed thickness of *ca.* 70 μm for both films. A 5-cm square pattern was formed by screen printing using terpineol and butyl cellosolve as organic solvents for the graphene-based film. Figure 70b shows that the synthesized G/PANI/PSS had good interplanar electrical contact between the graphene layer over about 8% of the surface, compared to a 23% distribution for the graphene-based film. These results
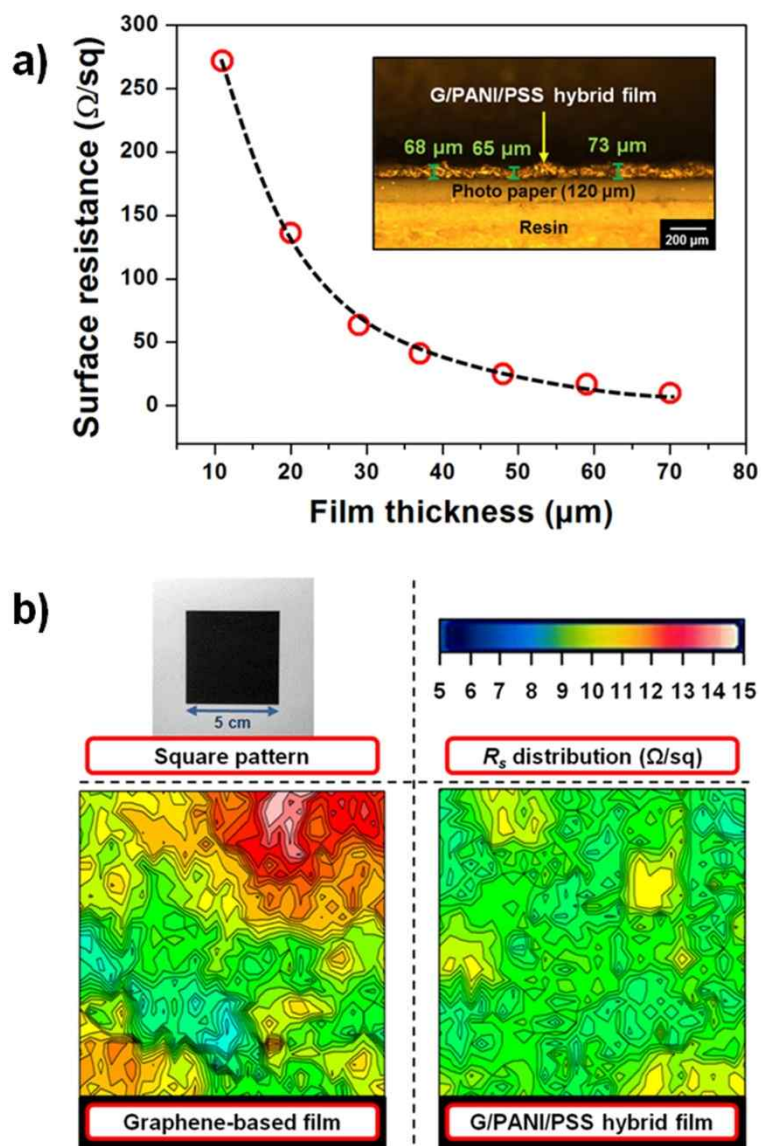
Figure 70. a) Surface resistance of the G/PANI/PSS hybrid film as a function of the film thickness. The photo shows a homogenous film thickness of 70 μm. b) The distribution of surface resistance for the graphene-based and G/PANI/PSS hybrid films for a 5-cm square pattern.

157

suggest that PSS acted as a bridge connecting graphene with PANI and that PANI/PSS enhanced the interfacial interactions between graphene layers. In other words, the contact resistance, which originates from considerable defect regions in the graphene nanosheets formed by exfoliation, was reduced. The vacant lattice sites in the graphene were then filled with well-dispersed PANI nanoparticles.

To assess the flexibility of the G/PANI/PSS hybrid film, electrical fatigue tests were performed using an external force. Overall surface resistance increased in proportion to the folding angle from −180° to +180°. Folding the film −180 ° and +180 ° led to *ca.* 10 % and 21 % increases in surface resistance, respectively (Figure 71a). However, surface resistance decreased by up to 6 % as a function of increasing folding angle from 0 to −30 °. These results can be explained in terms of compressive and tensile strain. Namely, graphene nanosheets exhibit a high degree of overlap in $\pi-\pi$ stacking under compressive strain (−30° < folding angle < 0°), which causes extensive charge delocalization. This phenomenon disappears with increasing tensile strain (−180° < folding angle < −30°) and is replaced with mechanical deformation of the stacked graphene, which reduces charge-carrier mobility. Tensile strain of G/PANI/PSS hybrid film (0° < folding angle < +180°) results in a considerable decrease in conductivity caused by the introduction of extended defects into the graphene lattice.
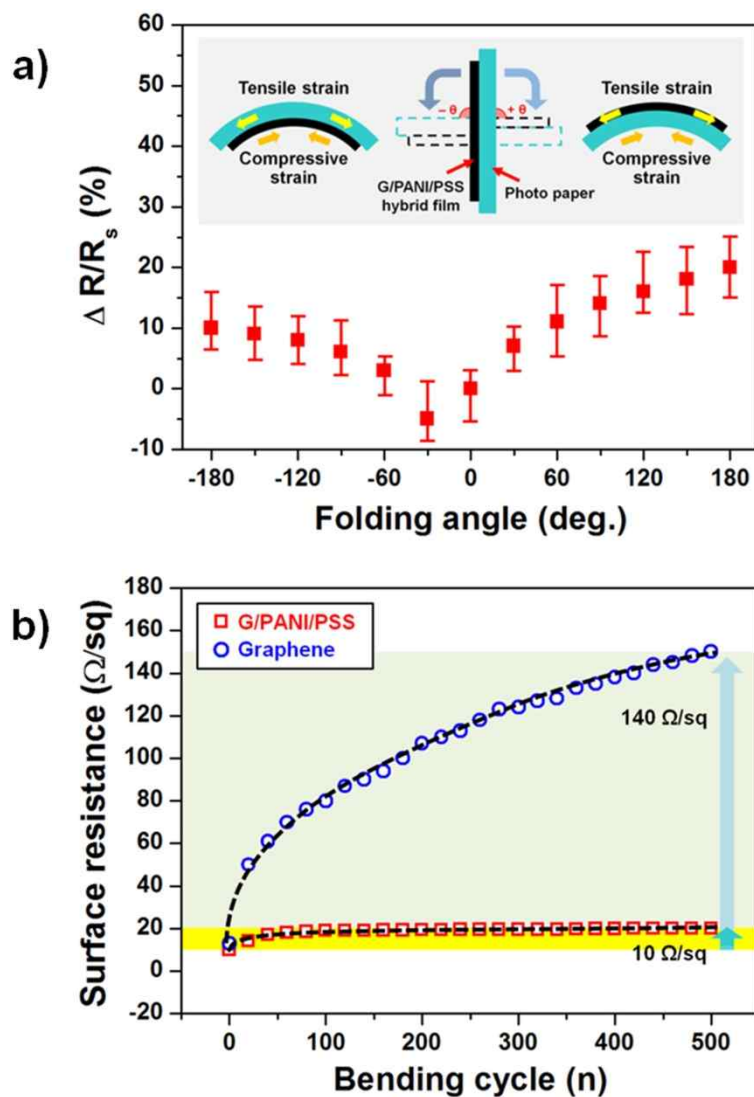
Figure 71. Surface resistance changes of a G/PANI/PSS hybrid film as a function of a) folding angle and b) bending cycle (inset: schematic diagram of folded G/PANI/PSS film on substrate under tensile or compressive strain, θ > 0). A comparative study with the graphene-based film as a function of bending cycle is also presented.

159

Figure 71b shows the surface resistance of the G/PANI/PSS hybrid film and a graphene-based film as a function of bending cycle. When the samples were released from bending after 500 cycles, the surface resistance of the hybrid and graphene-based films increased by only *ca.* 10 and 140 Ω sq^{-1}, respectively. This indicates a high degree of structural stability in the G/PANI/PSS hybrid film. This is most likely the result of improved adhesion of the hybrid film to the flexible substrate, which can in turn be ascribed to the high concentration, viscosity, and molecular weight of the PSS binder. In contrast, the graphene-based film exhibited cracks and fissures after bending. The above results indicate that these G/PANI/PSS hybrid films may be applicable as electrodes in tag antennas.

The G/PANI/PSS-based conducting paste was screen-printed into a micropattern and assessed as an antenna for dipole tag applications. The procedure for the formation of G/PANI/PSS-based patterns on a flexible substrate by screen printing, along with optical images and a schematic representation of the ring pattern, is illustrated in Figure 72a. Ring patterns with a 5.5-mm internal diameter and 7-mm outer diameter were formed on photo paper. Flip-chip bonding locations are specified along sections A and B. To further define the pattern resolution, the screen-printed G/PANI/PSS-based patterns were compared along sections A′ and B′ at high magnification with the
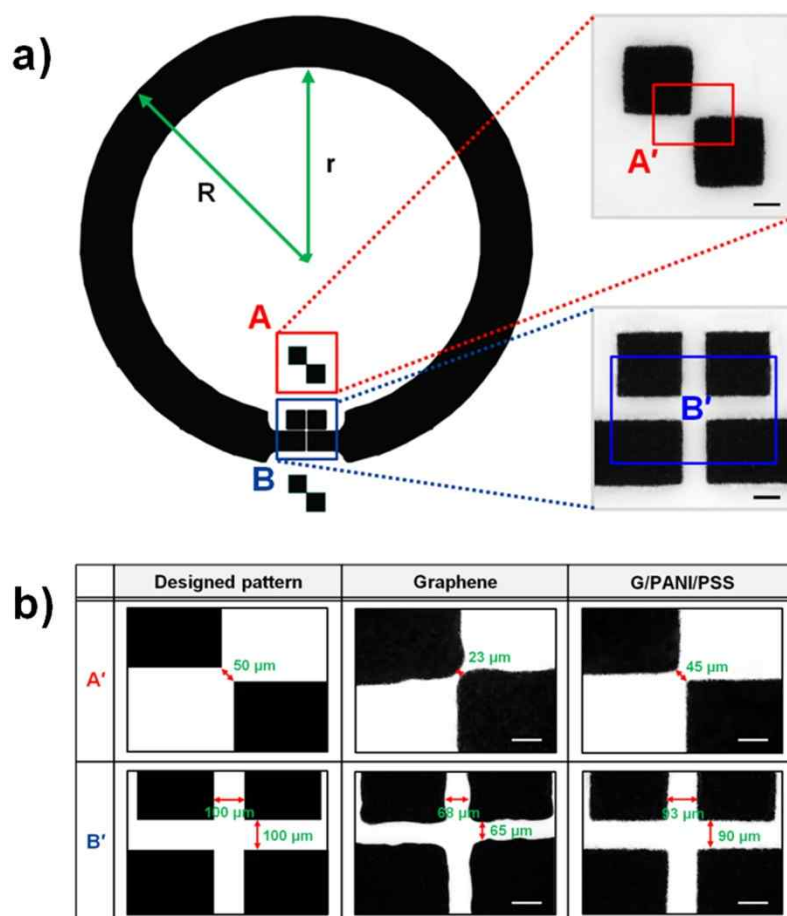
Figure 72. a) The designed ring pattern for the dipole tag antenna and optical images of section A and B formed by the G/PANI/PSS-based conducting paste. The distances along the diagonal direction for the A section and horizontal direction for the B section were 50 µm and 100 µm (r = 5.5 mm, R = 7 mm), respectively. b) Optical images show pristine graphene and the screen-printed G/PANI/PSS-based pattern for the A′ and B′ sections. The optical images are magnified at the marked areas (scale bar: 100 µm). c) A schematic mechanism illustrates the observed differences in edge waviness between the pristine graphene and the G/PANI/PSS hybrid film.

initial design and graphene-based patterns using optical methods. Figure 72b shows that G/PANI/ PSS patterns were obtained with higher resolution than those of pristine graphene. This difference in resolution may be attributed to surface energy matching between the substrate and the conductive ink and grain properties within the domain structure. The surface tension of the graphene-based ink was measured as *ca.* 46.12 mN m^{-1}, which is lower than that of photo paper (68.73 mN m^{-1}). In contrast, the G/PANI/PSS-based aqueous solution had a high surface tension of 73.14 mN m^{-1}, which afforded excellent compatibility with respect to the substrate. Furthermore, despite high concentration of graphene, good wettability of G/PANI/PSS-based thin films could be maintained due to their hydrophilic property (Figure 73). The attached mask on the photo paper formed an open mesh area, which allowed the hybrid ink to form a sharp image without line-edge waves as it transferred to the substrate (Figure 74). Moreover, stacks of planar graphene structures surrounded by PANI/PSS over large domains have affected the high-resolution patterns.

A synthesized G/PANI/PSS-based ring pattern was connected to an RF network analyzer using an SMA-type connector for dipole tag antenna tests. Generally, bandwidth and VSWR or RL, which is indicative of transmitted power efficiency, are used to evaluate the performance of a designed antenna. The G/PANI/PSS-based dipole tag antenna had a 28.7-MHz bandwidth from
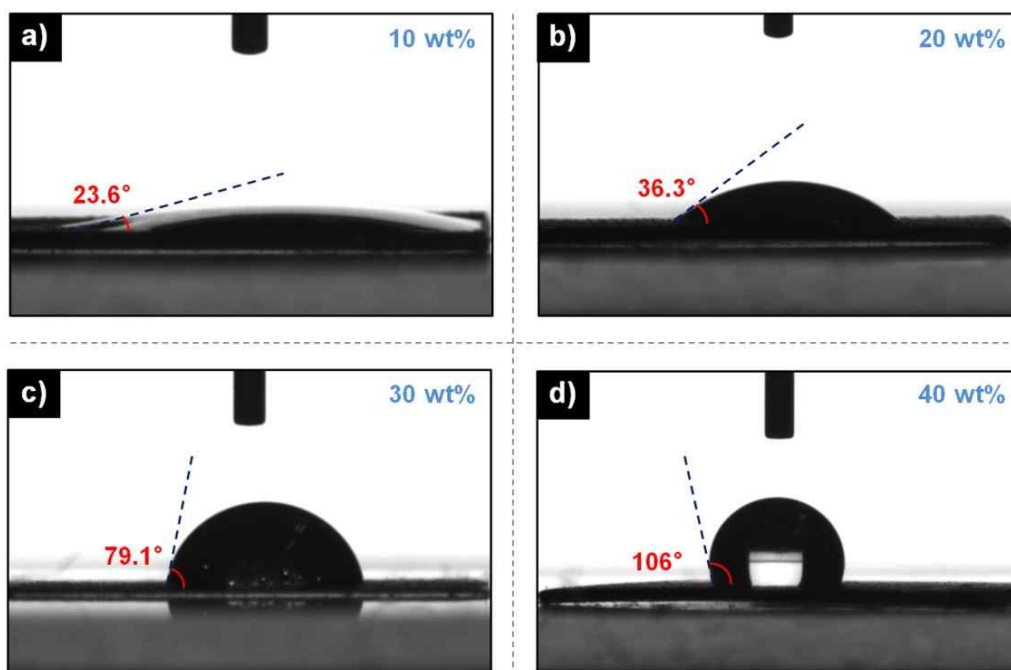
Figure 73. Contact angles on the surface of G/PANI/PSS hybrid film with a) 10, b) 20, c) 30 and d) 40 wt% graphene. All samples were transferred onto a flexible PET film.
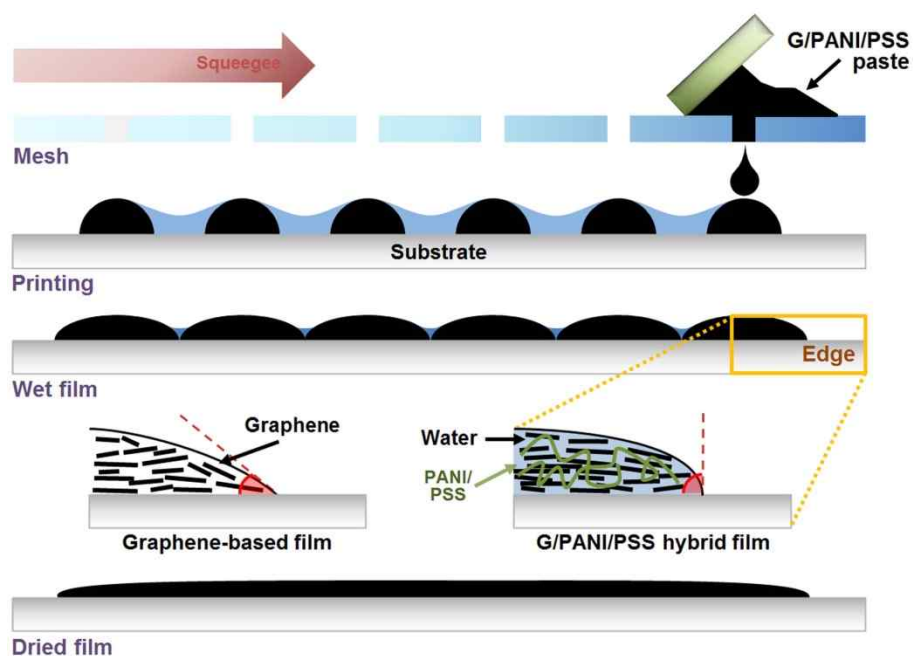
Figure 74. A schematic mechanism illustrates the observed differences in edge waviness between the pristine graphene and the G/PANI/PSS hybrid film.

894.4 MHz to 923.1 MHz with respect to a 10-dB standard, as shown in Figure 75a. Furthermore, a VSWR of 1.28 and an RL of 18.2 dB at the mean frequency indicated a high transmitted power efficiency of 98.5 % (Table 4). The inset shows that the impedance point of the passband was located near the center of the Smith chart, which indicates a small RL. Figure 75b shows that the recognition distance of the G/PANI/PSS and graphene-based dipole tag antennas increased slightly with frequency. In particular, the G/PANI/PSS-based dipole tag antenna could be detected within 0.42 m at 910 MHz, which was twice the recognition distance of the graphene-based dipole tag antenna.
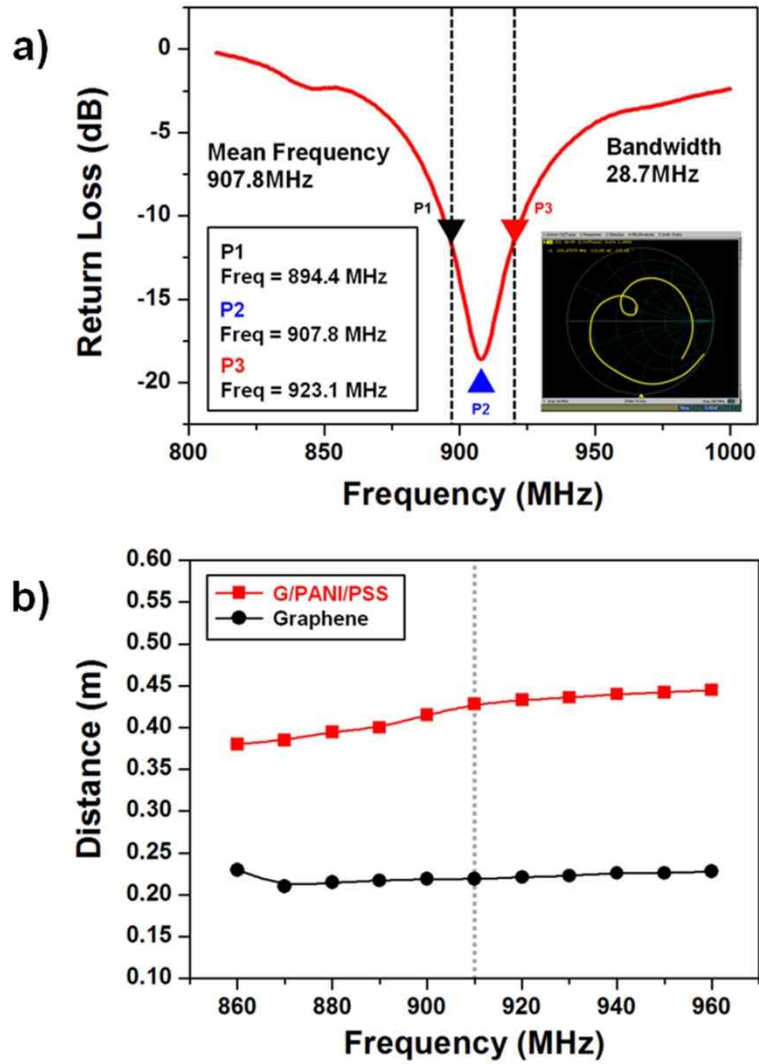
Figure 75. a) The return loss curve of the dipole tag antenna using a G/PANI/PSS-based electrode (inset: Smith chart impedance diagram). b) Recognition distances of graphene and the G/PANI/PSS-based dipole tag antenna as a function of frequency.

Table 4. VSWR and RL of patterned G/PANI/PSS-based dipole tag antenna.

VSWR	RL[a]	Reflection Coefficeint (Γ)	Transmitted Power	Reflected Power
1.28	18.2	0.066	98.5	1.5

[a] This value was acquired in the E5071B ENA RF Network Analyzer of Agilent Technologies.

3.4.2. Fabrication of highly scalable graphene/polyaniline thin film with enhanced electrical and mechanical property and its monopole antenna application.

Figure 76 shows a schematic illustration of the synthetic procedure of G/PANI thin film. First, the graphene powder was added to HCl solution and sonicated for 24 hr to obtain homogeneous dispersion. Then aniline monomer was added, keeping vigorous stirring. In this experiment, chloroform was mixed to prevent the freezing of the reaction solution. When the temperature of the solution decreased to -9 $^{\circ}$C in the chiller, the anilinium hydrochloride became partially insoluble in the aqueous phase and co-existed in both the aqueous and organic phase [159]. Thus, the hydrophobic part of the anilinium hydrochloride (phenyl group) adsorbed on the aromatic surface of the graphene by the π–π interaction in the organic phase [160]. After addition of initiator, APS, the polymerization of aniline occurred on the surface of the graphene, and then graphene/PANI ES was obtained. After washing and drying, the primary dopant of PANI ES in G/PANI was removed by ammonia solution, resulting in de-doped G/PANI (De-G/PANI). After additional washing and drying, De-G/PANI was re-doped by CSA, and then re-doped G/PANI (Re-G/PANI) was dissolved in m-cresol/chloroform solvent. This secondary doping process is very helpful in changing the conformation of PANI chains from a
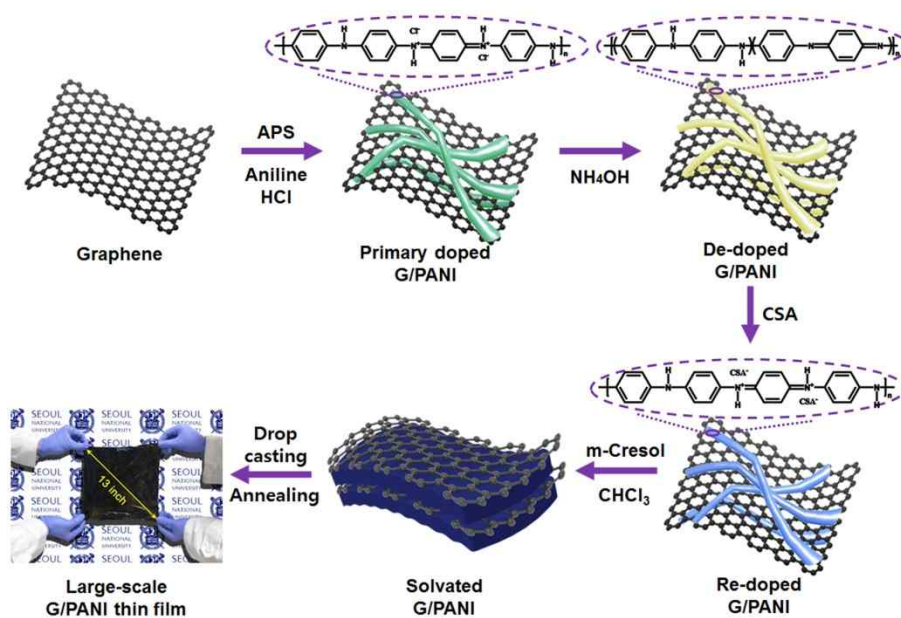
Figure 76. Schematic illustration of the sequential steps for fabricating large-scale G/PANI thin film.

compact coil to an expanded structure in the solvent [161]. Furthermore, it is expected that graphene also induced the more expanded coil conformation of PANI chains in the solution *via* strong π–π interactions. Finally, the prepared solution was cast onto a large-sized glass substrate (23 cm x 23 cm, 13 inch) and placed on a heat source to evaporate any residual solvent. Due to the high surface polarity and wettability of the m-cresol solvent, the prepared solution was well attached to the glass substrate [162]. After the annealing process, the large-scale G/PANI film could be obtained.

In this experiment, solvated G/PANI could be used as conducting ink in screen printing, and the smaller sized thin films (3 cm x 500 μm) of graphene, PANI and G/PANI were easily fabricated via screen printing, demonstrating the great advantage of the scalable film. The attached mask on the photo paper formed an open mesh area, which allowed the conductive ink to form a sharp-edged image as it transferred to the substrate. Figure 77 illustrates the the optical micrographs and FE−SEM images of the surface morphology for the graphene, PANI and G/PANI-based straight lines on photo paper. Pristine graphene exhibits the wrinkled and silk-like two-dimensional morphology with the size of several micrometers structure [163]. The SEM images of the PANI and G/PANI clearly show that the PANI was uniformly and successfully polymerized on the surface of the few micrometer sized-graphene. Furtheremore,
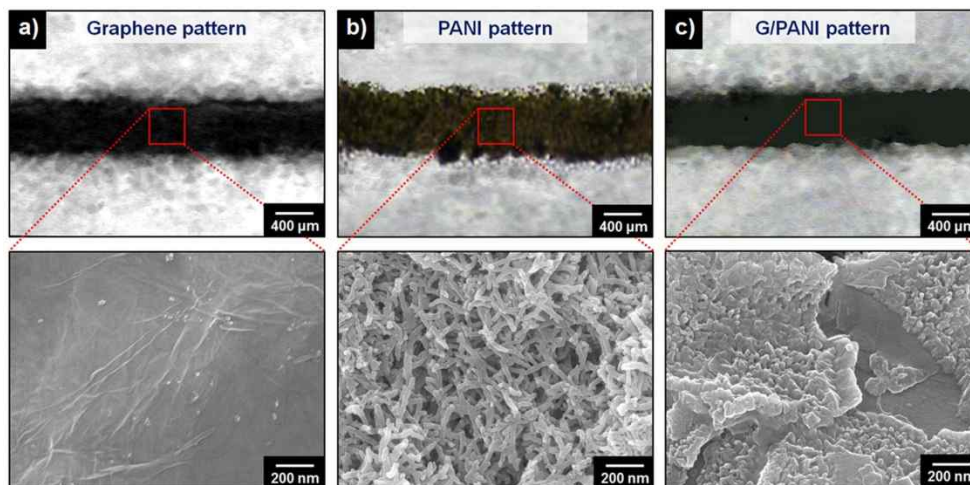
Figure 77. The optical micrographs and FE−SEM images of the surface morphology for the a) graphene, b) PANI and c) G/PANI-based straight lines with the width of *ca.* 500 µm and length of *ca.* 3 cm on photo paper. The patterning of three different conductive materials-based thin films was obtained via screen printing.

well-defined patterns of graphene and G/PANI thin film are more clearly observed on the photo paper than that of pristine PANI. This difference of resolution was related to grain property on domain structure. In other words, stacks of planar structure on the large domain caused the high resolution of patterned graphene and G/PANI.

The Raman spectra of graphene exhibit the increased I_D/I_G compared to that of GO, suggesting that the reduction process increased the defect content or edge area in graphene sheets (Figure 78). In addition to the reduction process, the decreased size of the graphene sheets might also cause the structural defect, leading to an increase of I_D/I_G. The Raman spectra of pristine PANI show the distinctive vibrations of C-C stretching of the para-distributed benzenoid ring, C=N stretching of the quinoid ring, C=N stretching of the quinoid ring, C-N$^{\bullet+}$ stretching in polaron form (cationic amine units of the benzenoid ring), C-N^{+} stretching in bipolaron form (cationic imine units of the quinoid ring), C-N stretching, C-H bending of the benzenoid ring, C-H bending of the quinoid ring, benzenoid ring deformation, and C-H bending of the quinoid ring and quinoid ring deformation at 1620, 1513, 1485, 1338, 1312, 1255, 1189, 1162, 878 and 832 cm^{-1}, respectively [164,165]. After aniline monomers were polymerized on the graphene, the intensity of quinoid ring-related vibrations has increased, and the C=C stretching vibrational mode of the quinoid ring at 1582 cm^{-1} has
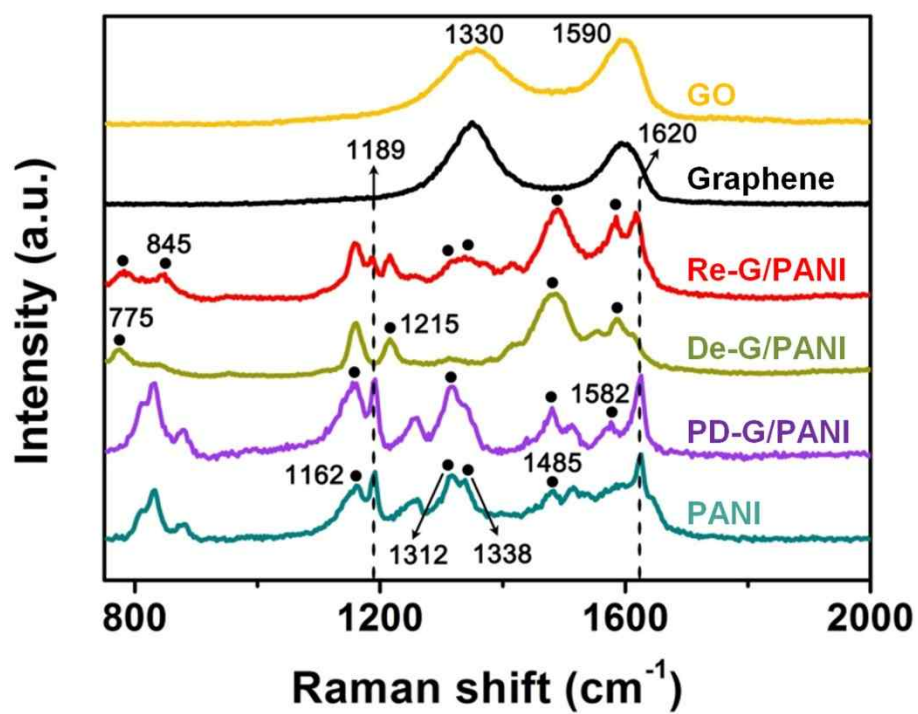
Figure 78. Raman spectra of GO, graphene, Re-G/PANI film, De-G/PANI, primary doped G/PANI and PANI.

173

appeared [166], which indicated of the strong inter-molecular π–π stacking between the basal planes of the graphene and the quinoid rings of the PANI backbone [167]. In the Raman spectra of De-G/PANI, the peaks of C-N$^{\bullet+}$ and C-N^{+} almost disappeared, whereas C-N stretching in the emeraldine base (EB) form and quinoid ring deformation at 1215 and 775 cm^{-1} newly appeared [168,169]. Furtheremore, it was observed that the C-C stretching of the para-distributed benzenoid ring significantly decreased, while the C=C stretching band of the quinoid ring and the C=N stretching vibration of the quinoid ring increased considerably, which lead to high imine/amine and quinoid ring/benzenoid ring ratio than the ES form [170,171]. Moreover, it should also be noted that PANI ES significantly losses its bipolaronic and polaronic structure by de-protonation [172,173]. After De-G/PANI was re-doped by CSA, the re-emerged benzenoid ring peak (1189 cm^{-1}), newly appeared amine deformation peak (845 cm^{-1}), and increased benzenoid ring peak (1620 cm^{-1}) obviously reflect the increased doping level of PANI in the Re-G/PANI film [174]. In addition, the re-emerged bipolaron and polaron bands provide crucial evidence of the successful re-protonation of the PANI component. The up-shift of the two quinoid ring vibrations at 782 and 1489 cm^{-1} indicated the changed backbone structures of PANI to benzenoid ring and amine nitrogen atoms. However, the quinoid ring vibrations still present even after the redoping

process, and the peak at 1582 cm^{-1} corresponding to the C=C stretching band of the quinoid ring has been slightly increased. It means that the overlapping of the P$_z$ orbitals of the quinoid rings of the PANI with the aromatic surface of graphene would result in the strong quinoid ring peaks in the Re-G/PANI film. In order to an in-depth insight into the mechanical property of synthesized G/PANI thin film, representative stress−strain curves for three different conductive thin films are presented in Figure 79. The pristine graphene and PANI thin films have an tensile strength of 224 and 208 Pa, and modulus of 7.13 and 4.33 GPa, respectively. Significant improvements on the tensile strength and modulus have been achieved for the G/PANI thin film: a tensile strength of 315 Pa and a modulus of 10.05 GPa (Table 5). Compared with pristine graphene and PANI thin films, the elongations at break become higher for the G/PANI thin film, which is about 6.31%. Most of all, the work of extension to toughness is 8.74 MJ m^{-3} for the G/PANI thin film, slightly higher than that of the pristine PANI thin film (6.93 MJ m^{-3}). Considering these results, it could be inferred that the enhanced mechanical strength of G/PANI could be orginated from the strong interactions between graphene sheets and PANI resulting from the compact inter-molecular π–π stacking.

To measure the electromechanical stability of the samples, the four-probe method was conducted. Patterned graphene, PANI and G/PANI thin films have
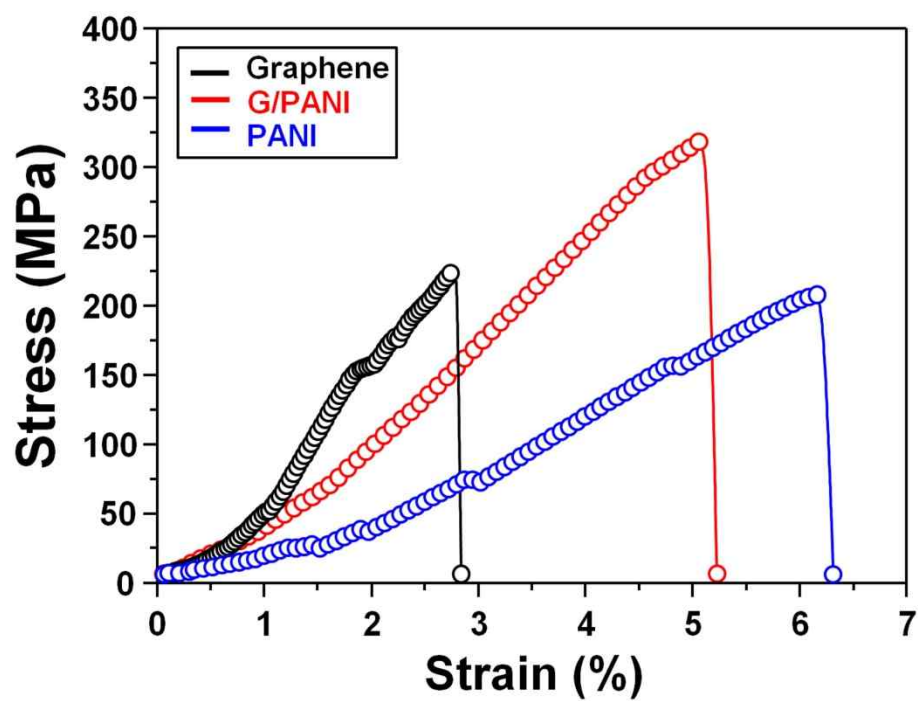
Figure 79. Typical stress-strain curves under tensile loading of graphene, PANI and G/PANI thin films. The mechanical measurement was conducted under strain rate of 1 mm s^{-1}.

Table 5. Mechanical properties of various G/PANI-based thin films.

Sample	Modulus [a] (GPa)	Tensile strength [a] (GPa)	Elongations at break [a] (%)	Toughness [a] (MJ m^{-3})
Graphene	7.13	224	2.89	3.45
PANI	4.33	208	6.31	6.93
G/PANI	10.05	315	5.20	8.74

[a] These values were obtained by stress−strain curve using UTM .

a surface resistance of 35, 2.1, and 0.6 Ω sq^{-1} at room temperature, respectively. Electrical fatigue tests were performed using an external force and Figure 80 shows the surface resistance change of the samples as a function of bending cycle. When the samples were released from bending after 500 cycles, the surface resistance change of the G/PANI, pristine PNAI and graphene thin films increased by only about 3.2, 6.7 and 8.8, respectively. This indicates a high degree of structural stability in the G/PANI thin film. In contrast, pristine graphene-based film exhibited cracks and fissures after bending. The above results indicate that patterned G/PANI thin film may be applicable as electrodes in RFID antennas.

Prior to study the patterned three types of thin film-based monopole antenna application, dielectric constant of the samples are analyzed since it affects the speed of propagation for an electromagnetic wave thorugh a material. Therefore, the permittivity and loss factor (ε'') of the samples were determined (Figure 81). As a result, the G/PANI thin film had a significantly improved permittvity value of 60.32 compared to that of pristine graphene (20.57) and PANI (41.09) thin film. It indicates the increased rate of reversible conformational rearrangements in the interior of the G/PANI, which resultant in high stored energy opposing the external electric filed. In electromagnetics, the permittivity can be strongly influenced by the geometry of the materials
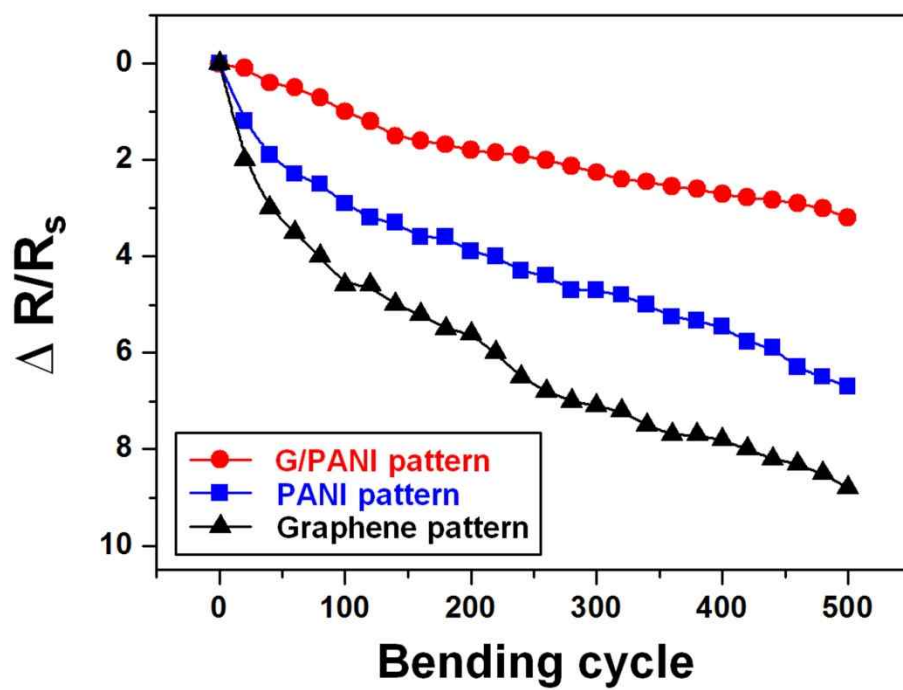
Figure 80. Electrical-resistance change upon repeated bending of graphene, PANI and G/PANI thin films.
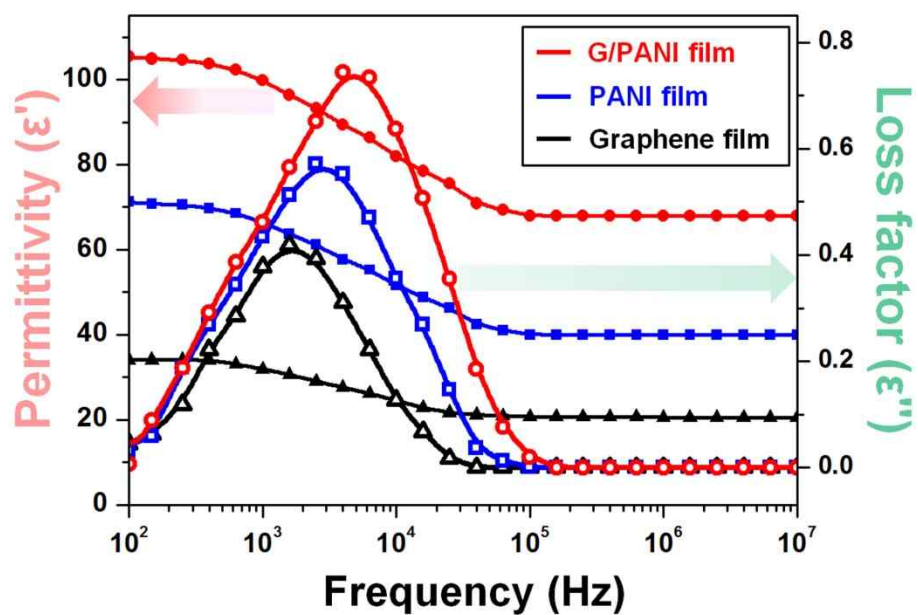
Figure 81. Permittivities and loss factors of graphene, PANI and G/PANI thin films. The loss factor was obtained by differentiation of the permittivity values.

through the interfacial interaction between mediums. For this reason, XRD analysis for the samples were performed to investigate the crystalline structure of the samples.

Figure 82 shows the XRD patterns of pristine graphene, PANI and G/PANI thin films. The XRD pattern of pristine graphene presented a one broad peak centered at 24.58 ° (d-spacing = *ca.* 3.62Å) [175]. In the case of pristine PANI, three diffraction peaks were observed at 2θ = 15.3°, 20.5°, and 25.6° (d-spacings = ca. 5.8, 4.3, and 3.5 Å) on the broad background, revealing the semi-crystalline nature of the PANI. Compared to pristine PANI, XRD pattern of G/PANI demonstrates that the peaks at 15.3°, 20.4° and the broad background mostly disappeared, and the diffraction pattern was dominated by the peak at 25.6°. This indicates an increase in the crystalline phase and strengthened stacking along the specific direction. Especially, the disappearance of the intrinsic peak of graphene clearly indicates that the graphene is properly intercalated into PANI chains. Furthermore, the increase in the intensity of the peak at 25.6° reflect that intensified π–π inter-chain stacking between the phenyl rings of the PANI chains [176,177]. In addition, based on the strengthened peak (25.6°) of the G/PANI thin film, it is considered that the basal planes of RGO and phenyl rings form planar chain conformation and compact packing structure with a distance of 3.5 Å (Figure 83). This
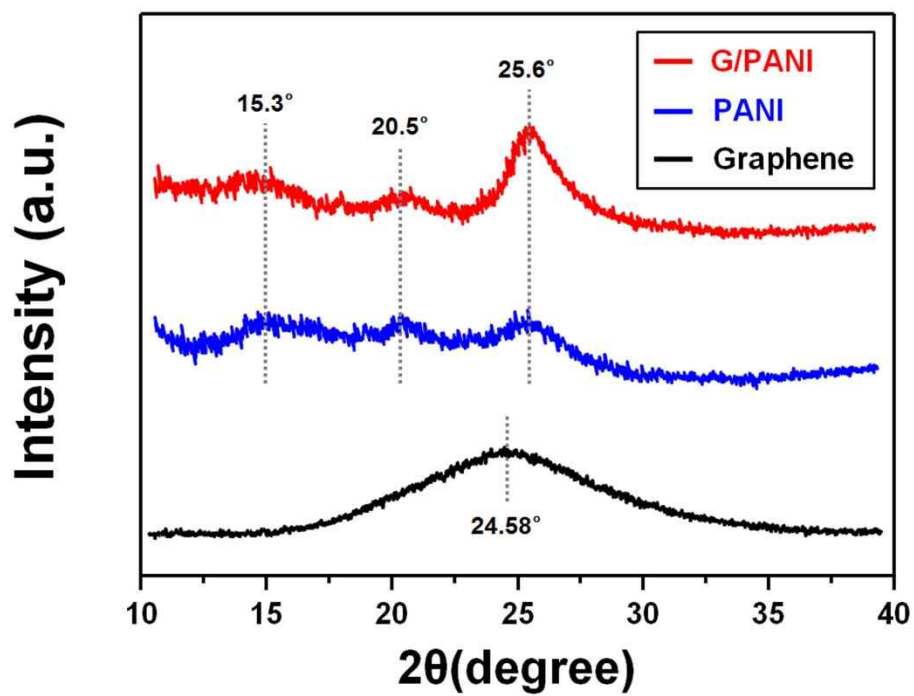
Figure 82. The XRD patterns of graphene, PANI and G/PANI. For XRD sample preparation, power-types were used.
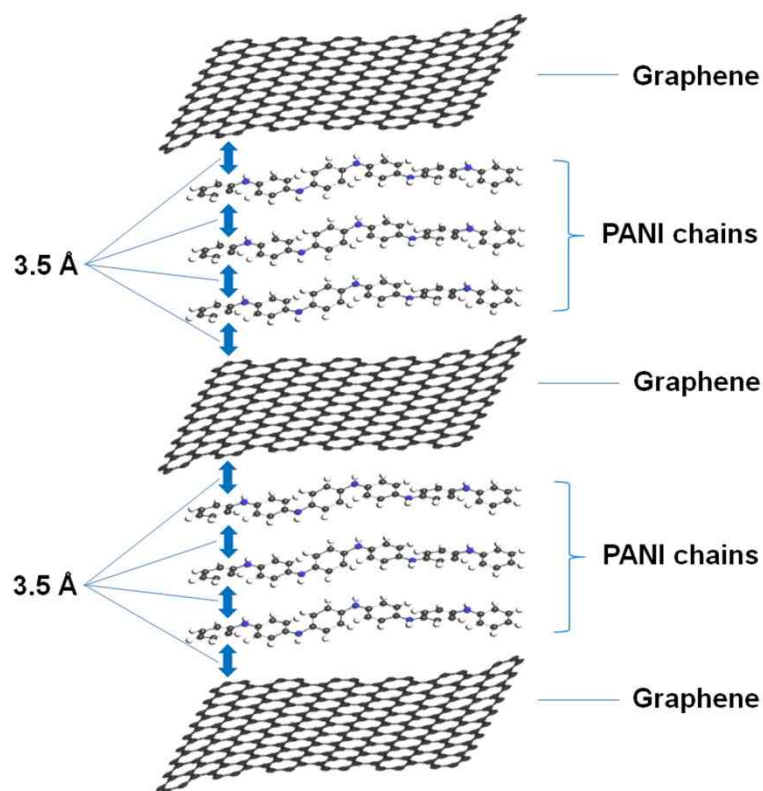
Figure 83. Schematic representation of interaction between graphene and PANI chains leading to compact packing of the PANI chains with graphene and extensive three-dimensional delocalization of the charge.

phenomena caused the improved π–π interactions and extensive three-dimensional delocalization of charge, which leading to the increase in the crystallinity, electrical conductivity and permittivity [178,179].

Three types of line pattern were connected to an RF network analyzer using an SMA-type connector for monopole antenna tests. As a result, The pristine graphene, PANI and G/PANI-based monopole tag antenna had a 874.5 MHz, 1.31 and 1.98 GHz mean frequency, respectively (Figure 84). Furthermore, an *RL* of 14.9, 16.8 and 18.5 dB indicated a increased transmitted power efficiency of 96.7, 97.9 and 98.5%, respectively (Table 6). The widely different mean frequency is ascribed to the difference of permittivity. In general, The speed of an electromagnetic wave propagation in a given medium is given as follows:

$$c = \frac{c_0}{\sqrt{\varepsilon_r \mu_r}}$$

where c_0, ε_r and μ_r are the speed of light in free space, relative permittivity and permeability of medium. In other words, increase in permittivity lowered the speed of an electromagnetic wave propagation in the medium, which resultant in decreased wavelength and size as follows:

$$\lambda = \frac{c}{f} = \frac{c_0}{f\sqrt{\varepsilon_r}} = \frac{\lambda_0}{\sqrt{\varepsilon_r}}$$

where f and λ_0 are the frequency and wavelength of a plane wave in free space. From the point of view, high permittivity and conductivity of G/PANI thin film made it possible to have a high efficient monopole antenna with smaller size.
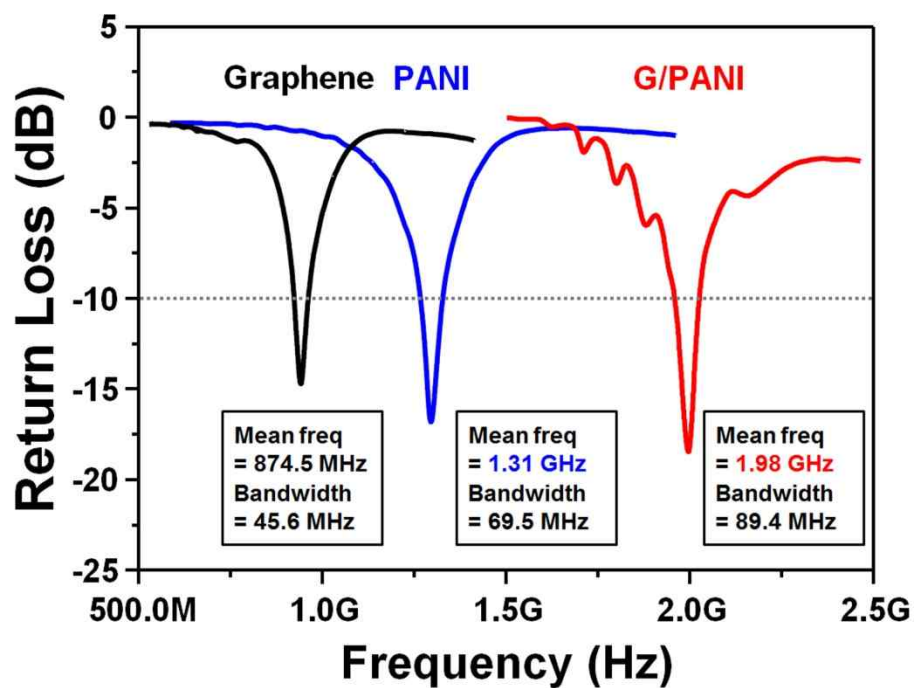
Figure 84. The return loss curve of the monopole antenna using a graphene, PANI and G/PANI-based electrodes. For the fabrication of monopole antenna, 30 mm x 500 μm rectangle films were formed on flexible photo paper.

Table 6. VSWR and RL of various G/PANI-based monopole antenna.

Sample	VSWR	RL[a]	Reflection Coefficeint (Γ)	Transmitted Power	Reflected Power
Graphene	1.44	14.9	0.18	96.7	3.3
PANI	1.34	16.8	0.15	97.9	2.1
G/PANI	1.27	18.5	0.12	98.6	1.4

[a] This value was acquired in the E5071B ENA RF Network Analyzer of Agilent Technologies.

4. CONCLUSIONS

1. The simple and effective strategy to pattern the graphene nanosheets was demonstrated using an inkjet printing method. The graphene nanosheets consisted of a few layers were successfully patterned on PET film with high resolution, and the fine tuning of the sheet resistance was achieved via gradient patterning. Furthermore, it could be also simply controlled by varying concentration of GO ink and the number of printing. Interestingly, the graphene-based thin film could be used as an electrode for WB antenna. The graphene sheets-based WB dipole antenna was implemented with 500 MHz bandwidth and high transmitted power efficiency of 96.7 %, and it can be applied for signal receiving apparatus such as RFID tag, airport passenger screening detecting nearby objects and body sensor network using Medical Implant Communication Service (MICS) band.

2. Flexible and transparent graphene thin film as an acoustic actuator electrode was fabricated using inkjet printing and VDP method. The overall frequency responses were enhanced with increasing the film thickness, particularly over the midrange frequency. Moreover, the frequency response was obviously enhanced in the bass and midrange frequency at the bending condition compared to the flat condition. The sound level of the graphene-based transducer could produce at least 3.1 times higher than

that of the commercial transducer at the same driving voltage. The ability to design shape and size by inkjet printing is expected to offer a great feasibility to give the thin film acoustic actuator various and improved stereo height and width, which is able to produce the sound from everywhere over a large-size panel.

3. The simple and effective mechanochemical approach was used to control the size of GO sheets. GO nanosheets having outstanding dispersibility were prepared in silicone oil. The superior dispersibility derived from the small average particle size and narrow particle size distribution, and the high degree of oxidation of the nanosheets. Ball milling transformed the GO flake morphology into a spherical form, and lowered the density slightly. The GO-based ER fluid made with GO ball-milled for 2 h had the best ER performance (shear stress of 78.5 Pa at a shear rate of 1 s^{-1}), which was double that of the non-milled GO-based ER fluid, and had fast response and recovery times under applied electric fields. The ability to control the size of a graphene sheet is an important advance toward graphene commercialization using a high-quality, scalable production process.

4. The graphene hybrid thin film with controlled domain size was successfully fabricated via mechanochemical method and screen printing. It was noteworthy that the hybrid thin film with 20 wt% of 2h ball-milled

graphene had a low sheet resistance of 0.73 kΩ sq^{-1}, which is *ca.* 1.5 times lower than the sheet resistance of pristine graphene thin film, thus suggesting a bridging effect of small domain-sized graphene (400−700 nm) between adjacent graphene layers with micometer size along the horizontal and vertical axes. In addition, outstanding dispersibility could make it possible to have improved adhesion of the graphene hybrid thin film to the flexible PES substrate. Large-area graphene hybrid thin film with uniformity and flexibility would be suitable for use as a commercial transparent conductive electrode.

5. The sub-kilogram scale of EGnP with multi-layered graphene sheets was successfully fabricated using a simple mild-oxidation of pristine graphite. The substantial amount of trapped water molecules in EGnP made it a good ionic conductor, while simultaneously allowing it to serve as an electrolyte with ion transport characteristics. Synthesized EGnP produced by screen printing could be used as electro-heating elements in line heaters due to its high electrical and thermal conductivity. The EGnP-based line heater demonstrated fast heat propagation with uniform temperature distribution. In addition, the manipulation of the applied voltage and bending radius allowed control over the steady-state temperature of EGnP-based line heaters. Most importantly, the screen printing of EGnP provided a means to

easily control the film's shape and size, suggesting its application to the production of cheap, lightweight patch heaters for industry.

6. A G/PANI/PSS-based conducting paste was successfully fabricated by introducing a PANI/PSS nanofiller into a multilayer graphene matrix by mechanical blending. The incorporation of high concentrations of PSS, which acted as a compatibilizer and binder, by ex-situ polymerization allowed for uniform surface resistance and good adhesion to a flexible substrate. The G/PANI/PSS hybrid film functioned as the electrode in a dipole tag antenna due to its high electrical conductivity and structural flexibility. The hybrid film-based dipole tag antenna was implemented at a center frequency of 910 MHz and boasted a high transmitted power efficiency of 98.5% with a 0.42m recognition distance. These characteristics indicate that such an electrode would be suitable for use as a signal-receiving apparatus that could detect nearby objects.

7. The G/PANI hybrid thin film was successfully fabricated via in-situ polymerization and screen printing. The strong π–π interactions of graphene with the quinoid rings of the PANI chains induced the more expanded conformation of the PANI chains, leading to improvement in the mechanical, electrical property and crystallinity of the film. Outstanding conductivity and permittivity G/PANI thin films made it possible to have a

high efficient monopole antenna with smaller size. The G/PANI-based monopole tag antenna had a 1.98 GHz mean frequency and transmitted power efficiency of 98.5%. This approach will offer a valuable and promising tool for producing highly flexible, scalable, and high-performance RFID antenna electrodes.

In summary, four different ways in the synthetic methodology of graphene materials and flexible graphene thin films using solution processes were demonstrated. First, chemically exfoliated graphene thin films were fabricated via inkjet printing and vapor deposition process. Second, size-controlled graphene thin films with uniform conductivity and outstanding flexibility could be prepared through a mechanochemical method and screen printing. Third, multilayered graphene thin films with good thermal conductivity were able to be obtained from the simple mild-oxidation of pristine graphite and screen printing. Lastly, graphene/polyaniline thin films with outstanding mechanical and electrical property could have been formed by in or ex-situ polymerization and screen printing. These novel strategies do not require a high-cost processing techniques, and the simple process can be used as an alternative tool for the fabrication of various carbon-based thin films and functional devices.

The graphene-based thin films via solution process have been successfully applied in a wide variety of applications, suggesting that these nanomaterials may be potentially very useful in many new electrode types of applications related to electronic/optoelectronic devices, conductive nanocomposites, actuators, sensors and energy storage/conversion systems.

REFERENCES

[1]   J. H. Chen, C. Jang, S. Xiao, M. Ishigami, M. S. Fuhrer, *Nat. Nanotech.*, **2008**, *3*, 206.

[2]   A. K. Geim, P. Kim, *Scientific American*, **2008**, *298*, 90.

[3]   X. K. Lu, M. F. Yu, H. Huang, R. S. Ruoff, *Nanotechnology*, **1999**, *10*, 269.

[4]   K. S. Novoselov, A. K. Geim, S. V. Morozov, D. Jiang, Y. Zhang, S. V. Dubonos, I. V. Grigorieva, A. A. Firsov, *Science*, **2004**, *306*, 666.

[5]   J. C. Meyer, A. K. Geim, M. I. Katsnelson, K. S. Novoselov, T. J. Booth, S. Roth, *Nature*, **2007**, *446*, 60.

[6]   K. I. Bolotin, K. J. Sikes, J. Hone, H. L. Stormer, P. Kim, *Phys. Rev. Lett.*, **2008**, *101*, 096802.

[7]   A. S. Mayorov, R. V. Gorbachev, S. V. Morozov, L. Britnell, R. Jalil, L. A. Ponomarenko, P. Blake, K. S. Novoselov, K. Watanabe, T. Taniguchi, A. K. Geim, *Nano Lett.*, **2011**, *11*, 2396.

[8]   C. Lee, X. Wei, J. W. Kysar, J. Hone, *Science*, **2008**, *321*, 385.

[9]   A. A. Balandin, *Nat. Mater.*, **2011**, *10*, 569.

[10]   R. R. Nair, P. Blake, A. N. Grigorenko, K. S. Novoselov, T. J. Booth, T. Stauber, N. M. R. Peres, A. K. Geim, *Science*, **2008**, *320*, 1308.

[11]   J. S. Bunch, S. S. Verbridge, J. S. Alden, A. M. van der Zande, J. M. Parpia, H. G. Craighead, P. L. McEuen, *Nano Lett.*, **2008**, *8*, 2458.

[12]   R. S. Edwards, K. S. Coleman, *Nanoscale*, **2013**, *5*, 38.

[13]   C. N. R. Rao, A. K. Sood, K. S. Subrahmanyam, A. Govindaraj, *Angew. Chem. Int. Ed.*, **2009**, *48*, 7752.

[14]   D. Wei, Y. Liu, *Adv. Mater.*, **2010**, *22*, 3225.

[15]   R. O. Brennan, *J. Chem. Phys.*, **1952**, *20*, 40.

[16]   D. D. L. Chung, *J. Mater. Sci.*, **1987**, *22*, 4190.

[17]   K. S. Novoselov, D. Jiang, F. Schedin, T. J. Booth, V. V. Khotkevich, S. V. Morozov, A. K. Geim, *Proc. Natl. Acad. Sci.*, **2005**, *102*, 10451.

[18]   P. Blake, E. W. Hill, A. H. Castro Neto, K. S. Novoselov, D. Jiang, R. Yang, T. J. Booth, A. K. Geim, *Appl. Phys. Lett.*, **2007**, *91*, 063124.

[19]   G. Wang, B. Wang, J. Park, Y. Wang, B. Sun, J. Yao, *Carbon*, **2009**, *47*, 3242.

[20]   C. –Y. Su, A. –Y. Lu, Y. Xu, F. –R. Chen, A. N. Khlobystov, L. –J. Li, *ACS Nano*, **2011**, *5*, 2332.

[21]   J. M. Englert, J. Röhrl, C. D. Schmidt, R. Graupner, M. Hundhausen, F. Hauke and A. Hirsch, *Adv. Mater.*, **2009**, *21*, 4265.

[22]   D. A. C. Brownson, J. P. Metters, D. K. Kampouris, C. E. Banks, *Electroanalysis*, **2011**, *23*, 894.

[23]   H. Huang, Y. Xia, X. Tao, J. Du, J. Fang, Y. Gan, W. Zhang, *J. Mater. Chem.*, **2012**, *22*, 10452.

[24] T. Wei, Z. Fan, G. Luo, C. Zheng and D. Xie, *Carbon*, **2009**, *47*, 337.

[25] S. Malik, A. Vijayaraghavan, R. Erni, K. Ariga, I. Khalakhan, J. P. Hill, *Nanoscale*, **2010**, *2*, 2139.

[26] S. R. Dhakate, N. Chauhan, S. Sharma, J. Tawale, S. Singh, P. D. Sahare, R. B. Mathur, *Carbon*, **2011**, *49*, 1946.

[27] W. Fu, J. Kiggans, S. H. Overbury, V. Schwartz, C. Liang, *Chem. Commun.*, **2011**, *47*, 5265.

[28] A. Safavi, M. Tohidi, F. A. Mahyari, H. Shahbaazi, *J. Mater. Chem.*, **2012**, *22*, 3825.

[29] N. −W. Pu, C. −A. Wang, Y. Sung, Y. −M. Liu, M. −D. Ger, *Mater. Lett.*, **2009**, *63*, 1987.

[30] J. S. Moon, D. Curtis, M. Hu, D. Wong, C. McGuire, P. M. Campbell, G. Jernigan, J. L. Tedesco, B. VanMil, R. Myers-Ward, C. J. Eddy, D. K. Gaskill, *IEEE Electron. Device Lett.*, **2009**, *30*, 650.

[31] O. C. Compton, S. T. Nguyen, *Small*, **2010**, *6*, 711.

[32] S. Park, J. An, I. Jung, R. D. Piner, S. J. An, X. Li, A. Velamakanni, R. S. Ruoff, *Nano Lett.*, **2009**, *9*, 1593.

[33] M. A. Rafiee, J. Rafiee, Z. Wang, H. Song, Z.-Z. Yu, N. Koratkar, *ACS Nano*, **2009**, *3*, 3884.

[34] Y. Shao, J. Wang, M. Engelhard, C. Wang, Y. Lin, *J. Mater. Chem.*,

2010, *20*, 743.

[35] L. J. Cote, R. Cruz-Silva, J. Huang, *J. Am. Chem. Soc.*, **2009**, *131*, 11027.

[36] V. Strong, S. Dubin, M. F. El-Kady, A. Lech, Y. Wang, B. H. Weiller, R. B. Kaner, *ACS Nano*, **2012**, *6*, 1395.

[37] D. V. Kosynkin, A. L. Higginbotham, A. Sinitskii, J. R. Lomeda, A. Dimiev, B. K. Price, J. M. Tour, *Nature*, **2009**, *458*, 872.

[38] L. Jiao, L. Zhang, X. Wang, G. Diankov, H. Dai, *Nature*, **2009**, *458*, 877.

[39] A. G. Cano-Márquez, F. J. Rodríguez-Macías, J. Campos-Delgado, C. G. Espinosa-González, F. Tristán-López, D. Ramírez-González, D. A. Cullen, D. J. Smith, M. Terrones, Y. I. Vega-Cantú, *Nano Lett.*, **2009**, *9*, 1527.

[40] K. I. Bolotin, K. J. Sikes, Z. Jiang, M. Klima, G. Fudenberg, J. Hone, P. Kim, H. L. Stormer, *Solid State Commun.*, **2008**, *146*, 351.

[41] J. Moser, A. Barreiro, A. Bachtold, *Appl. Phys. Lett.*, **2007**, *91*, 163513.

[42] L. Xie, H. Wang, C. Jin, X. Wang, L. Jiao, K. Suenaga, H. Dai, *J. Am. Chem. Soc.*, **2011**, *133*, 10394.

[43] S. Cho, K. Kikuchi, A. Kawasaki, *Carbon*, **2011**, *49*, 3865.

[44] P. Sutter, *Nat. Mater.*, **2009**, *8*, 171.

[45]   K. V. Emtsev, A. Bostwick, K. Horn, J. Jobst, G. L. Kellogg, L. Ley, J. L. McChesney, T. Ohta, S. A. Reshanov, J. Rohrl, E. Rotenberg, A. K. Schmid, D. Waldmann, H. B. Weber, T. Seyller, *Nat. Mater.*, **2009**, *8*, 203.

[46]   R. M. Tromp, J. B. Hannon, *Phys. Rev. Lett.*, **2009**, *102*, 106104.

[47]   Q. Huang, X. Chen, J. Liu, W. Wang, G. Wang, W. Wang, R. Yang, Y. Liu, L. Guo, *Chem. Commun.*, **2010**, *46*, 4917.

[48]   Z. Wu, W. Ren, L. Gao, B. Liu, C. Jiang, H. Cheng, *Carbon*, **2009**, *47*, 493.

[49]   Z. –Y. Juang, C. –Y. Wu, C. –W. Lo, W. –Y. Chen, C. –F. Huang, J. –C. Hwang, F. –R. Chen, *Carbon*, **2009**, *47*, 2026.

[50]   J. D. Caldwell, T. J. Anderson, J. C. Culbertson, G. G. Jernigan, K. D. Hobart, F. J. Kub, M. J. Tadjer, J. L. Tedesco, J. K. Hite, M. A. Mastro, R. L. Myers-Ward, C. R. Eddy, P. M. Campbell, D. K. Gaskill, *ACS Nano*, **2010**, *4*, 1108.

[51]   Y. Dedkov, A. Shikin, V. Adamchuk, S. Molodtsov, C. Laubschat, A. Bauer, G. Kaindl, *Phys. Rev. B*, **2001**, *64*, 035405.

[52]   P. W. Sutter, J. –I. Flege, E. A. Sutter, *Nat. Mater.*, **2008**, *7*, 406.

[53]   Y. S. Dedkov, M. Fonin, C. Laubschat, *Appl. Phys. Lett.*, **2008**, *92*, 052506.

[54]   S. Bae, H. Kim, Y. Lee, X. Xu, J. –S. Park, Y. Zheng , J. Balakrishnan, T. Lei, H. Ri Kim, Y. I. Song, Y. –J. Kim, K. S. Kim, B. Ozyilmaz, J. –H. Ahn, B. H. Hong, S. Iijima, *Nat. Nanotechnol.*, **2010**, *5*, 574.

[55]   W. Cai, R. D. Piner, Y. Zhu, X. Li, Z. Tan, H. C. Floresca, C. Yang, L. Lu, M. J. Kim, R. S. Ruoff, *Nano Res.*, **2009**, *2*, 851.

[56]   A. Reina, X. Jia, J. Ho, D. Nezich, H. Son, V. Bulovic, M. S. Dresselhaus, J. Kong, *Nano Lett.*, **2009**, *9*, 30.

[57]   G. Lopez, E. Mittemeijer, *Scr. Mater.*, **2004**, *51*, 1.

[58]   G. L. Selman, P. J. Ellison, A. s. Darling, *Platinum Metals Rev.*, **1970**, *14*, 14.

[59]   S. Bhaviripudi, X. Jia, M. S. Dresselhaus, J. Kong, *Nano Lett.*, **2010**, *10*, 4128.

[60]   K. Yan, H. Peng, Y. Zhou, H. Li, Z. Liu, *Nano Lett.*, **2011**, *11*, 1106.

[61]   S. Chen, W. Cai, R. D. Piner, J. W. Suk, Y. Wu, Y. Ren, J. Kang, R. S. Ruoff, *Nano Lett.*, **2011**, *11*, 3519.

[62]   A. Dato, V. Radmilovic, Z. Lee, J. Phillips, M. Frenklach, *Nano Lett.*, **2008**, *8*, 2012.

[63]   A. Dato, M. Frenklach, *New J. Phys.*, **2010**, *12*, 125013.

[64]   C. R. Herron, K. S. Coleman, R. S. Edwards, B. G. Mendis, *J. Mater. Chem.*, **2011**, *21*, 3378.

[65]   J. Wu, W. Pisula, K. Muellen, *Chem. Rev.*, **2007**, *107*, 718.

[66]   X. Yang, X. Dou, A. Rouhanipour, L. Zhi, H. J. Rader, K. Müllen, *J. Am. Chem. Soc.*, **2008**, *130*, 4216.

[67]   J. Cai, P. Ruffieux, R. Jaafar, M. Bieri, T. Braun, S. Blankenburg, M. Muoth, A. P. Seitsonen, M. Saleh, X. Feng, K. Muellen, R. Fasel, *Nature*, **2010**, *466*, 470.

[68]   X. Yan, X. Cui, L.-s. Li, *J. Am. Chem. Soc.*, **2010**, *132*, 5944.

[69]   X. Yan, X. Cui, B. Li, L.-s. Li, *Nano Lett.*, **2010**, *10*, 1869.

[70]   A. K. Geim, K. S. Novoselov, *Nature Mater.*, **2007**, *6*, 183.

[71]   H. P. Boehm, R. Setton, E. Stumpp, *Pure Appl. Chem.*, **1994**, *66*, 1893.

[72]   K. S. Novoselov, V. I. Fal'ko, L. Colombo, P. R. Gellert, M. G. Schwab, K. Kim, *Nature*, **2012**, *490*, 192.

[73]   W. J. Yu, S. H. Chae, S. Y. Lee, D. L. Duong, Y. H. Lee, *Adv. Mater.*, **2011**, *23*, 1889.

[74]   R. –H. Kim, M. –H. Bae, D. G. Kim, H. Cheng, B. H. Kim, D. –H. Kim, M. Li, J. Wu, F. Du, H.-S. Kim, S. Kim, D. Estrada, S. W. Hong, Y. Huang, E. Pop, J. A. Rogers, *Nano Lett.*, **2011**, *11*, 3881.

[75]   K. S. Kim, Y. Zhao, H. Jang, S. Y. Lee, J. M. Kim, K. S. Kim, J. H. Ahn, P. Kim, J.-Y. Choi, B. H. Hong, *Nature*, **2009**, *457*, 706.

[76]   J. Wang, M. Liang, Y. Fang, T. Qiu, J. Zhang, L. Zhi, *Adv. Mater.*,

2012, *24*, 2874.

[77]   S.-K. Lee, B. J. Kim, H. Jang, S. C. Yoon, C. Lee, B. H. Hong, J. A. Rogers, J. H. Cho, J.-H. Ahn, *Nano Lett.*, **2011**, *11*, 4642.

[78]   N. M. R. Peres, F. Guinea, A. H. C. Neto, *Ann. Phys.*, **2006**, *321*, 1559.

[79]   M. J. Allen, V. C. Tung, L. Gomez, Z. Xu, L. –M. Chen, K. S. Nelson, C. Zhou, R. B. Kaner, Y. Yang, *Adv. Mater.*, **2009**, *21*, 2098.

[80]   X. Li, X. Wang, L. Zhang, S. Lee, H. Dai, *Science*, **2008**, *319*, 1229.

[81]   S. J. Kang, B. Kim, K. S. Kim, Y. Zhao, Z. Chen, G. H. Lee, J. Hone, P. Kim, C. Nuckolls, *Adv. Mater.*, **2011**, *23*, 3531.

[82]   B. J. Kim, H. Jang, S. –K. Lee, B. H. Hong, J. –H. Ahn, J. H. Cho, *Nano Lett.*, **2010**, *10*, 3464.

[83]   C. Lee, X. Wei, J. W. Kysar, J. Hone, *Science*, **2008**, *321*, 385.

[84]   F. Schedin, A. K. Geim, S. V. Morozov, E. W. Hill, P. Blake, M. I. Katsnelson, K. S. Novoselov, *Nat. Mater.*, **2007**, *6*, 652.

[85]   J. D. Fowler, M. J. Allen, V. C. Tung, Y. Yang, R. B. Kaner, B. H. Weiller, *ACS Nano*, **2009**, *3*, 201.

[86]   K. S. Novoselov, Z. Jiang, Y. Zhang, S.V. Morozov, H. L. Stormer, U. Zeitler, J. C. Maan, G. S. Boebinger, P. Kim, A. K. Geim, *Science*, **2007**, *315*, 1379.

[87]   V. Dua, S. P. Surwade, S. Ammu, S. R. Agnihotra, S. Jain, K. E.

Roberts, S. Park, R. S. Ruoff, S. K. Manohar, *Angew. Chem. Int. Ed.*, **2010**, *49*, 2154.

[88]   C. Shan, H. Yang, J. Song, D. Han, A. Ivaska, and L. Niu, *Anal. Chem.*, **2009**, *81*, 2378.

[89]   S. Alwarappan, A. Erdem, C. Liu, and C. Z. Li, *J. Phys. Chem. C*, **2009**, *113*, 8853.

[90]   J. Jang, J. Bae, M. Choi, *Carbon*, **2005**, *43*, 2730.

[91]   M. Choi, B. Lim, J. Jang, *Macromol. Res.*, **2008**, *16*, 200.

[92]   M. D. Stoller, S. Park, Y. Zhu, J. An, R. S. Ruoff, *Nano Lett.*, **2008**, *8*, 3498.

[93]   A. V. Murugan, T. Muraliganth, A. Manthiram, *Chem. Mater.*, **2009**, *21*, 5004.

[94]   J. Yan, T. Wei, B. Shao, Z. Fan, W. Qian, M. Zhang, F. Wei, *Carbon*, **2010**, *48*, 487.

[95]   Y. Wang, Z. Shi, Y. Huang, Y. Ma, C. Wang, M. Chen, Y. Chen, *J. Phys. Chem. C*, **2009**, *113*, 13103.

[96]   M. D. Stoller, S. Park, Z. Yanwu, J. An, R. S. Ruoff, *Nano Lett.*, **2008**, *8*, 3498.

[97]   J. J. Yoo, K. Balakrishnan, J. Huang, V. Meunier, B. G. Sumpter, A. Srivastava, M. Conway, A. L. Mohana Reddy, J. Yu, R. Vajtai, P. M.

Ajayan, *Nano Lett.*, **2011**, *11*, 1423.

[98]   W. Gao, N. Singh, L. Song, Z. Liu, A. L. M. Reddy, L. Ci, R. Vajtai, Q. Zhang, B. Wei, P. M. Ajayan, *Nat. Nanotechnol.*, **2011**, *6*, 496.

[99]   G. Zheng, L. Hu, H. Wu, X. Xie, Y. Cui, *Energy Environ. Sci.*, **2011**, *4*, 3368.

[100]   J. Cho, K. Shin, J. Jang, *Thin Solid Films*, **2010**, *518*, 5066.

[101]   P. Calvert, *Chem. Mater.*, **2001**, *13*, 3299.

[102]   S. Stankovich, D. A. Dikin, R. D. Piner, K. A. Kohlhaas, A. Kleinhammes, Y. Jia, Y. Wu, S. T. Nguyen, R. S. Ruoff, *Carbon*, **2007**, *45*, 1558.

[103]   D. W. Boukhvalov, M. I. Katsnelson, *J. Am. Chem. Soc.*, **2008**, *130*, 10697.

[104]   S. Park, R.S. Ruoff, *Nature*, **2009**, *4*, 217.

[105]   J. T. Robinson, M. Zalalutdinov, J. W. Baldwin, E. S. Snow, Z. Wei, P. Sheehan, B. H. Houston, *Nano Lett.*, **2008**, *8*, 3441.

[106]   B. Lim, J. Jang, *Angew. Chem. Int. Ed.*, **2003**, *42*, 5600.

[107]   G. Eda, G. Fanchini, M. Chhowalla, *Nat. Nanotechnol.*, **2008**, *3*, 270.

[108]   K. –Y. Shin, J. –Y. Hong, S. Lee, J. Jang, *J. Mater. Chem.*, **2012**, *22*, 7871.

[109]   N. A. Kumar, H. –J. Choi, Y. R. Shin, D. W. Chang, L. Dai, J. –B.

Baek, *ACS Nano*, **2012**, *6*, 1715.

[110] J. Bae, J. Jang, *Angew. Chem.*, **2004**, *116*, 3891.

[111] F. Thomsen, S. Reich, *Phys. Rev. Lett.*, **2000**, *85*, 5214.

[112] Y. Hernandez, V. Nicolosi, M. Lotya, F. M. Blighe, Z. Sun, S. De, I. T. Mc-govern, B. Holland, M. Byrne, Y. K. Gun'ko, J. J. Boland, P. Niraj, G. Duesberg, S. Krishnamurthy, R. Goodhue, J. Hutchison, V. Scardaci, A. C. Ferrari, J. N. Coleman, *Nat. Nanotechnol.*, **2008**, *3*, 563.

[113] A.C. Ferrari, *Phys. Rev. Lett.*, **2006**, *97*, 187401.

[114] J. Cho, K. –H. Shin, J. Jang, *Synth. Met.*, **2010**, *160*, 1119.

[115] H. Yoon, J. Jang, *Adv. Funct. Mater.*, **2009**, *19*, 1567.

[116] V. Dua, S. P. Surwade, S. Ammu, S. R. Agnihotra, S. Jain, K. E. Roberts, S. Park, R. S. Ruoff, S. K. Manohar, *Angew. Chem. Int. Ed.*, **2010**, *49*, 2154.

[117] N. A. Luechinger, S. Loher, E. K. Athanassiou, R. N. Grass,W. J. Stark, *Langmuir*, **2007**, *23*, 3473.

[118] M. Dragoman, A. A. Muller, D. Dragoman, F. Coccetti, R. Plana, J. Appl. Phys., **2010**, *107*, 104313.

[119] J. H. So, J. Thelen, A. Qusba, G. J. Hayes, G. Lazzi, M. D. Dickey, *Adv. Funct. Mater.*, **2009**, *19*, 3632.

[120] M. Kubo, X. Li, C. Kim , M. Hashimoto, B. J. Wiley, D. Ham, G. M.

Whitesides, *Adv. Mater.*, **2010**, *22*, 2749.

[121] S. Cheng, A. Rydberg, K. Hjort, Z. Wu, *Appl. Phys. Lett.*, **2009**, *94*, 144103.

[122] Y. Tikhov, J. H. Won, *Electron. Lett.*, **2004**, *40*, 574.

[123] H. Sirringhaus, T. Kawase, R. H. Friend, T. Shimoda, M. Inbasekaran, W. Wu, E. P. Woo, *Science*, **2000**, *290*, 2123.

[124] Y. Yoshioka, P. D. Calvert, G. E. Jabbour, *Macromol. Rapid. Commun.*, **2005**, *26*, 238.

[125] S. Lee, J. –S. Park, T. R. Lee, *Bull. Korean Chem. Soc.*, **2011**, *32*, 41.

[126] N. Vandencasteele, D. Merche, F. Reniers, *Surf. Interface Anal.*, **2006**, *38*, 526.

[127] A. Vesel, M. Mozetic, A. Zalar, *Vacuum*, **2008**, *82*, 248.

[128] X. Yu, H. Zhu, R. Rajamani, K. A. Stelson, *Smart Mater. Struct.*, **2007**, *16*, 2006.

[129] H. Zhu, X. Yu, R. Rajamani, K. A. Stelson, *Mechatronics*, **2004**, *14*, 805.

[130] K. –Y. Shin, J. –Y. Hong, S. Lee, J. Jang, *J. Mater. Chem.*, **2012**, *22*, 23404.

[131] Q. Tang, J. Wu, Q. Li, J. Lin, *Polymer*, **2008**, *49*, 5329.

[132] W. S. Hummers, R. E. Offeman, *J. Am. Chem. Soc.*, **1958**, *80*, 1339.

[133] N. I. Kovtyukhova, *Chem. Mater.*, **1999**, *11*, 771.

[134] Y. P. Seo, Y. Seo, *Langmuir*, **2012**, *28*, 3077.

[135] C. McIntyre, H. Yang, P. F. Green, *ACS Appl. Mater. Interfaces*, **2013**, *5*, 8925.

[136] J. B. Yin, X. P. Zhao, *Chem. Mater.*, **2002**, *14*, 4633.

[137] J. C. Kim, M. Seo, M. A. Hillmyer, L. F. Francis, *ACS Appl. Mater. Interfaces*, **2013**, *5*, 11877.

[138] R. Tao, Q. Jiang, *Phys. Rev. Lett.*, **1994**, *73*, 205.

[139] M. Stenicka, V. Pavlinek, P. Saha, N. V. Blinova, J. Stejskal, O. Quadrat, *Colloid Polym. Sci.*, **2009**, *287*, 403.

[140] K. –H. Shin, Y. Jang, B. –S. Kim, J. Jang, S. H. Kim, *Chem. Commun.*, **2013**, *49*, 4887.

[141] M. A. Raza, A. Westwood, A. Brown, N. Hondow, C. Stirling, *Carbon*, **2011**, *49*, 4269.

[142] K. Kalaitzidou, H. Fukushima, P. Askeland, L. T. Drzal, *J. Mater. Sci.*, **2008**, *43*, 2895.

[143] P. –G. Ren, D. –X. Yan, X. Ji, T. Chen, Z. –M. Li, *Nanotechnology*, **2011**, *22*, 055705.

[144] J. Torres, C. C. Perry, S. J. Bransfield, D. H. Fairbrother, *J. Phys. Chem. B*, **2003**, *107*, 5558.

[145]   N. S. Clarke, P. G. Hall, *Langmuir,* **1991**, *7*, 678.

[146]   M. A. Mojid, D. A. Rose, G. C. L. Wyseur, *Eur. J. Soil Sci.*, **2007**, *58*, 560.

[147]   F. Tuinstra, J. L. Koenig, *J. Chem. Phys.*, **1970**, *53*, 1126.

[148]   A. C. Ferrari, *Solid State Commun.*, **2007**, *143*, 47.

[149]   Y. Zhang, J. C. Reed, S. Yang, *ACS Nano*, **2009**, *3*, 2412.

[150]   K. −Y. Shin, J. −Y. Hong, J. Jang, *Adv. Mater.*, **2011**, *23*, 2113.

[151]   J. Kang, H. Kim, K. S. Kim, S. −K. Lee, S. Bae, J. −H. Ahn, Y. –J. Kim, J. –B. Choi, B. H. Hong, *Nano Lett.*, **2011**, *11*, 5154.

[152]   D. Sui, Y. Huang, L. Huang, J. Liang, Y. Ma, Y. Chen, *Small*, **2011**, *7*, 3186.

[153]   T. R. Hendricks, J. Lu, L. T. Drzal, I. Lee, *Adv. Mater.*, **2008**, *20*, 2008.

[154]   W. Wei, X. Qu, *Small*, **2012**, *8*, 2138.

[155]   J. Ha, J. Cho, J. Jang, *Adv. Mater.*, **2007**, *19*, 1772.

[156]   C. P. L. Rubinger, R. Faez, L. C. Costa, C. R. Martins, R. M. Rubinger, Polym. Bull., **2008**, *60*, 379.

[157]   D. W. Hatchett, D. Josowicz, J. Janata, *J. Phys. Chem. B*, **1999**, *103*, 10992.

[158]   K. –S. HO, T. –H. Hsieh, C. –W. Kuo, S. –W. Lee, J. –J. Lin, Y. –J. Huang, *J. Polym. Sci., Part A: Polym. Chem.*, **2005**, *43*, 3116.

[159] S. H. Lee, D. H. Lee, K. Lee, C. W. Lee, *Adv. Funct. Mater.*, **2005**, *15*, 1495.

[160] M. Ginic-Markovic, J. G. Matisons, R. Cervini, G. P. Simon, P. M. Fredericks, *Chem. Mater.*, **2006**, *18*, 6258.

[161] A. G. MacDiarmid, A. J. Epstein, *Synth. Met.*, **1994**, *65*, 103.

[162] U. J. Lee, S. –H. Lee, J. J. Yoon, S. J. Oh, S. H. Lee, J. K. Lee, *Sol. Energy Mater. Sol. Cells*, **2013**, *108*, 50.

[163] J. Zhang, J. Jiang, H. Li, X. S. Zhao, *Energy Environ. Sci.*, **2011**, *4*, 4009.

[164] H. Wang, Q. Hao, X. Yang, L. Lu, X. Wang, *Nanoscale*, **2010**, *2*, 2164.

[165] G. Niaura, R. Mažeikienė, A. Malinauskas, *Synth. Met.*, **2004**, *145*, 105.

[166] J. E. Pereira da Silva, D. L. A. de Faria, S. I. Cordoba de Torresi, M. L. A. Temperini, *Macromolecules*, **2000**, *33*, 3077.

[167] S. Bourdo, Z. Li, A. S. Biris, F. Watanabe, T. Viswanathan, I. Pavel, *Adv. Funct. Mater.*, **2008**, *18*, 432.

[168] M. Jain, S. Annapoorni, *Synth. Met.*, **2010**, *160*, 1727.

[169] R. Mažeikienė, V. Tomkutė, Z. Kuodis, G. Niaura, A. Malinauskas, *Vib. Spectrosc.*, **2007**, *44*, 201.

[170] S. Quillard, G. Louarn, S. Lefrant, A. Macdiarmid, *Phys. Rev. B*, **1994**, *50*, 12496.

[171] A. Ray, G. E. Asturias, D. L. Kershner, A. F. Richter, A. G. MacDiarmid, A. J. Epstein, *Synth. Met.*, **1989**, *29*, 141.

[172] M. C. Bernard, A. Hugot-Le Goff, *Electrochim. Acta*, **2006**, *52*, 595

[173] S. Bhadra, N. K. Singha, D. Khastgir, *Polym. Int.*, **2007**, *56*, 919.

[174] M. −I. Boyer, S. Quillard, E. Rebourt, G. Louarn, J. P. Buisson, A. Monkman, S. Lefrant, *J. Phys. Chem. B*, **1998**, *102*, 7382.

[175] K. Zhang, L. L. Zhang, X. S. Zhao, J. Wu, *Chem. Mater.*, **2010**, *22*, 1392.

[176] K. Lee, S. Cho, S. H. Park, A. J. Heeger, C. W. Lee, S. H. Lee, *Nature*, **2006**, *441*, 65.

[177] H. −W. Park, T. Kim, J. Huh, M. Kang, J. E. Lee, H. Yoon, *ACS Nano*, **2012**, *6*, 7624.

[178] J. P. Pouget, M. E. Jozefowicz, A. J. Epstein, X. Tang, A. G. MacDiarmid, *Macromolecules*, **1991**, *24*, 779.

[179] A. G. MacDiarmid, A. J. Epstein, *Synth. Met.*, **1994**, *65*, 103.

국문초록

지난 수년 동안 집중적인 연구적 관심을 불러 일으키고 있는 그래핀은 탄소원자가 한층으로 벌집모양의 육각형의 격자를 가진 탄소의 2차원적인 동소체이다. 그래핀의 높은 전자이동도나 높은 전기전도도 등의 물리적 특성뿐만 아니라 우수한 광투과도와 같은 그들 고유구조 특성에 기인한 새로운 물성을 바탕으로 전자공학, 광전자공학, 촉매반응, 에너지 저장 및 변환, 생의학 등의 다양한 분야에 적용되고 있다.

본 연구에서는 다양한 형태 및 크기를 갖는 그래핀을 제조하고, 용액 공정법을 이용하여 유연성 그래핀 박막을 제조하였으며, 이들의 형성 메커니즘과 기계적, 전기적 및 열 특성을 체계적으로 고찰하였고, 아울러 안테나, 음향 작동장치, 투명전극 소재, 패치 히터으로의 응용에 대해 살펴보았다.

첫째로, 화학적 박리된 그래핀 박막은 수분산 산화 그래핀을 잉크젯 프린팅 잉크로 사용하고, 기상증착 환원법을 이용해 제조할 수 있었으며, 안테나 및 음향 작동장치의 전극으로 응용할 수 있었다. 둘째로, 그래핀 도메인 크기는 볼밀 공정을 이용한 기계 화학적 방법에 의해 손쉽게 조절될 수 있었으며, 스크린 프린팅을 이용하여 균일한 전도도 및 높은 유연성 특성을 갖는 그래핀 박막을 제작하고, 투명전극 소재로 활용할 수 있었다. 셋째로, 다층 구조의 그래핀은 흑연 삽입 물질 및 초고주파에 의한 박리 공정을 통해 손쉽게 대량으로 제조할 수 있었으며, 스크린 프린팅

기술을 이용하여 우수한 열 전도도 특성을 갖는 그래핀 박막 기반 패치 히터를 제작할 수 있었다. 마지막으로, 그래핀/폴리아닐린은 인 및 익스시츄 중합법을 이용하여 성공적으로 제조할 수 있었으며, 스크린 프린팅을 이용하여 우수한 기계적 및 전기적 특성을 갖는 그래핀/폴리아닐린 박막을 제작하였고, 이를 모노폴 및 다이폴 태그 안테나 전극으로 사용할 수 있었다.

본 연구에서 새롭게 개발한 유연성 그래핀 박막 제조방법은 제어된 크기 및 모양을 지닌 다양한 종류의 그래핀 제조에 적용될 수 있으며, 기존의 그래핀 박막에 비해 기계적, 전기적 및 열 특성을 향상시킬 수 있었다. 무엇보다도, 다양한 용액 공정법을 이용하여 원하고자 하는 형태의 그래핀 박막을 손쉽게 제작할 수 있으며, 이를 통해 투명전극 소재, 안테나, 음향 작동장치, 패치 히터를 포함한 여러가지 전자소자 응용분야에 폭넓게 활용될 수 있을 것으로 사료된다.

주요어: 그래핀, 제조 방법, 표면 개질, 용액 공정, 유연성 박막, 전극

학번: 2009-23951